Title
In Situ Investigations into CaCO3 Nucleation

Author
Nielsen, Michael Harold

Publication Date
2015

Peer reviewed|Thesis/dissertation

In Situ Investigations into $CaCO_3$ Nucleation

By

Michael Harold Nielsen

A dissertation submitted in partial satisfaction of the

requirements for the degree of

Doctor of Philosophy

in

Engineering – Materials Science and Engineering

in the

Graduate Division

of the

University of California, Berkeley

Committee in charge:

Professor Andrew M. Minor, Co-Chair
Professor James J. De Yoreo, Co-Chair
Professor Mark D. Asta
Professor Seung-Wuk Lee

Summer 2015

Abstract

In Situ Investigations into Calcium Carbonate Nucleation

by

Michael Harold Nielsen

Doctor of Philosophy in Engineering – Materials Science and Engineering

University of California, Berkeley

Professors Andrew M. Minor and James J. De Yoreo, Co-Chairs

Classical theories of nucleation were developed over a hundred years ago starting with Gibbs. However, much remains unknown about the process of phase transition in aqueous electrolyte solutions due to the lack of experimental tools able to probe dynamic processes at the time and length scales of the phase transformation. In the calcium carbonate system, recent discovery of an amorphous phase, as well as the suggested existence of potential precursor states such as so-called 'pre-nucleation clusters' or dense liquid droplets, has called into question the utility of the classical framework in making accurate predictions of nucleation.

Added to these questions are those regarding the effects that chemical templates have on nucleating calcium carbonate. Many organisms use complex organic matrices to form architecturally complex functional structures out of sea water at ambient temperatures. By contrast, laboratory methods to materials synthesis often require extreme conditions yet maintain at best a low level of control over the development of the resulting material. With the goal of tightly controlling formation of functional materials, scientists have looked to such biomineral systems for inspiration. Self-assembled monolayers (SAMs) of functionalized alkanethiols have been found to act as idealized chemical templates for calcium carbonate nucleation, controlling the nucleating plane of the calcite phase for many surface functionalities. Yet there remain many open questions as to the fundamental mechanisms by which these templates achieve this control.

In this dissertation many investigations of calcium carbonate nucleation are discussed, which examine the nucleation pathways of calcium carbonate and mechanisms of control by which alkanethiol surfaces direct the oriented formation of calcite. Traditional in situ microscopy techniques are used to make nucleation rate measurements of templated calcite nucleation on alkanethiol SAMs to test the applicability of the predictions of classical nucleation theory to this system. Low resolution microscopy techniques are further used to provide indirect evidence for the formation pathways of calcite on SAMs exhibiting different surface chemistries. The development of a platform for liquid phase transmission electron microscopy (TEM) utilizing a sealed liquid cell is described, and its utility in making novel observations of materials formation processes is demonstrated. Liquid phase TEM is further employed, using an open cell system which allows for mixing reagents, to directly observe formation pathways in the $CaCO_3$ system.

Table of Contents

Acknowledgements

Numerous people have contributed in various capacities to my graduate school experience and the work contained in this dissertation.

I feel extremely fortunate to have had Jim De Yoreo as a primary research advisor. Jim, in addition to being an excellent scientist and a leading expert in the field, has been an exceedingly conscientious mentor committed to the development of his group members. None of this work would have been possible without his dedicated guidance and support.

Andy Minor, my research advisor in the MSE department, took me in as an orphaned grad student and integrated me into his group, providing useful feedback on my research and helpful career advice.

My research benefited greatly from interacting with many highly intelligent and deeply dedicated scientific circles which surrounded me throughout my graduate career; from the members of Jim's research group who willingly shared their own expertise and with whom I had the pleasure of frequent scientific discussions, to the Berkeley faculty members who taught my courses and sat on my research committees, to the staff scientists at LBL who shared their equipment and their expertise. I owe particular thanks to Shaul Aloni, Virginia Altoe, Stefano Cabrini, Erin Wood, and Ed Wong of The Molecular Foundry, for facilitating the research contained within this dissertation, and for providing useful input on research methods; and also to Mark Asta of the MSE department, who served wonderfully as a Graduate Advisor and made himself readily available to provide excellent advice in navigating the department and the many stages of the graduate program.

Lastly, to Hannah, who has had to do so many things she didn't want to. Thank you.

I was supported throughout my graduate program by the Department of Defense, Air Force Office of Scientific Research, National Defense Science and Engineering Graduate (NDSEG) Fellowship, 32 CFR 168a, the National Science Foundation under grant DMR-1312697, and the Department of Energy, Office of Science Graduate Student Research (SCGSR) Fellowship.

Preface

A number of published or submitted manuscripts have been used throughout this dissertation. Chapters 1 and 5 incorporate material from two submitted book chapters, “Liquid Phase TEM for Studying Environmental and Biological Mineral Systems” (Liquid Cell Electron Microscopy, Cambridge University Press) and “Liquid Phase TEM Invesigations of Crystal Nucleation, Growth and Transformation” (New Perspectives on Mineral Nucleation and Growth, Springer). Chapter 2 is adapted from “The Thermodynamics of Calcite Nucleation at Organic Interfaces: Classical vs. Non-Classical Pathways,” *Faraday Discussions* **159**, 509-523 (2012). Chapter 3 is largely comprised of sections of “Structural Evolution, Formation Pathways and Energetic Controls During Template-Directed Nucleation of $CaCO_3$,” *Faraday Discussions* **159**, 105-121 (2012) and “Investigating Processes of Nanocrystal Formation and Transformation via Liquid Cell TEM,” *Microscopy & Microanalysis* **20**, 425-436 (2014). Chapter 4 is adapted from “In Situ TEM Imaging of CaCO3 Nucleation Reveals Coexistence of Direct and Indirect Pathways,” *Science* **345**, 1158-1162 (2014); one of the figures from this article, however, has been more suitably used in Chapter 1.

Chapter 1

Introduction

1.1 Motivation

The study of materials formation is of paramount importance because it represents the seminal event in the development of a new phase. During biologically mediated formation of mineralized tissues, nucleation and growth are tightly controlled by surrounding organic matrices [1]. These soluble organic and inorganic constituents in cellular or intracellular spaces determine the time of appearance, phase, orientation and shape of the evolving crystal. Moreover these elegant mineral structures are produced by living organisms at ambient conditions, which consists of an aqueous phase and the organism's organic matrix. Synthetic approaches to crystal formation strive for comparable levels of structural hierarchy but lack the level of control observed in nature. Similar to biomineral systems, inorganic chemists rely extensively on the use of organic and inorganic additives to achieve precise control during colloidal synthesis of nanomaterials [2]. Such additives can precisely steer nucleation, enhance anisotropy of crystal growth, and control crystal structure of the growing material, bringing us closer to achieving the goal of precise engineering of technologically relevant nanomaterials. However the level of achievable complexity in materials design is limited by a lack of fundamental understanding of the physical mechanisms and chemical interactions active during crystallization and growth in the presence of additives. Thus the scientific challenge in understanding controlled nanomaterial formation is to explain how and why specific phases and morphologies form, how organic additives or ligands govern their stabilization or transformation, and how chemistry at the organic–inorganic interface defines these processes.

Many open questions in crystallization processes remain in part because traditional characterization tools do not allow for direct observations of the phenomena at relevant length and time scales. The dynamics of nucleation, including formation of the nascent particle, attachment and detachment of the fundamental units, and the transient existence and transformation of potential intermediate phases, typically occur at nanometer length scales limiting the utility of in situ optical [3], scanning electron microscopy [4], and x-ray based imaging [5] and spectroscopic methods. In situ scanned probe microscopy has been successfully applied to nucleation and growth in many surface-mediated systems due to its capability of imaging with adequate spatial resolution. However, the early events in materials formation for many materials occur rapidly relative to the time required for image acquisition. Although recent advances in high scan speed approaches have greatly improved the attainable temporal resolution [6], surface scanning techniques are limited in the samples they can characterize. Scanned probe microscopy is of little use, for example, in examining the role of organic matrices, such as globular phases of macromolecules [7], lipid vesicles [8], amelogenin [9], and collagen [10], where mineralization likely occurs within the matrix. More broadly, methods that minimize surface effects are necessary for better understanding crystallization processes in solution, as

surfaces often substantially change the kinetic barriers and free energies that control nucleation [11, 12].

Lacking techniques for direct, in situ examination of mineralization mechanisms, researchers have turned to alternative approaches to understand these phenomena. Low resolution in situ techniques have produced indirect evidence of crystallization pathways [3, 13], while ex situ imaging [14], calorimetric [15], and spectroscopic [16] approaches have given insight into individual time slices of mineralization processes. In the absence of direct experimental data that follow the birth and development of individual particles, tenets of Classical Nucleation Theory (CNT) originating from Gibbs [17] have been challenged by novel theoretical frameworks. Nucleation in electrolyte solutions as described by CNT, occurs via unstable density fluctuations of monomer attachment and detachment that, given sufficient time, stochastically build a nucleus exceeding the critical size. Crossing this threshold makes further growth energetically favorable and, given a sufficient reservoir of material, monomeric attachment of growth units continues unabated as illustrated in Figure 1.1. An example of alternative theories to CNT is well illustrated by recent studies in calcium carbonate crystallization. Titration and analytical ultracentrifugation data have served as the basis for proposing that a stable population of multi-ion 'pre-nucleation clusters' exist [18] in the $CaCO_3$ system, and that these clusters aggregate to form an amorphous precursor phase that subsequently transforms into one of the anhydrous crystalline phases. Supporting evidence for the existence of these clusters came from cryogenic transmission electron microscopy (cryo-TEM) [19], although these data could not establish whether these were stable clusters or transient species arising from the density fluctuations described by CNT; nor could they verify a link between the observed clusters and later nuclei. Alternatively — or in addition to the clusters — a metastable, bicarbonate-rich dense liquid precursor phase has been proposed based on NMR data, as forming prior to the appearance of a solid phase [20]. In silico approaches have suggested that highly dynamic clusters form [21], followed by spinodal decomposition driving a liquid-liquid phase separation [22] at moderate supersaturations. The solid phase was then reasoned to form via amorphous calcium carbonate (ACC) generation through dehydration of the denser liquid droplets. In addition, ACC has been frequently observed as the initially formed phase [23] that eventually ends up as one of the crystalline phases [24]. Despite many attempts, however, ex situ electron microscopy [19], x-ray spectroscopy [16], and in situ x-ray [5, 13] studies have failed to determine whether the ACC to crystal transformation occurred through dissolution-reprecipitation or direct phase transformation.

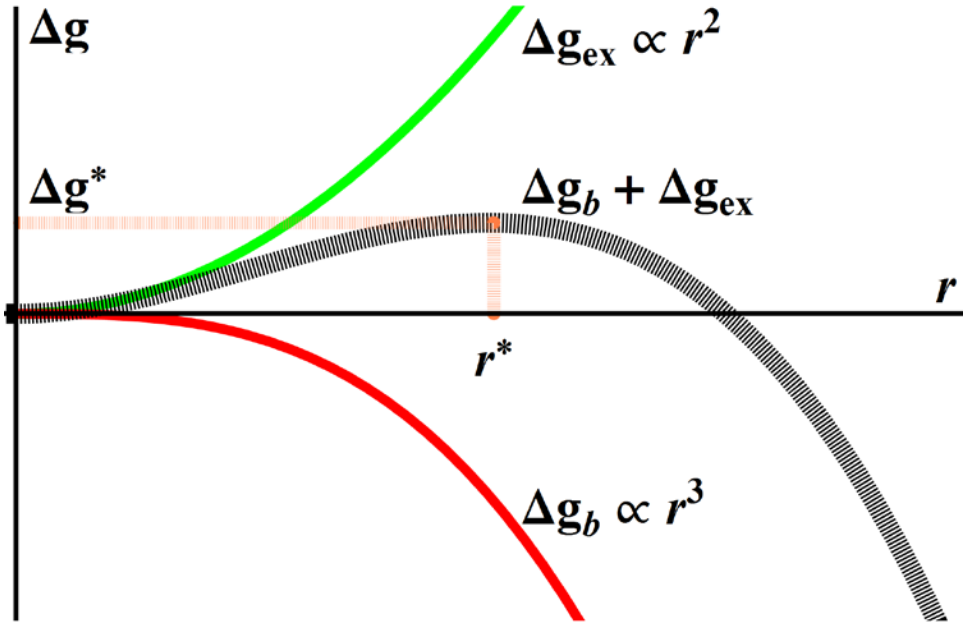

Figure 1.1 Classical Nucleation Theory predicts an energy barrier to nucleation arising from the combination of the energetically favorable creation of volume in the new phase, which scales as r^3 and the unfavorable creation of a surface between the old and new phases, which scales as r^2.

Complex mineral nucleation pathways involving cluster aggregation and transformation of precursor phases have also been observed in other systems. Calcium phosphate, for example, has been suggested, based on cryo-TEM and in situ scanned probe microscopy data, to form through the initial development of an extended network of nanometer-sized amorphous particles which then undergo sequential chemical, structural, and morphological transformations to produce the final crystalline phase [25]. However, because the characterization tools lacked the capability of directly observing particle formation and evolution through the proposed pathway, the results are open to other interpretations.

Looking beyond nucleation mechanisms, processes governing crystal growth are also poorly understood. While the predictions of well-developed classical theories accurately describe growth in many systems as proceeding via monomer-by-monomer attachment, they fail to correctly portray growth in other systems. Particle-based growth mechanisms provide a clear illustration of this point. It was discovered that TiO_2 primary particles attached on specific crystallographic faces, a process that has come to be called “oriented attachment,” yielding complex single crystals [26]. In the years since those findings, particle-based mechanisms have been recognized as perhaps dominant in numerous biological, environmental, and synthetic systems, particularly semiconductor nanoparticles and nanowires with complex topologies [27]. Particle attachment mechanisms need not proceed through alignment along perfect crystallographic registry. Attachment at slightly misaligned orientations [28] may precede crystal relaxation that expels defects from the structure to result in a well-ordered single crystal [29]. Furthermore, attaching particles may not even be of a uniform phase. Instead, a phase that is metastable, or stable only at the nanoscale, attaches to the surface of a crystal of the stable bulk phase, followed by recrystallization of the attached particle to yield a single crystal [30-32]. The

resulting crystals from any of the above examples of particle-based mechanisms may contain scant, if any, signature of the pathway by which they were produced. Additionally, most experimental data used to infer such particle-based pathways have been produced by ex situ techniques.

With this context established, the need for in situ techniques capable of resolving crystallization processes at time and length scales appropriate to catch the early stages of particle formation, is clear. The above-mentioned and many similar studies, some of which may be controversial or inconclusive, suggest a multitude of mechanisms contribute to nucleation and growth depending on material system and precipitation conditions. Thus, in order to truly understand the physics behind such non-classical mechanisms and develop a complete picture of materials formation, identifying which processes are active is of paramount importance. Direct observation of these phenomena and the rates at which they proceed would additionally provide quantitative insight into the energetics of nucleation and growth, as formation pathways depend on energy barriers between initial and final states, changes in free energy, and gradients in interaction potentials. The recent advent of liquid phase TEM provides an experimental technique that allows such direct observations. The ability of this characterization tool to acquire both imaging and crystallographic data renders it an invaluable tool for advancing knowledge of crystallization processes.

1.2 Calcium Carbonate

The research contained in the following chapters of this dissertation revolves around the formation of calcium carbonate as a model system by which to understand phenomena occurring throughout the early stages of mineralization. While Section 1.1 introduced some of the issues regarding the interest in this system, a few of the many open questions around $CaCO_3$ formation bear emphasizing here. Which of the observed phases or proposed precursors are active participants in crystallization? While calcite is the thermodynamically stable phase under typical laboratory conditions as shown below in Figure 1.2A, other anhydrous and hydrated crystalline phases exist [33-35], as do one [23] or multiple [15, 36, 37] amorphous phases. The major $CaCO_3$ phases exhibiting their typical morphologies are shown below in Figure 1.3. Additional precursors such as pre-nucleation clusters and dense liquid droplets have also been proposed. With this collection of phases, does the classical picture of direct calcite nucleation from solution occurring through monomeric addition to a nascent calcite crystal accurately reflect the actual process? Does Ostwald's Rule of Stages [38, 39] more accurately reflect nucleation, with smaller kinetic barriers resulting in a progression of increasingly stable phases from amorphous to calcite? Or are these classical ideas insufficient because they don't take into account additional precursor species or states that are crucial to the process?

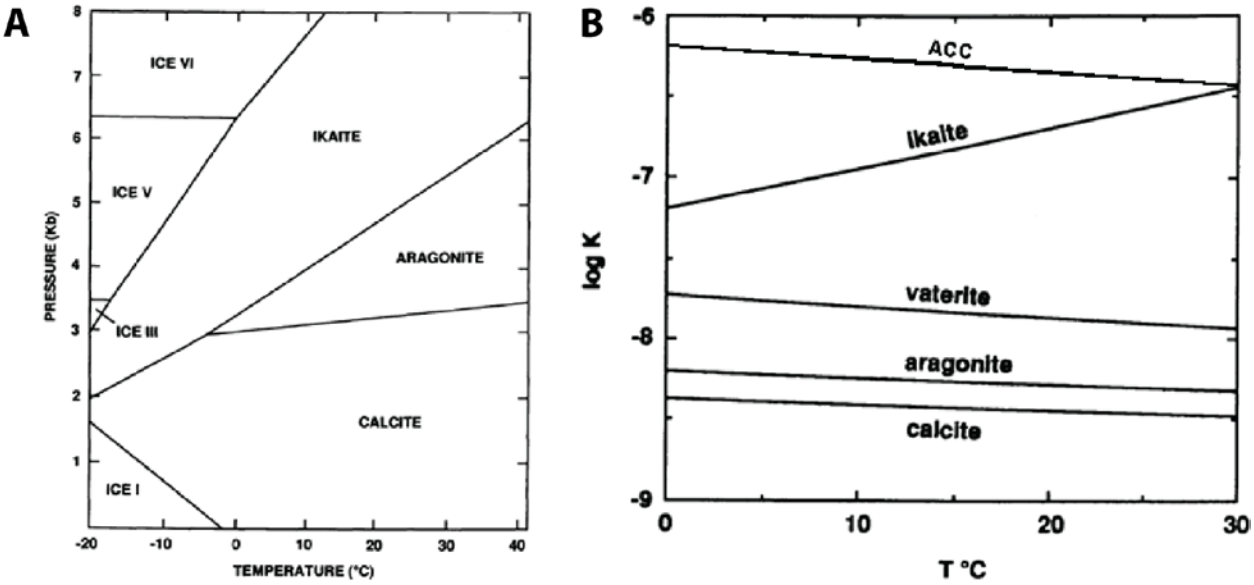

Figure 1.2 (A) P-T phase diagram of water-saturated $CaCO_3$ system [43]. (B) Solubilities of the major $CaCO_3$ phases (modified from [43] with ACC data from [23]).

Part of the reason for the seemingly complicated landscape in mineral systems such as calcium carbonate is the existence of multiple crystalline polymorphs with similar solubilities, as shown in Figure 1.2B, and relatively large interfacial energies. Due to the latter, in order to study nucleation of these materials on a manageable experimental time-scale the solution must be driven to high supersaturation, which results in multiple phases and pathways becoming thermodynamically available. In the $CaCO_3$ system where the interfacial free energy is over $100 mJ/m^2$, even when the concentration is raised to the solubility limit of the amorphous phase so that all four of the common polymorphs are stable with respect to the dissolved state, the free energy barrier to forming calcite, which is the most stable phase, is still on the order of 100 $\mathbf{k}T$ [3]. Hence pathways can be complex.

As introduced in above Section 1.1, calcium carbonate is a much studied mineral system due to its relevance in, among other fields, biomineralization [44]. Living organisms exert biological control over crystallization of hard materials through the use of a scaffold of macromolecules that is often referred to as the organic matrix. The matrix is believed to play an active role in directing nucleation of the mineral phase by presenting a template that controls the location and orientation of the individual crystallites [44-46]. The hierarchical structure and mechanical properties made possible through matrix-mediated mineralization are beyond the reach of laboratory synthesis [47]. Such an inclusion of an organic matrix into the mineral system, either as a solid template or dispersed in solution, raises additional questions, including: How do organic matrices such as those found in biomineral systems affect the early stages of $CaCO_3$ formation? Achieving a mechanistic understanding of this phenomenon is of interest for development of new approaches to materials synthesis, and thus a great deal of research has been directed towards creating model matrices for that purpose.

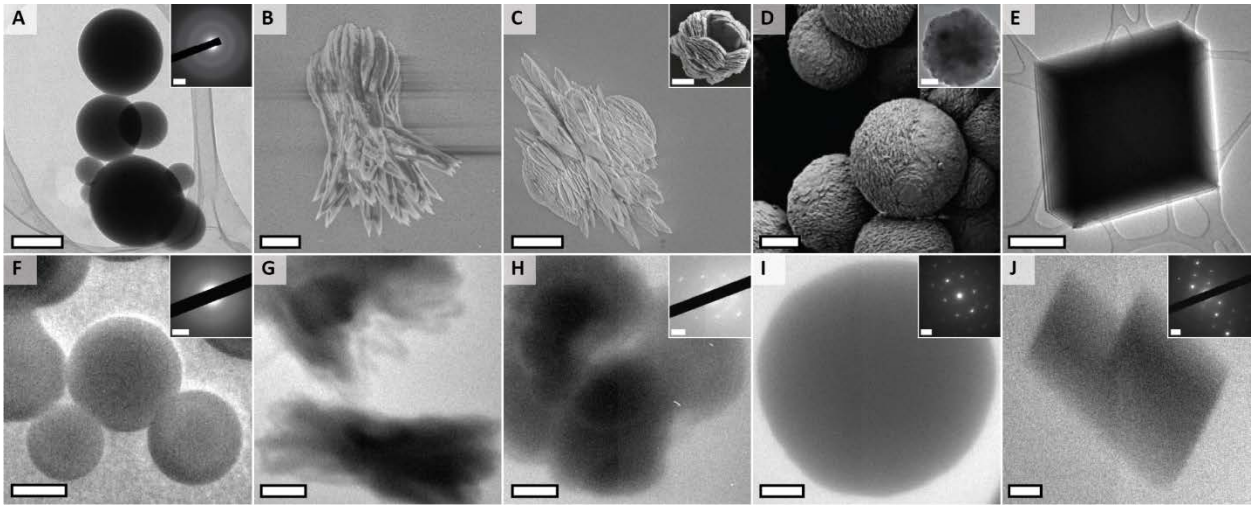

Figure 1.3 Common morphologies of major $CaCO_3$ phases. Collection of ex situ and in situ images and diffraction data showing typical morphologies and projections of various phases of $CaCO_3$. TEM image and diffraction (A and inset, respectively) of ACC particles on a carbon film, with in situ comparison (F and inset, respectively) in liquid cell. SEM image (B) of aragonite "sheaf-of-wheat" bundle, compared to structure imaged in TEM liquid cell (G). SEM images of vaterite floret (C) and 'cauliflower' vaterite structure (C inset, [40] – Reproduced by permission of The American Chemical Society), and in situ TEM image with diffraction of polycrystalline vaterite plates (H and inset, respectively) in liquid cell. SEM image (D, [41] – Reproduced by permission of The Royal Society of Chemistry) of vaterite sphere and ex situ TEM image (D inset, [42] – Reproduced by permission of The Royal Society of Chemistry) of vaterite plate. In situ TEM image and diffraction pattern of vaterite with the primary pattern the [22-1] zone axis (I and inset, respectively) in liquid cell. Ex situ TEM image (E) of calcite rhombohedron on a carbon film, and in situ TEM image with diffraction data from near the [110] zone axis (J and inset, respectively), of similar calcite rhombohedron in liquid cell. Scale bars are: 200 nm (A, D inset, J), 2 μm (B, D), 5 μm (C), 20 μm (C inset), 500 nm (E-G), 1 μm (H, I), and 2 nm^{-1} (diffraction insets).

1.3 Model Templating Surfaces

Early studies of crystal templating [48-51] used Langmuir monolayers with specific head-group chemistries as simple biomimetic systems to look at the effect of organic films on nucleation of inorganic crystals. These studies found that compressed monolayers induced oriented nucleation of $CaCO_3$ and $BaSO_4$ on specific faces dependent on chemical functionality at the organic-inorganic interface. In the case of vaterite on stearate there was no epitaxial match between the nucleating face and the organic template and the authors concluded that stereochemical and electrostatic matching override the lattice mismatch. In addition they observed that partially compressed monolayers produced the best control over vaterite nucleation, and suggested that scaffolds that can undergo conformational changes in the presence of the mineral may provide the highest control over mineralization. For calcite on stearate and sulfonated films, and $BaSO_4$ on sulfate and phosphonate monolayers, although they observed

lattice matching at the interface of the organic and mineral phases, selection of a single crystal nucleation plane was attributed to stereochemical matching between the template head-group chemistries and the nucleating face. Adding to these findings Berman *et al.* [52] demonstrated that calcite nuclei were co-aligned with respect to the conjugated backbone of a polydiacetylene Langmuir monolayer on a solid support, and that the alkyl side chains of the supported organic film reorganized during mineralization to optimize the stereochemical fit to the calcite structure.

Aizenberg *et al.* [53, 54] showed that organothiol SAMs exhibiting surface functional groups commonly expressed on biomolecules generated well-defined calcite crystal orientations, narrowly distributed crystal sizes, and a pattern of nucleation dependent on the location of these functional groups. They demonstrated that by varying either the terminal groups on SAMs of alkane thiols or the underlying noble metal substrate one could precisely control the plane of nucleation of calcite, and found that the geometry of the SAM functional groups was the primary factor in controlling the orientation of the calcite nuclei. Travaille *et al.* [55] showed a 1:1 relationship along one direction between the underlying Au structure and in-plane orientation of the templated crystals. Han and Aizenberg [56] extended Aizenberg's earlier studies to systematically explore the effects of SAM alkyl chain parity and material of the underlying substrate on calcite nucleation. Through these studies they showed the nucleation plane depended strongly on a combination of three aspects of the template: packing geometry of the templating surface, head-group chemistry and orientation of the functional group.

These observations led to the idea that directed growth is determined at the initial stage of nucleation where the nucleus contacts specifically with the functional groups of the organic interface to develop into a specific polymorph and orientation. Figure 1.4 shows this schematically, with the SAM a well-ordered template with which the solvated mineral comes into close proximity, aligns into some energetically favorable configuration with respect to the organic template, and crystallizes into its energetically favorable phase. However, a quantitative understanding of the energetic drivers underlying the process and knowledge about the phase pathway that the mineral underwent during crystallization were lacking. Thus the above studies set the context for three key questions regarding oriented nucleation on templates: 1) What is the pathway taken by the mineralizing constituents from the solvated state to the final, energetically stable phase? 2) How does the presence of the organic surface affect the energetics of mineralization; that is, is templated nucleation driven by thermodynamics through reduction of interfacial energy or kinetics through reduction of activation barriers and by how much are they reduced? 3) Are the predictions of Classical Nucleation Theory accurate in describing nucleation in this system?

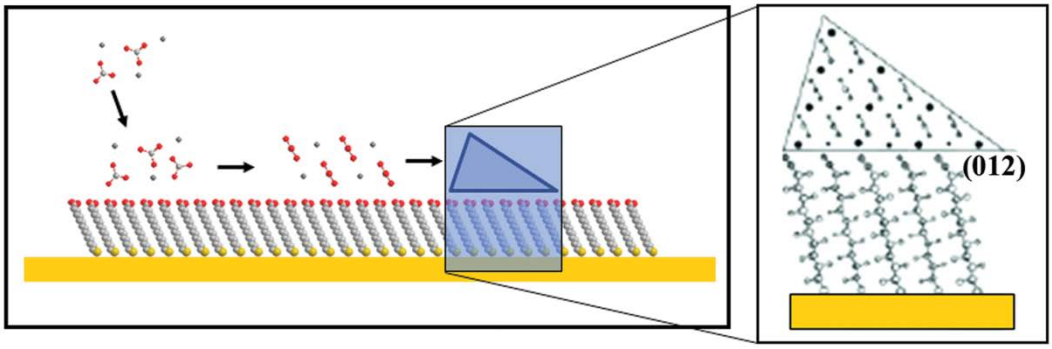

Figure 1.4 Possible nucleation pathway for calcite forming on an alkanethiol SAM. The initial state consists of a well-ordered SAM assembled on an underlying substrate submerged in a supersaturated calcium carbonate solution. A suitable number of ions to constitute a critical nucleus organize at the organic-solution interface into an energetically favorable arrangement and crystallizes, with the calcite crystal oriented by the underlying SAM.

1.4 Looking Ahead

The research presented in this dissertation combines multiple in situ characterization approaches to address open questions around the nucleation of calcium carbonate, both in the presence and absence of organic templates. In Chapter 2, low resolution optical microscopy is used to provide an indirect method of measuring nucleation rates, from which the predictions of Classical Nucleation Theory are tested. Furthermore, SAM-templated calcite formation pathways are investigated by optical and scanned probe microscopies, to provide a baseline by which to compare the results of techniques which allow direct measurement. The development of a liquid phase TEM platform, which provides a means of observing nucleation phenomena at time and length scales relevant to the phase transformation, is detailed in Chapter 3, along with a discussion of various measurements of nanocrystal formation and transformation processes. Chapter 4 presents direct observations of $CaCO_3$ formation pathways in a pure mineral system, using a continuous flow liquid phase TEM stage, and Chapter 5 includes a discussion of extending the technique to look at $CaCO_3$ formation pathways on a SAM template.

1.5 References

1. A. H. Knoll, in *Biomineralization*, P. M. Dove, J. J. DeYoreo, S. Weiner, Eds. (2003), vol. 54, pp. 329-356.

2. Y. Yin, A. P. Alivisatos, Colloidal nanocrystal synthesis and the organic-inorganic interface. *Nature* **437**, 664-670 (2005). doi:

3. Q. Hu, M. H. Nielsen, C. L. Freeman, L. M. Hamm, J. Tao, J. R. I. Lee, T. Y. J. Han, U. Becker, J. H. Harding, P. M. Dove, J. J. De Yoreo, The thermodynamics of calcite

nucleation at organic interfaces: Classical vs. non-classical pathways. *Faraday Discuss.* **159**, 509-523 (2012). doi:10.1039/c2fd20124k

4. A. Verch, I. E. G. Morrison, R. van de Locht, R. Kroger, In situ electron microscopy studies of calcium carbonate precipitation from aqueous solution with and without organic additives. *Journal of Structural Biology* **183**, 270-277 (2013). doi:10.1016/j.jsb.2013.05.017

5. J. Rieger, J. Thieme, C. Schmidt, Study of precipitation reactions by x-ray microscopy: $CaCO_3$ precipitation and the effect of polycarboxylates. *Langmuir* **16**, 8300-8305 (2000). doi:10.1021/la0004193

6. T. Ando, N. Kodera, E. Takai, D. Maruyama, K. Saito, A. Toda, A high-speed atomic force microscope for studying biological macromolecules. *Proceedings of the National Academy of Sciences* **98**, 12468-12472 (2001). doi:10.1073/pnas.211400898

7. P. J. M. Smeets, K. R. Cho, R. G. E. Kempen, N. A. J. M. Sommerdijk, J. J. De Yoreo, Calcium carbonate nucleation driven by ion binding in a biomimetic matrix revealed by in situ electron microscopy. *Nat. Mater.* **14**, 394-399 (2015). doi:10.1038/nmat4193

8. C. C. Tester, R. E. Brock, C. H. Wu, M. R. Krejci, S. Weigand, D. Joester, In vitro synthesis and stabilization of amorphous calcium carbonate (ACC) nanoparticles within liposomes. *Crystengcomm* **13**, 3975-3978 (2011). doi:10.1039/c1ce05153a

9. P. A. Fang, J. F. Conway, H. C. Margolis, J. P. Simmer, E. Beniash, Hierarchical self-assembly of amelogenin and the regulation of biomineralization at the nanoscale. *Proceedings of the National Academy of Sciences of the United States of America* **108**, 14097-14102 (2011). doi:10.1073/pnas.1106228108

10. F. Nudelman, K. Pieterse, A. George, P. H. H. Bomans, H. Friedrich, L. J. Brylka, P. A. J. Hilbers, G. de With, N. Sommerdijk, The role of collagen in bone apatite formation in the presence of hydroxyapatite nucleation inhibitors. *Nat. Mater.* **9**, 1004-1009 (2010). doi:10.1038/nmat2875

11. A. J. Giuffre, L. M. Hamm, N. Han, J. J. De Yoreo, P. M. Dove, Polysaccharide chemistry regulates kinetics of calcite nucleation through competition of interfacial energies. *Proceedings of the National Academy of Sciences* **110**, 9261-9266 (2013). doi:10.1073/pnas.1222162110

12. L. M. Hamm, A. J. Giuffre, N. Han, J. Tao, D. Wang, J. J. De Yoreo, P. M. Dove, Reconciling disparate views of template-directed nucleation through measurement of calcite nucleation kinetics and binding energies. *Proceedings of the National Academy of Sciences* **111**, 1304-1309 (2014). doi:10.1073/pnas.1312369111

13. P. Bots, L. G. Benning, J. D. Rodriguez-Blanco, T. Roncal-Herrero, S. Shaw, Mechanistic insights into the crystallization of amorphous calcium carbonate (ACC). *Crystal Growth & Design* **12**, 3806-3814 (2012). doi:10.1021/cg300676b

14. J. Rieger, T. Frechen, G. Cox, W. Heckmann, C. Schmidt, J. Thieme, Precursor structures in the crystallization/precipitation processes of $CaCO_3$ and control of particle formation by polyelectrolytes. *Faraday Discuss.* **136**, 265-277 (2007). doi:10.1039/b701450c

15. A. V. Radha, T. Z. Forbes, C. E. Killian, P. Gilbert, A. Navrotsky, Transformation and crystallization energetics of synthetic and biogenic amorphous calcium carbonate. *Proceedings of the National Academy of Sciences of the United States of America* **107**, 16438-16443 (2010). doi:10.1073/pnas.1009959107

16. J. R. I. Lee, T. Y. J. Han, T. M. Willey, D. Wang, R. W. Meulenberg, J. Nilsson, P. M. Dove, L. J. Terminello, T. van Buuren, J. J. De Yoreo, Structural development of mercaptophenol self-assembled monolayers and the overlying mineral phase during templated $CaCO_3$ crystallization from a transient amorphous film. *J. Am. Chem. Soc.* **129**, 10370-10381 (2007). doi:10.1021/ja071535w

17. J. W. Gibbs, On the equilibrium of heterogeneous substances. *Transactions of the Connecticut Academy of Arts and Sciences* **3**, 108-248 (1876); 343-524 (1878).

18. D. Gebauer, A. Völkel, H. Cölfen, Stable prenucleation calcium carbonate clusters. *Science* **322**, 1819–1822 (2008). doi:10.1126/science.1164271

19. E. M. Pouget, P. H. Bomans, J. A. Goos, P. M. Frederik, G. de With, N. A. Sommerdijk, The initial stages of template-controlled $CaCO_3$ formation revealed by cryo-TEM. *Science* **323**, 1455–1458 (2009). doi:10.1126/science.1169434

20. M. A. Bewernitz, D. Gebauer, J. Long, H. Cölfen, L. B. Gower, A metastable liquid precursor phase of calcium carbonate and its interactions with polyaspartate. *Faraday Discussions* **159**, 291–312 (2012). doi:10.1039/c2fd20080e

21. R. Demichelis, P. Raiteri, J. D. Gale, D. Quigley, D. Gebauer, Stable prenucleation mineral clusters are liquid-like ionic polymers. *Nature Communications* **2**, 590 (2011). doi:10.1038/ncomms1604

22. A. F. Wallace, L. O. Hedges, A. Fernandez-Martinez, P. Raiteri, J. D. Gale, G. A. Waychunas, S. Whitelam, J. F. Banfield, J. J. De Yoreo, Microscopic evidence for liquid-liquid separation in supersaturated $CaCO_3$ solutions. *Science* **341**, 885–889 (2013). doi:10.1126/science.1230915

23. L. Brečević, A. E. Nielsen, Solubility of amorphous calcium carbonate. *Journal of Crystal Growth* **98**, 504–510 (1989). doi:10.1016/0022-0248(89)90168-1

24. A. Gal, W. Habraken, D. Gur, P. Fratzl, S. Weiner, L. Addadi, Calcite crystal growth by a solid-state transformation of stabilized amorphous calcium carbonate nanospheres in a hydrogel. *Angew. Chem.-Int. Edit.* **52**, 4867-4870 (2013). doi:10.1002/anie.201210329

25. W. Habraken, J. H. Tao, L. J. Brylka, H. Friedrich, L. Bertinetti, A. S. Schenk, A. Verch, V. Dmitrovic, P. H. H. Bomans, P. M. Frederik, J. Laven, P. van der Schoot, B. Aichmayer, G. de With, J. J. DeYoreo, N. Sommerdijk, Ion-association complexes unite classical and non-classical theories for the biomimetic nucleation of calcium phosphate. *Nature Communications* **4**, 1507 (2013). doi:10.1038/ncomms2490

26. R. L. Penn, J. F. Banfield, Oriented attachment and growth, twinning, polytypism, and formation of metastable phases: Insights from nanocrystalline TiO_2. *American Mineralogist* **83**, 1077-1082 (1998). doi:

27. R. L. Penn, Kinetics of oriented aggregation. *The Journal of Physical Chemistry B* **108**, 12707-12712 (2004). doi:10.1021/jp036490+

28. R. L. Penn, J. F. Banfield, Imperfect oriented attachment: Dislocation generation in defect-free nanocrystals. *Science* **281**, 969-971 (1998). doi:10.1126/science.281.5379.969

29. D. S. Li, M. H. Nielsen, J. R. I. Lee, C. Frandsen, J. F. Banfield, J. J. De Yoreo, Direction-specific interactions control crystal growth by oriented attachment. *Science* **336**, 1014-1018 (2012). doi:10.1126/science.1219643

30. J. Baumgartner, A. Dey, P. H. H. Bomans, C. Le Coadou, P. Fratzl, N. Sommerdijk, D. Faivre, Nucleation and growth of magnetite from solution. *Nat. Mater.* **12**, 310-314 (2013). doi:10.1038/nmat3558

31. C. Frandsen, B. A. Legg, L. R. Comolli, H. Z. Zhang, B. Gilbert, E. Johnson, J. F. Banfield, Aggregation-induced growth and transformation of beta-FeOOH nanorods to micron-sized alpha-Fe_2O_3 spindles. *Crystengcomm* **16**, 1451-1458 (2014). doi:10.1039/c3ce40983j

32. M. H. Nielsen, D. S. Li, H. Z. Zhang, S. Aloni, T. Y. J. Han, C. Frandsen, J. Seto, J. F. Banfield, H. Colfen, J. J. De Yoreo, Investigating processes of nanocrystal formation and transformation via liquid cell TEM. *Microsc. microanal.* **20**, 425-436 (2014). doi:10.1017/s1431927614000294

33. J. Johnston, H. E. Merwin, E. D. Williamson, The several forms of calcium carbonate. *American Journal of Science* **41**, 473-512 (1916). doi:

34. F. Krauss, W. Schriever, The hydrates of calcium carbonate. *Zeitschrift Fur Anorganische Und Allgemeine Chemie* **188**, 259-260 (1930). doi:10.1002/zaac.19301880122

35. R. Brooks, L. M. Clark, E. F. Thurston, Calcium carbonate and its hydrates. *Philosophical Transactions of the Royal Society of London Series a-Mathematical and Physical Sciences* **243**, 145-167 (1950). doi:10.1098/rsta.1950.0016

36. N. Koga, Y. Yamane, Thermal behaviors of amorphous calcium carbonates prepared in aqueous and ethanol media. *Journal of Thermal Analysis and Calorimetry* **94**, 379-387 (2008). doi:10.1007/s10973-008-9110-3

37. D. Gebauer, P. N. Gunawidjaja, J. Y. P. Ko, Z. Bacsik, B. Aziz, L. J. Liu, Y. F. Hu, L. Bergstrom, C. W. Tai, T. K. Sham, M. Eden, N. Hedin, Proto-calcite and proto-vaterite in amorphous calcium carbonates. *Angew. Chem.-Int. Edit.* **49**, 8889-8891 (2010). doi:10.1002/anie.201003220

38. P. T. Cardew, R. J. Davey, The kinetics of solvent-mediated phase transformations. *Proc. R. Soc. London Ser. A-Math. Phys. Eng. Sci.* **398**, 415-428 (1985). doi:10.1098/rspa.1985.0043

39. P. W. Voorhees, The theory of ostwald ripening. *J. Stat. Phys.* **38**, 231-252 (1985). doi:10.1007/bf01017860

40. J. Gómez-Morales, A. Hernandez-Hernandez, G. Sazaki, J. M. Garcia-Ruiz, Nucleation and polymorphism of calcium carbonate by a vapor diffusion sitting drop crystallization technique. *Crystal Growth & Design* **10**, 963–969 (2010). doi:10.1021/cg901279t

41. J. P. Andreassen, R. Beck, M. Nergaard, Biomimetic type morphologies of calcium carbonate grown in absence of additives. *Faraday Discussions* **159**, 247–261 (2012). doi:10.1039/c2fd20056b

42. J. Ahmed, A. K. Menaka, A. K. Ganguli, Controlled growth of nanocrystalline rods, hexagonal plates and spherical particles of the vaterite form of calcium carbonate. *CrystEngComm* **11**, 927–932 (2009). doi:10.1039/b820928f

43. J. L. Bischoff, J. A. Fitzpatrick, R. J. Rosenbauer, The solubility and stabilization of ikaite ($CaCO_3.6H_2O$) from 0 - 25 C: Environmental and paleoclimatic implications for thinolite tufa. *J. Geol.* **101**, 21-33 (1993). doi:

44. J. R. Young, K. Henriksen, in *Biomineralization*, P. M. Dove, J. J. DeYoreo, S. Weiner, Eds. (Mineralogical Soc Amer, Chantilly, 2003), vol. 54, pp. 189-215.

45. J. R. Young, J. M. Didymus, P. R. Bown, B. Prins, S. Mann, Crystal assembly and phylogenetic evolution in heterococcoliths. *Nature* **356**, 516-518 (1992). doi:

46. S. Mann, Molecular tectonics in biomineralization and biomimetic materials chemistry. *Nature* **365**, 499-505 (1993). doi:10.1038/365499a0

47. J. Aizenberg, Crystallization in patterns: A bio-inspired approach. *Advanced Materials* **16**, 1295-1302 (2004). doi:10.1002/adma.200400759

48. S. Mann, B. R. Heywood, S. Rajam, J. D. Birchall, Controlled crystallization of $CaCO_3$ under stearic acid monolayers. *Nature* **334**, 692-695 (1988). doi:

49. S. Mann, D. D. Archibald, J. M. Didymus, T. Douglas, B. R. Heywood, F. C. Meldrum, N. J. Reeves, Crystallization at inorganic-organic interfaces - biominerals and biomimetic synthesis. *Science* **261**, 1286-1292 (1993). doi:10.1126/science.261.5126.1286

50. B. R. Heywood, S. Rajam, S. Mann, Oriented crystallization of $CaCO_3$ under compressed monolayers 2. Morphology, structure and growth of immature crystals. *Journal of the Chemical Society-Faraday Transactions* **87**, 735-743 (1991). doi:10.1039/ft9918700735

51. S. Rajam, B. R. Heywood, J. B. A. Walker, S. Mann, R. J. Davey, J. D. Birchall, Oriented crystallization of $CaCO_3$ under compressed monolayers 1. Morphological studies of mature crystals. *Journal of the Chemical Society-Faraday Transactions* **87**, 727-734 (1991). doi:

52. A. Berman, D. J. Ahn, A. Lio, M. Salmeron, A. Reichert, D. Charych, Total alignment of calcite at acidic polydiacetylene films - cooperativity at the organic-inorganic interface. *Science* **269**, 515-518 (1995). doi:10.1126/science.269.5223.515

53. J. Aizenberg, A. J. Black, G. M. Whitesides, Control of crystal nucleation by patterned self-assembled monolayers. *Nature* **398**, 495-498 (1999). doi:10.1038/19047

54. J. Aizenberg, A. J. Black, G. M. Whitesides, Oriented growth of calcite controlled by self-assembled monolayers of functionalized alkanethiols supported on gold and silver. *J. Am. Chem. Soc.* **121**, 4500-4509 (1999). doi:10.1021/ja984254k

55. A. M. Travaille, J. Donners, J. W. Gerritsen, N. Sommerdijk, R. J. M. Nolte, H. van Kempen, Aligned growth of calcite crystals on a self-assembled monolayer. *Adv. Mater.*

14, 492-495 (2002). doi:10.1002/1521-4095(20020404)14:7<492::aid-adma492>3.0.co;2-l

56. Y. J. Han, J. Aizenberg, Face-selective nucleation of calcite on self-assembled monolayers of alkanethiols: Effect of the parity of the alkyl chain. *Angew. Chem.-Int. Edit.* **42**, 3668-3670 (2003). doi:10.1002/anie.200351655

Chapter 2

The Thermodynamics of Calcite Nucleation at Organic Interfaces: Classical vs. Non-Classical Pathways

Nucleation in the natural world often occurs in the presence of organic interfaces. In mineralized tissues, a range of macromolecular matrices are found in contact with inorganic phases and are believed to direct mineral formation. In geochemical settings, mineral surfaces, which are often covered with organic or biological films, surround the volume within which nucleation occurs. In the classical picture of nucleation, the presence of such interfaces is expected to have a profound effect on nucleation rates, simply because they can reduce the interfacial free energy, which controls the height of the thermodynamic barrier to nucleation of the solid phase. However, the recent discovery of a nearly monodisperse population of calcium carbonate clusters – so called prenucleation clusters – and the many observations of amorphous precursor phases have called into question the applicability of classical descriptions. In this chapter in situ observations of nucleation on organothiol self-assembled monolayers (SAMs) are used to explore the energetics and pathways of calcite nucleation at organic interfaces. Carboxyl SAM-directed nucleation is found to be described well in purely classical terms through a reduction in the thermodynamic barrier due to decreased interfacial free energy. Moreover, the differences in nucleation kinetics on odd and even chain-length carboxyl SAMs are attributable to relative differences in these energies. In addition, amorphous particles formed prior to or during crystal nucleation do not grow and are not observed to act as precursors to the crystalline phase. Instead, calcite appears to nucleate independently. These results imply that the recently proposed model of calcite formation as a non-classical process, one which proceeds via aggregation of stable pre-nucleation clusters that form an amorphous precursor from which the crystalline phase emerges, is not applicable to template-directed nucleation on carboxyl SAMs and does not provide a universal description of calcite formation.

2.1 Introduction

Macromolecular matrices play a key role in establishing the architectural complexity and mechanical properties of biominerals by directing the organization of the mineralized component [1–3]. The ability of the matrix to perform this function is determined by both its structural relationship with the incipient nucleus [4] and the changes to the energy landscape it imposes upon the mineralizing constituents [5]. A number of studies have explored the structural aspect [1–4, 6, 7], but little is known about the energetic controls. Moreover, the recent discovery that

calcium carbonate [8] and phosphate [4] solutions contain clusters prior to nucleation—i.e., pre-nucleation clusters—that seem to be stable relative to the free ions [8] combined with observations of non-equilibrium amorphous precursors in numerous biomineral [1, 9, 10] and biomimetic systems [11–13], raises the question of whether the classical description [5] of nucleation dynamics is applicable to matrix-directed mineralization. This same question arises when considering mineral nucleation in geochemical settings where a surrounding mineral matrix, which is often coated with biofilms or other organic layers, is likely to influence nucleation kinetics. While these issues are difficult to address in the context of three-dimensional biological matrices or geological reservoirs, self-assembled monolayers (SAMs) of organothiols on noble metal surfaces, which can template mineral nucleation on distinct crystallographic planes with a high degree of specificity, offer an excellent 2D model [12, 14–17].

This chapter discusses the use of carboxyl- and hydroxyl-terminated SAMs to investigate the energetics and formation pathways during templated nucleation of $CaCO_3$. To begin, the basic relationships between the rate of calcite nucleation and the supersaturation are developed for three classes of free energy landscapes, including both size independent and size dependent excess free energies, as well as one in which local or global minima create a population of pre-nucleation clusters. An in situ optical microscopy method to measure nucleation rates as a function of supersaturation on SAMs is then utilized, from which is derived the effective interfacial energies. The resulting free energy barriers for heterogeneous nucleation on carboxyl-terminated SAMs containing carbon chains of odd and even length are compared to that expected for homogeneous nucleation in bulk solution. Finally a combination of in situ optical microscopy and atomic force microscopy (AFM) observations along with Raman and transmission electron microscopy (TEM) analyses are employed to follow the pathway of calcite formation on both the carboxyl- and hydroxyl-terminated SAMs.

Theoretical analysis shows that homogeneous nucleation of calcite is highly unlikely even at concentrations approaching the solubility limit of amorphous calcium carbonate (ACC). However, introduction of a size dependent interfacial energy, the introduction of low-energy surfaces and a population of metastable clusters can all significantly reduce the barrier. Based on the measurements of nucleation rates, nucleation on carboxyl-terminated SAMs is found to be described well in purely classical terms through a reduction in the thermodynamic barrier due to decreased interfacial free energy. The differences in nucleation kinetics on carboxyl-terminated SAMs of odd and even parity—i.e., an odd number, 11, vs. an even number, 16, of carbons in the alkyl chain—are attributable to relative differences in these energies that arise from varying degrees of SAM order related to oxygen-oxygen interactions between SAM headgroups. In addition, amorphous particles observed to form prior to crystal nucleation on hydroxyl SAMs and after crystal nucleation on carboxyl SAMs—even well below the accepted bulk solubility limit for ACC—do not grow and are not observed to be precursors to the crystalline phase. Instead, calcite appears to nucleate independently. A discussion follows for how these results can be reconciled with the recently proposed non-classical picture of calcite formation that is based on aggregation of stable or metastable pre-nucleation clusters [8, 11].

2.2 Theory

2.2.1 Homogeneous Nucleation of Calcite and ACC

In principle, the energetic effect of any surface on nucleation can be determined by measuring the dependence of nucleation rate on supersaturation [5, 18]. In all nucleation events, two important energetic parameters influence rates. The first is the excess free energy associated with the newly formed phase. This is an ensemble property that creates a thermodynamic barrier Δg_c due to the collective behavior of the ions in the solid and liquid phases. The second is an effective kinetic barrier E_A arising from individual reactions such as desolvation of solute ions, attachment to the forming nucleus, and structural rearrangements. Both barriers appear exponentially in the expression for the rate of nucleation J_n through [5]:

$$J_n = Ae^{-E_A/\mathbf{k}T}e^{-\Delta g_c/\mathbf{k}T} \tag{2.1}$$

where A is a pre-factor that is determined by geometric factors and material-dependent parameters (e.g. density) and Δg_c is a decreasing function of the chemical potential $\Delta\mu = \mathbf{k}T\sigma$, where σ is the supersaturation (defined as the log of the ion activity product over the equilibrium constant, which, for $CaCO_3$, looks as follows: $\sigma = \ln\left[(\{Ca^{2+}\}\{CO_3^{2-}\})/K_{sp}\right]$), **k** is Boltzmann's constant and T is the temperature.

While the exponential dependence of J_n on σ through the free energy barrier is a universal hallmark of nucleation that, in essence, distinguishes it from a simple chemical reaction, the exact form of A and Δg_c are model dependent. The source of Δg_c is a positive excess free energy Δg_{ex} of the solid phase that adds to the change in free energy for a simple chemical reaction, which is simply given by $(dg/dn)\Delta n$ where Δn is the number of molecules passing from the solution to the solid phase. For a supersaturated solution, $dg/dn < 0$. Thus without Δg_{ex} there would be no barrier and precipitation would happen spontaneously at infinitesimal supersaturation without nucleation. In classical nucleation theory (CNT), Δg_{ex} arises from the free energy of the interface between the mineral and the surrounding solvent and substrate (Figure 2.1A).

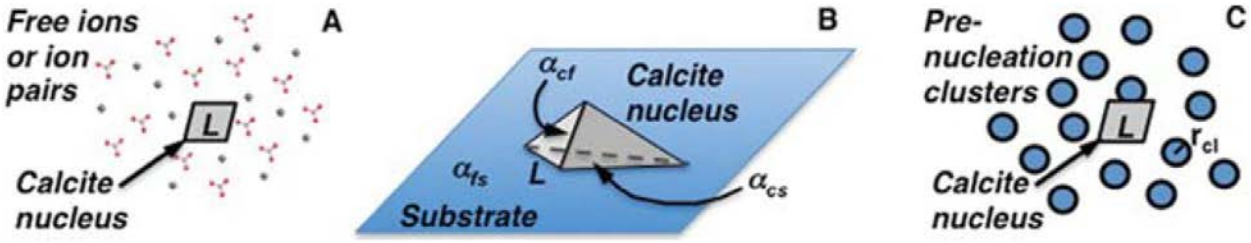

Figure 2.1 Schematic showing three different nucleation scenarios considered here. (A) Homogeneous nucleation of a calcite rhomb of edge length L from ions in solution. (B) Heterogeneous nucleation of a calcite rhomb of edge length L on an arbitrary face and against a substrate. The interfacial free energies for the crystal–fluid, crystal–substrate and fluid–substrate interfaces are α_{cf}, α_{cs}, and α_{fs}, respectively. (C) Nucleation of a calcite rhomb of edge length L from clusters of radius r_{cl} with excess free energy Δg_{ex}.

When the free energy landscape is flat – that is, the excess free energy is simply determined by the surface area times the interfacial free energy α, which is independent of size – then Δg_c is given by:

$$\Delta g_c = B\frac{\alpha^3}{\sigma^2} \tag{2.2}$$

where B is a constant that depends on the shape and density of the nucleating solid (see Appendix I for details). Based on the literature value of 109 mJ m^{-2} for the interfacial free energy of calcite in solution [19, 20], the predicted classical barrier to homogeneous nucleation of a calcite rhomb is formidable (Figure 2.2A and Figure 2.2E, blue curve), ranging from 175 $\mathbf{k}T$ to 93 $\mathbf{k}T$ for $CaCl_2$ and $NaHCO_3$ concentrations between 10 mM and 29 mM—the latter marking the literature value for the solubility limit of ACC [21].

Equation (2.2) also reveals the extreme level of supersaturation needed to reduce the free energy barrier for nucleation of ACC below that for calcite. Based on the scaling of interfacial free energy with solubility [18, 19] the ratio of α for ACC to that of calcite is of order 0.75. Taking into account the differences in the parameter B for calcite and ACC, we find that the free energy barrier to forming calcite will be less than the barrier to forming ACC until the solution concentration is increased to the point where the supersaturation relative to ACC exceeds ~65% of the supersaturation relative to calcite. Because the solubility of ACC is so much higher than that of calcite, for equal mixtures of $CaCl_2$ and $NaHCO_3$, this condition can only be reached if the solution Ca^{2+} concentration is far in excess of 100 mM. Even if the solubility of ACC is considerably smaller than reported in the literature, as seems likely based on recent titration studies [8] as well as from the data reported below – bulk ACC formation was induced at less than half the literature value of the solubility (i.e., 13 mM vs. 28 mM final Ca^{2+} concentration) – the required concentration for ACC to be favored thermodynamically is still extreme. For example, even if the equilibrium solubility is taken to be as small as 10 mM (final Ca^{2+} concentration), a Ca^{2+} concentration of approximately 100 mM is required before there is a crossover in barriers. Even at that concentration, the classical barrier is still in excess of 53 $\mathbf{k}T$. The clear conclusion of this analysis is that, for a flat energy landscape, the concentrations

required to achieve homogeneous nucleation of either phase are extreme and inconsistent with experimental observations of both calcite and ACC nucleation at significantly lower concentrations. Hence, either nucleation is heterogeneous or other pathways of precipitation that avoid this barrier must be at work.

2.2.2 Heterogeneous Nucleation

As Equation (2.1) shows, the thermodynamic barrier depends upon the cube of the interfacial energy. Consequently, heterogeneous nucleation on surfaces (Figure 2.1B) that reduce the interfacial energy can proceed at dramatically altered rates. In this case, α becomes an effective interfacial energy α_{het} that depends on the interfacial energies of the crystal-fluid, fluid-substrate, and crystal-substrate interfaces through:

$$\alpha_{het} = \alpha_{cf} - h(\alpha_{fs} - \alpha_{cs}) \tag{2.3}$$

where h is a factor that depends on the aspect ratio of the nucleus (see Appendix I for details). As long as $\alpha_{cs} < \alpha_{fs}$, the value of α_{het} will be reduced from that for the homogeneous nucleus. However, even if the effective α_{fs} equals α_{cs}, that is, the interfacial energies for the crystal-substrate and fluid-substrate interfaces are equal, the barrier will already be reduced by a factor of 1.6 (Figure 2.2E, red curve) simply because a surface that would have been generated during homogeneous nucleation is now a crystal–substrate interface that carries no energy penalty. A further reduction in α by only 20 to 50% due to $\alpha_{cs} < \alpha_{fs}$ would lead to a decrease in the barrier by a factor of 3 to 13 (Figure 2E, green and orange curves). Given that nucleation rate depends exponentially on this barrier, these large reductions mean that surfaces have the potential to completely alter the dynamics and pathways of calcite formation.

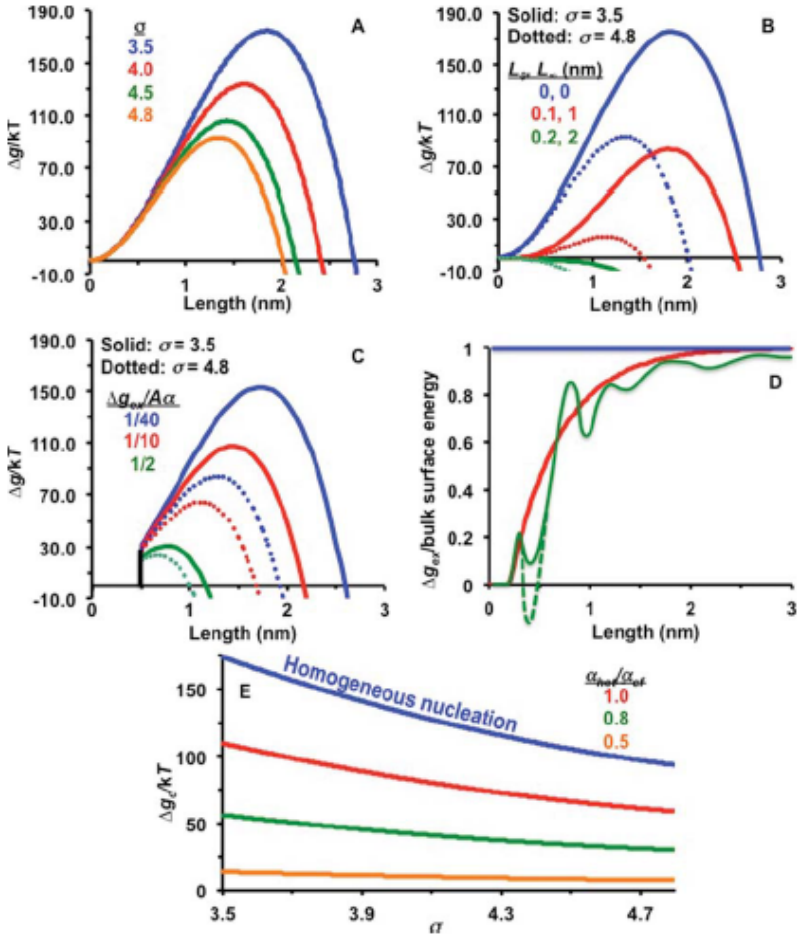

Figure 2.2 (A) Dependence of free energy Δg on the length L of one side of an equilateral calcite rhombohedron for homogeneous nucleation from solutions formed from equal mixtures of $CaCl_2$ and $NaHCO_3$ for the indicated values of supersaturation. The corresponding final Ca^{2+} concentrations are: Blue – 10 mM; Red – 15 mM; Green – 23 mM; Orange – 28 mM. (B) Effect of size dependent excess free energy on Δg_c, where $\alpha = \alpha_\infty\{1 - exp[-(L - L_0)/L_\infty]\}$ and α_∞ is the bulk interfacial energy, for two different supersaturations and the indicated values for L_0 and L_∞, where L_0 is the length at which Δg_{ex} reaches zero in Figure 1D and L_∞ is the size at which it reaches $1 - exp[-(L - L_0)/L_\infty]$ of its bulk value. (C) Effect on Δg of aggregation by clusters of size $L = 0.5$ nm occupying a local minimum in excess free energy for two different supersaturations and the indicated values for the ratio of excess free energy to bulk surface energy. Note that values of Δg make no sense below $L = 0.5$ nm, because clusters of this size are assembled to make the critical nucleus. (D) Dependence of excess free energy (Δg_{ex}) on particle size. Blue line – flat energy landscape; Red line – simple size dependence; Green line – Size dependence with local minima and maxima; Green dashed line – global minimum defining stable population of clusters with narrow size distribution. (E) Dependence of free energy barrier Δg_c on σ for homogeneous nucleation of a calcite rhomb with $\alpha = 109$ mJ m^{-2} (blue line) and heterogeneous nucleation of a calcite rhomb on an (012) face with the indicated values of α_{het}/α_{cf}.

2.2.3 Deviations from a Flat Energy Landscape: Cluster Aggregation and Size Dependent α

In truth, the free energy landscape is unlikely to be flat (blue curve in Figure 2.2D) at small sizes. Δg_{ex} must approach zero at the size of a molecule (shown schematically in Figure 2.2D by red curve) and probably exhibits local minima and maxima at very small cluster size as certain configurations expose more or less favorable coordination geometries for the surface ions (shown schematically in Figure 2.2D by green curves). While these variations in Δg_{ex} are easy to account for by expressing α as a function of size, they do little to change the basic physics of the nucleation process. Nonetheless, they can potentially have significant effects on the magnitude of the barrier (Figure 2.2B and 2.2C) if the size at which that barrier is reached—i.e. the critical size—becomes comparable to the dimensions at which size effects begin to emerge (red curve in Figure 2.2D), or where local (or global) minima (solid (or dashed) green curves in Figure 2.2D) in the free energy landscape create a population of metastable (or stable) clusters that can aggregate to form a critical nucleus (Figure 2.1C). An analysis of how these features impact Equations (2.1) and (2.2) can be found in Appendix I.

Unfortunately, not much is known about the size dependence of the interfacial free energy α. What little data do exist suggest a slight rise with decreasing size, followed by the beginning of a decrease in magnitude [22] but those data do little to constrain the dependence in the region below 5 nm diameter, which is greater than the 1–3 nm critical size seen in Figure 2.2A. Theoretical treatments suggest that even a single formula unit already possesses much of the energetic features of the bulk [23]. This suggests the fall-off in interfacial energy may not occur until diameters below 1 nm, though these simulations were performed for molecular solids and cannot be directly translated to ionic crystals like calcite. However, metadynamics simulations of equilibrium calcite structure suggest the energetic features of the bulk are still manifest below 2 nm [24]. Indirect evidence for a complex dependence on size comes from both cryoTEM [11] and ultra-centrifugation data [8] that suggest there is indeed a population of sub-critical clusters (commonly referred to as pre-nucleation clusters) with a tight size distribution, which implies there is indeed a minimum in the free energy vs. size, as shown schematically in Figure 2.2D (green curves). In fact, titration-based studies on the amount of calcium inferred to be bound in these clusters concluded that they occupy a global minimum, i.e., the free energy of the pre-nucleation clusters lies below that of the free ions [8].

Deviations from a flat landscape will change the dependence of Δg_c on σ from that of Equation (2.2). In the case of a size dependent α, the change can be complex and depends on the form of the size dependence. For nucleation by aggregation of clusters that occupy a local minimum in the free energy, the dependence becomes:

$$\Delta g_c = B\frac{\alpha^3}{(\sigma \pm C)^2} \tag{2.4}$$

where C is a constant that depends on the shape factor, the cluster radius and the excess free energy of the cluster, and the plus or minus sign depends on whether the minimum in Δg is local

or global (see Appendix I for details). If it is a local minimum (Figure 2.2D, solid green line), then the clusters are metastable, they carry excess free energy above the free ions, the plus sign applies and the barrier is reduced. If it is a global minimum (Figure 2.2D, dashed green line), then the clusters lie below the free ions, the minus sign applies and nucleation by cluster aggregation brings with it an extra energy cost (see Appendix I for details). This is the case for pre-nucleation clusters, which were found to lie about 18 kJ mol^{-1} below the free ions [25]. Thus creation of a super-critical nucleus by aggregation of pre-nucleation clusters would bring with it a larger barrier than aggregation of free ions, regardless of whether the end product is an amorphous or crystalline phase.

One interesting implication of Equation (2.4) is that the impact of clusters—stable or metastable—is to effectively alter the supersaturation from σ to $\sigma \pm C$, making it larger for metastable clusters and smaller for stable clusters. The result is that the existence of metastable clusters increases the probability of nucleating ACC rather than calcite, while the existence of stable clusters decreases that probability.

In the case of calcite nucleation by metastable clusters, for cluster radii below 2 nm and a reasonable range of excess free energies—such as those used in Figure 2.2C, the magnitude of C in Equation (2.4) is less than 10% of σ over the range used in this study. The small magnitude of C relative to σ has two consequences for the current study. First, measurements of the dependence of calcite nucleation rate on supersaturation will not distinguish between ion-by-ion and cluster-by-cluster addition; either way the data will appear to follow the dependence of rate on supersaturation predicted by the classical expressions. Second, because the effect of clusters is likely to be too small to detect, if the classical dependence is not observed, then size dependence of α is the likely source of the deviation.

2.3 Experimental Methods

2.3.1 SAM Preparation:

Gold substrates were prepared by evaporating 5 nm Ti and 50 – 100 nm Au on Si <100> wafers and cleaving the wafers into pieces approximately 1 cm^2 in size. The MHA and MUA monolayers on gold surfaces were prepared by immersing gold substrates for 24 to 30 hours into 2 mM MHA or MUA solutions of 95% ethanol and 5% acetic acid [12]. After removal from the ethanolic solutions, the gold substrates were thoroughly rinsed with the corresponding pure solvent, 5% acetic acid in ethanol, and then dried by flow of nitrogen gas. SAMs were covered by DI water to eliminate potential oxidization and then instantly placed in the flow cell of the optical microscope.

2.3.2 Solution preparation:

Ca^{2+} and CO_3^{2-} solutions were prepared from DI water and reagent grade $CaCl_2$ and $NaHCO_3$ for concentrations of: 10 mM, 18 mM, 20 mM, 21 mM, 22.5 mM, 24 mM, 25 mM, 26 mM, 27 mM, 28 mM, 29 mM, and 30 mM. Outside of this concentration range, nucleation rates

were found to be either too fast or too slow to be successfully analyzed. The activities of Ca^{2+} and CO_3^{2-}, and supersaturation relative to calcite and ACC, were calculated using the Visual MINTEQ (Jon Petter Gustafsson) software [26] (Table 2.1). The equilibrium solubility products (K_{sp}) of calcite and ACC used in the calculations were $10^{-8.48}$ and $10^{-6.393}$ [21], respectively.

Table 2.1 Calculated supersaturations of calcite and ACC for experimental conditions.

	{Ca^{2+}}	{CO_3^{2-}}	σ (calcite)	σ (ACC)
10 mM	4.45E-03	2.48E-05	3.506	-1.299
15 mM	5.84E-03	3.14E-05	4.014	-0.791
20 mM	7.04E-03	3.71E-05	4.368	-0.437
21 mM	7.26E-03	3.81E-05	4.425	-0.379
22 mM	7.48E-03	3.92E-05	4.483	-0.322
23 mM	7.69E-03	4.02E-05	4.536	-0.269
24 mM	7.90E-03	4.11E-05	4.58	-0.218
25 mM	8.11E-03	4.21E-05	4.635	-0.170
26 mM	8.31E-03	4.30E-05	4.683	-0.122
27 mM	8.51E-03	4.40E-05	4.727	-0.078
28mM	8.71E-03	4.49E-05	4.770	-0.034
29 mM	8.90E-03	4.58E-05	4.812	0.0069
30 mM	9.10E-03	4.67E-05	4.853	0.0483

2.3.3 Optical microscopy:

A schematic image of the optical setup is illustrated in Figure 2.3. $CaCl_2$ and $NaHCO_3$ solutions were loaded into separate syringes of an automated syringe pump. $CaCl_2$ was first injected into the fluid cell before flowing through an equal mixture of $CaCl_2$ and $NaHCO_3$ solutions of equal concentrations in order to achieve better face-selective control [27]. Flow rates from 0.5 to 5 mL min^{-1} were tested. It was found that the $CaCO_3$ nucleation rate increased as the flow rate increased from 0.5 to 2 mL min^{-1}, but did not change if the rate was increased further. Therefore, the flow rate was set to 2 mL min^{-1}, to yield nucleation rates independent of flow rate. This ensured that the nucleation was not limited by diffusion but was controlled by the nucleation reaction at the SAM surface. The tubing length was adjusted to ensure adequate mixing with little or no nucleation occurring prior to entering the fluid cell. A tubing length of around 38 cm provided the highest rate of nucleation on the SAMs.

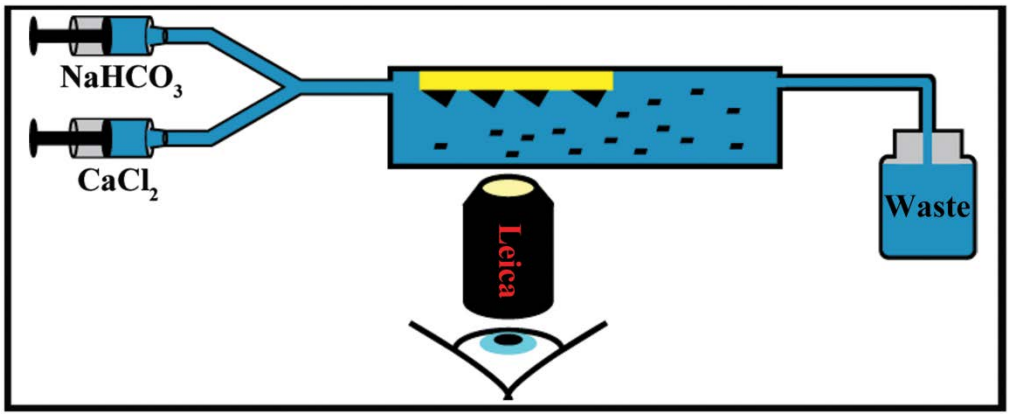

Figure 2.3 Schematic of experimental set-up for measuring nucleation rates. The SAM is suspended upside-down in a flow-through cell and imaged using an inverted optical microscope to measure nucleation rates as supersaturated calcium carbonate solutions are continuously pumped through the cell to maintain constant supersaturation.

The SAMs were placed upside down in the flow cell to prevent spurious nuclei from the solution from landing on the SAMs. $CaCO_3$ nucleation on the SAMs was imaged in situ using an inverted optical microscope in an area of 0.65×0.49 mm^2. Because the critical radius of a $CaCO_3$ nucleus was expected to be well below the resolution limit of the optical system, the nuclei were too small to be observed by the optical microscope at the instant of formation, so it was assumed that each observed crystal developed from one nucleus. This assumption was reasonable because the observed nucleation density was so low that the average distance between neighboring nuclei was much greater than the size at which the nuclei became visible. The observed linear dependence between number of nuclei and time after the onset of nucleation validates this assumption.

2.3.4 Raman analysis:

Samples were quenched in the optical cell by changing the flow from calcium carbonate solution to ethanol, as described previously for quenching of calcium phosphate samples [5]. Precipitates collected right after quenching exhibited Raman patterns characteristic of calcite with peaks at 154 cm^{-1}, 284 cm^{-1}, 710 cm^{-1}, and 1084 cm^{-1} [28, 29]. However, the distinctive broad peak of ACC at 150-300 cm^{-1} [30, 31] did not occur in any of the patterns. Since the volumes of the smallest particles are at the lower detection limit of micro-Raman, the peaks are not as sharp as the ones from the other two morphologies (The 520 cm^{-1} peak is that of Si from the silicon wafer).

2.3.5 Atomic Force Microscopy:

In situ atomic force microscopy was measured by using an AFM liquid cell with either contact or tapping mode AFM (Digital Instruments J scanner, Nanoscope IIIa and V controllers, Veeco Metrology, Inc.) using hybrid probes consisting of silicon tips on silicon nitride

cantilevers (Bruker AFM – Sharp Nitride Lever, k = 0.35 N m^{-1}, tip radius < 10 nm; AppNano – Hydra, k = 0.035 N m^{-1}, tip radius < 10 nm). The tapping mode was adopted in these experiments while applying a loading force less than 50 pN using optimized feedback and set-point parameters for stable imaging conditions. About 100 μL of growth solutions were injected into the sealed liquid cell and the image was captured immediately after the solution injection. Measurements were made by mixing equal $CaCl_2$ and $NaHCO_3$ with the final concentrations of 13 mM and 25 mM on the surface of hydroxyl-terminated SAMs and between 20 mM and 40 mM on the surface of carboxyl-terminated SAMs. SAM preparation followed the same procedure as used in the optical experiments, using MUO and MHA for hydroxyl-and carboxyl-SAMs, respectively. In order to increase the image stability and nuclei density, in situ AFM experiments were also carried out by diffusion method with ammonium carbonate diffusing into 50 mM $CaCl_2$ on the surface of OH terminated SAMs or mica. No obvious differences were observed between these two methods or substrates. The first particle was observed within 1 min for mixing method and up to 30 min for diffusion method, however, all of these particles were dissolved within 5 min when the rhombohedral crystal formed separately.

2.3.6 TEM analysis:

TEM samples used the same solution preparation method described for the AFM analysis. Subsequent to filtering the solutions, equal amounts were pipetted into a 1 mL centrifuge tube and spun at 6000 rpm in a Galaxy Ministar centrifuge (VWR) for 1-2 minutes, depending on concentration. The supernatant liquid was quickly removed and replaced with pure ethanol and the sample was centrifuged for another minute. This was repeated three times. After the final rinse, ethanol was used to wash any solid off the centrifuge tube walls and suspend the material in solution. A drop of this solution was placed on a TEM grid which was immediately placed into vacuum and pumped into the millitorr range. The TEM grid was then removed from vacuum, secured onto a TEM stage, and inserted into a JEOL 2100F operating at 200kV for analysis.

2.3.7 Carbonate diffusion optical experiments:

Carbonate diffusion experiments were conducted by placing OH and COOH SAM substrates in a covered 100 mm diameter petri dish, elevating the substrate to just below the inner surface of the lid. A small droplet of a few to a few tens of microliters of $CaCl_2$ solution, 10-50 mM, was placed on the substrate, and a 20 mm diameter dish containing less than a gram of $(NH_4)_2CO_3$ was placed nearby the substrate in the larger dish. The lid was then replaced on the larger dish and the dish was moved such that the substrate was in the focal plane of a light microscope and the first image was collected, establishing a zero time point. This time point was five to ten seconds after closing the dish. Sequential images were captured every five to ten seconds following the zero time point.

2.4 Results

2.4.1 Calcite Nucleation Rates on Carboxyl-Terminated SAMs

SAMs of 16-mercaptohexadecanoic acid (MHA) and 11-mercaptoundecanoic acid (MUA), both of which are carboxyl-terminated but differ in the length and parity of the carbon chain, were prepared on Au (111) substrates using previously described methods [12]. The SAMs were suspended upside down in a custom-built flow cell in the focal plane of an inverted optical microscope. A mixture of $CaCl_2$ and $NaHCO_3$ solutions with equal final concentrations of between 20 and 35 mM were flowed through the cell at constant rates under conditions that ensured nucleation was controlled by the reaction kinetics at the SAM surface rather than by diffusion or mixing. For each concentration, the number of crystals in a fixed area was determined as a function of time (Figure 2.4A–D). Plots of the number of nuclei vs. time (Figure 2.4E) produced S-shaped curves exhibiting a linear rise and an approach to saturation marking the time when the density of nuclei became too great for subsequent events to be independent. The slope of the linear region gave the steady-state nucleation rate J_n (number of nuclei per unit area per unit time).

The range of times selected for the linear fit was chosen based on visual inspection of the plotted data, with the resulting linear fits having high r-squared values. While crude, this approach was not expected to introduce a significant error into the final determination of values for α due to a number of factors. Minor adjustments to the time range selection for determining J_n would not induce significant changes to the value of J_n. For the purpose of determining α the important value is $\ln(J_n)$, so small errors in J_n should be inconsequential. Furthermore, α is related to the cube root of the slope in $\ln(J_n)$ vs σ^{-2}, further reducing the effect of any initial error on the final determination of α. Lastly, it is expected that any potential error in time range selection from the procedure utilized would be systematic, and mitigate any small impact on the analysis. Any error thus introduced into the J_n data would offset each data point on the vertical axis in the same direction, with the net result being an error in the y-intercept (which is not important for the determination of α) rather than the slope.

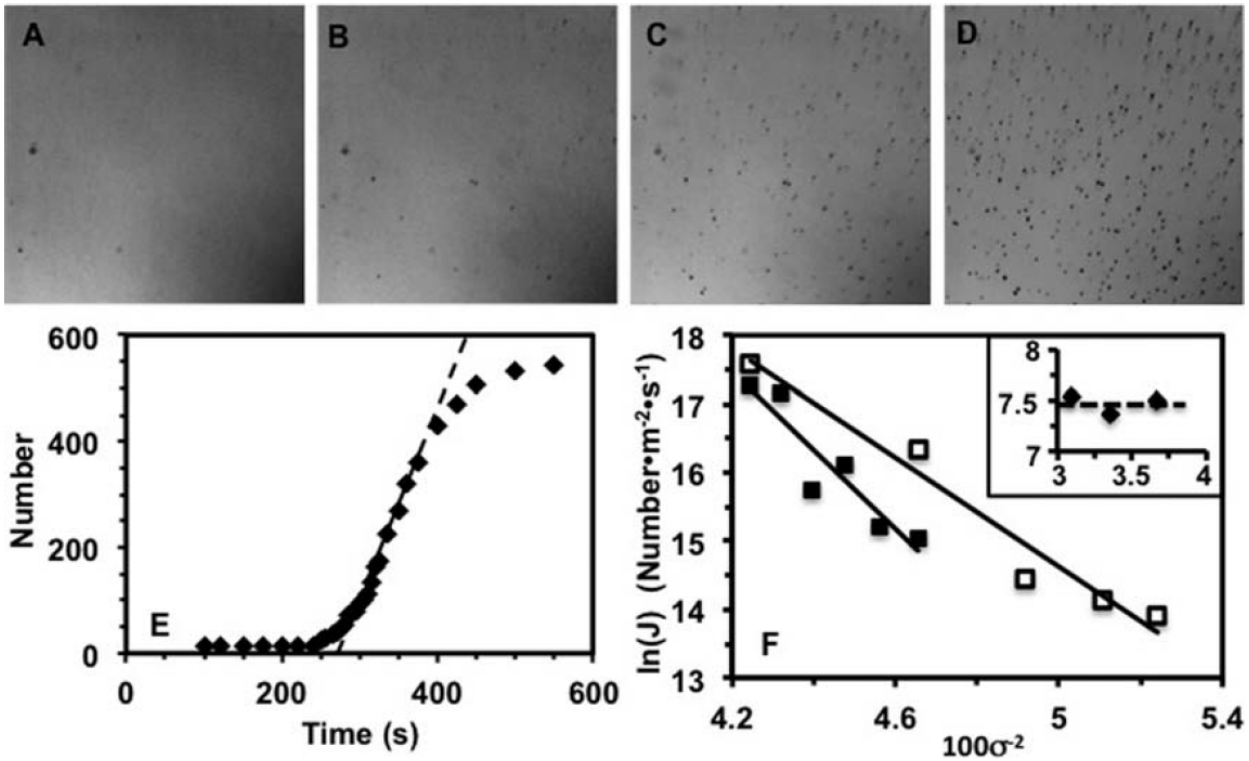

Figure 2.4 Rate of calcite nucleation on MHA and MUA SAMs. (A–D) Sequential optical images collected at t = 100, 300, 350 and 450 s. Each image is 0.49 × 0.49 mm in area. (Raw data were collected over 0.65 mm × 0.49 mm area.) (E) Typical dependence of number of nuclei on time. (F) Dependence of $\ln(J_n)$ on σ^{-2} showing that MHA films produce shallower slope and lower intercept than MUA films. Inset – Same as in F, but for nucleation on the OH-terminated mercapto-undecanol (MUO) SAM in solutions produced by mixing solutions of $CaCl_2$ and Na_2CO_3 at a pH of 10.55.

While qualitatively similar behavior was observed for both the MHA (C-16) and MUA (C-11) films, the nucleation rate was found to be greater on MHA over the entire supersaturation range explored here. In addition, in accord with previous reports, nucleation occurred on distinct crystallographic planes for the two different SAMs [15]. The even parity MHA SAM induced nucleation almost exclusively on the (012) plane (Figure 2.5A), while on the odd parity MUA SAM nucleation occurred primarily on the (013) face (Figure 2.5B), though 30–40% of the crystals exhibited orientations between (012) and (015), and also included sporadic (104) and (001) orientations (Figure 4B insets). In contrast, under identical conditions, nuclei on SAM-free gold films were few in number and exhibited random orientations (Figure 2.5C).

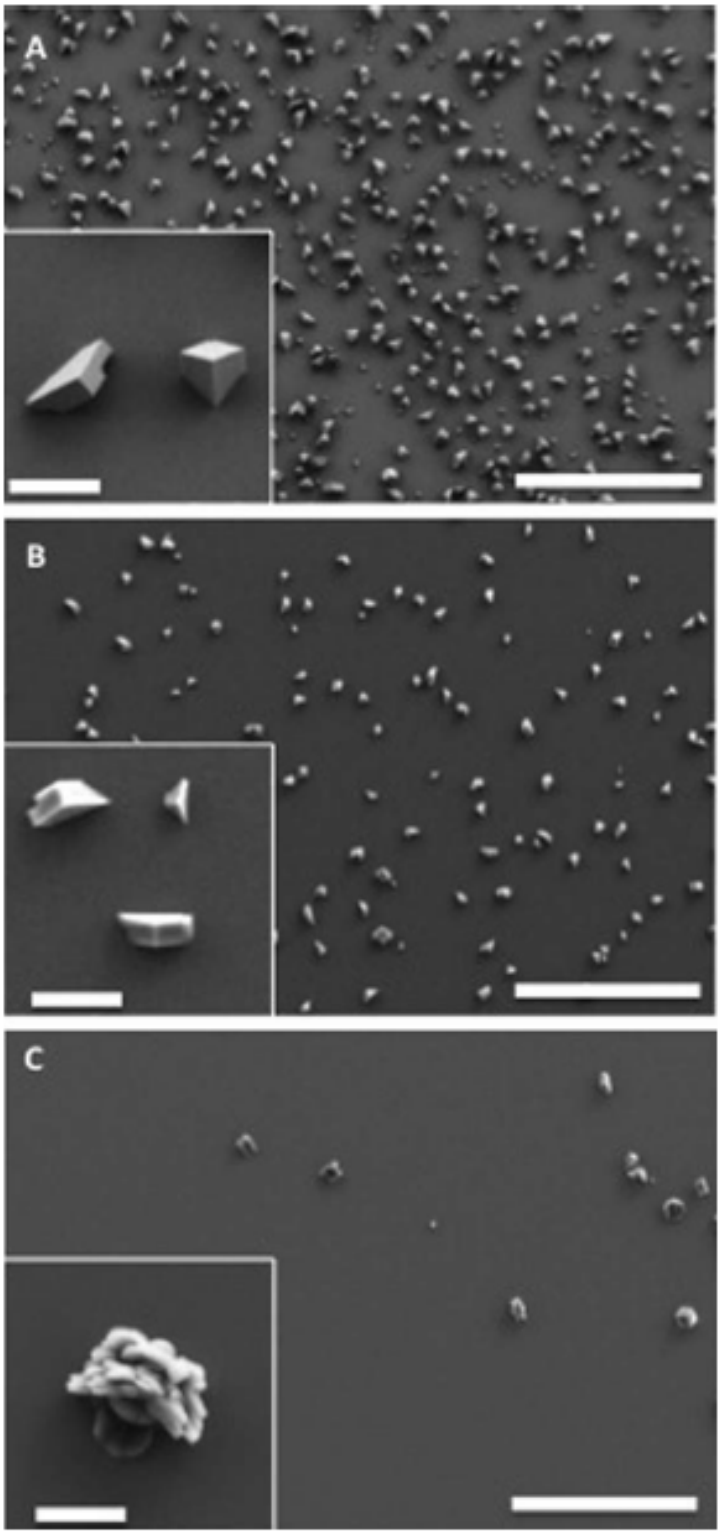

Figure 2.5 SEM images showing number density and orientation of calcite crystals on (A) MHA, (B) MUA, and (C) bare gold surfaces. Scale bars are: main images – 100 mm; insets – 10 mm.

Analysis of nucleation data such as those given in Figure 2.4E shows that J_n exhibits the dependence on σ expected from CNT through Equations (2.1) and (2.2) (Figure 2.4F). From the slope of $\ln(J_n)$ vs. σ^2 were obtained values for α of 72 mJ m^{-2} for MHA and 81 mJ m^{-2} for MUA, both of which are substantially smaller than the value of 109 mJ m^{-2} for calcite in bulk solution [19, 20]. These differences in interfacial energy have a dramatic impact on nucleation rates. For example, in the middle of the supersaturation range explored here, the corresponding free energy barriers for nucleation on MHA, MUA and in bulk solution are found to be 19 $\mathbf{k}T$, 27 $\mathbf{k}T$ and 105 $\mathbf{k}T$, respectively. All other factors being equal, these differences alone would correspond to relative nucleation rates $J_n^{MHA} : J_n^{MUA} : J_n^{sol}$ of $1 : 3.4 \times 10^{-4} : 4.5 \times 10^{-38}$, although the advantage of the MHA film over that of the MUA film is somewhat reduced because it also produces a larger value of E_A by about 7 ± 3 $\mathbf{k}T$ (as can be seen from the smaller value of the y-intercept for MHA when extrapolated to $\sigma^2 = 0$). These results show that calcite nucleation on these canonical SAMs proceeds as expected from CNT and that both the enhancement of nucleation on the SAMs relative to bulk solution and the advantage of the SAM with even parity over that with odd parity can be explained in purely classical terms through differences in interfacial energy.

2.4.2 Nucleation Pathways

These findings support the conclusion that the classical viewpoint of nucleation control through minimization of crystal-SAM interfacial energy can describe nucleation in this system and appear to be in conflict with the proposed model for calcite formation as a non-classical process [8, 11, 12, 25, 32]. In particular, they raise the question of how these results can be reconciled with those of previous studies that concluded: 1) nucleation of calcite occurs via an ACC precursor and 2) $CaCO_3$ solutions contain pre-nucleation clusters that aggregate to form this precursor. To address these apparent discrepancies the pathway of calcite formation on SAMs were investigated using Raman spectroscopy, in situ AFM imaging, optical microscopy and TEM analysis.

Raman spectra collected on samples that were quenched during the nucleation rate experiments by switching the incoming fluid from $CaCO_3$ solution to ethanol corresponded to that of calcite regardless of particle size investigated (Figure 2.6). It is certain that the ethanol itself did not cause conversion of ACC to calcite, because ACC is routinely preserved via this technique using OH films in both the optical and AFM fluid cells, as well as centrifuges and button filters. However, sub-100 nm particles present on the MHA films as seen in some SEM images (data not shown) were below the threshold for obtaining useful Raman spectra. To assess these particles, the conditions of the optical experiments were reproduced using an AFM in place of the optical microscope. When these experiments were performed using MHA SAMs as substrates, all particles that appeared remained intact and grew in size. Even at the earliest stage of formation captured by the AFM, these particles possessed the typical rhombic shape of calcite and exhibited the orientation seen at larger size that results from nucleation on an (012) face (Figure 2.7A–D).

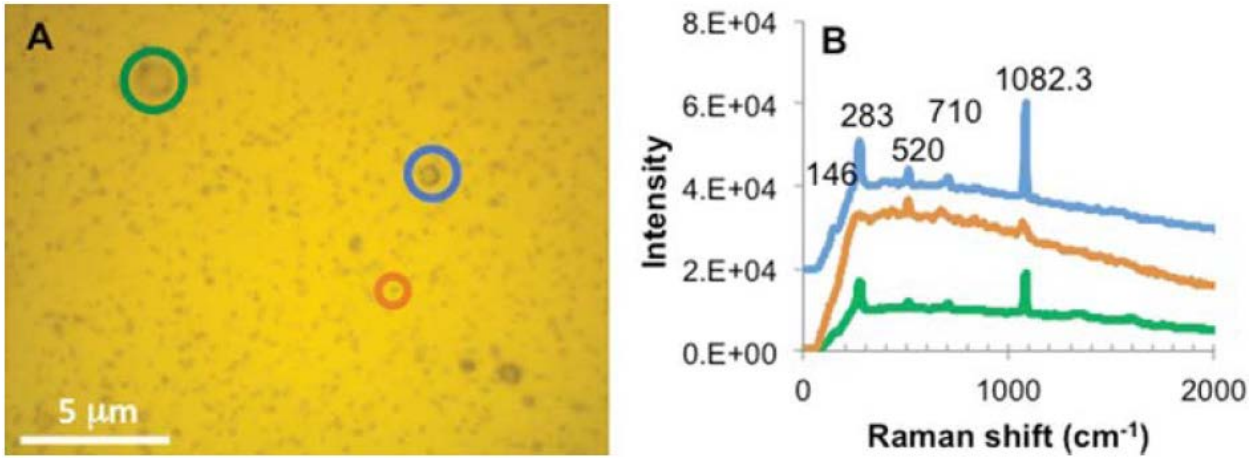

Figure 2.6 Typical Raman spectra of particles formed right after the incubation time for 30 mM solutions. (A) optical microscopy image of of $CaCO_3$ particles collected on gold 75 s after mixing the solutions, (B) Raman spectra where color of curve corresponds to that of solid circle in (A).

When the same experiments were performed using an OH terminated SAM (mercapto-undecanol, MUO), at all supersaturations investigated—including concentrations that were highly undersaturated with respect to ACC based on the accepted bulk solubility—within the first minute of imaging the formation of roughly spherical nanoparticles characteristic of ACC were observed, whose number and size were dependent on the solution concentration (Figure 2.7E). (Raman spectra and SEM data from MUO samples (not shown) readily confirm the presence of ACC.) Unlike the result with MHA SAMs, these particles did not continue to grow in size. Instead, after a short period of time they began to dissolve (Figure 2.7E–G) in response to the formation of the more stable calcite phase elsewhere in the cell. In parallel experiments using identical solution mixtures, these nanoparticles were collected on filters and examined by high resolution TEM, which revealed them to indeed be amorphous (Figure 2.7H).

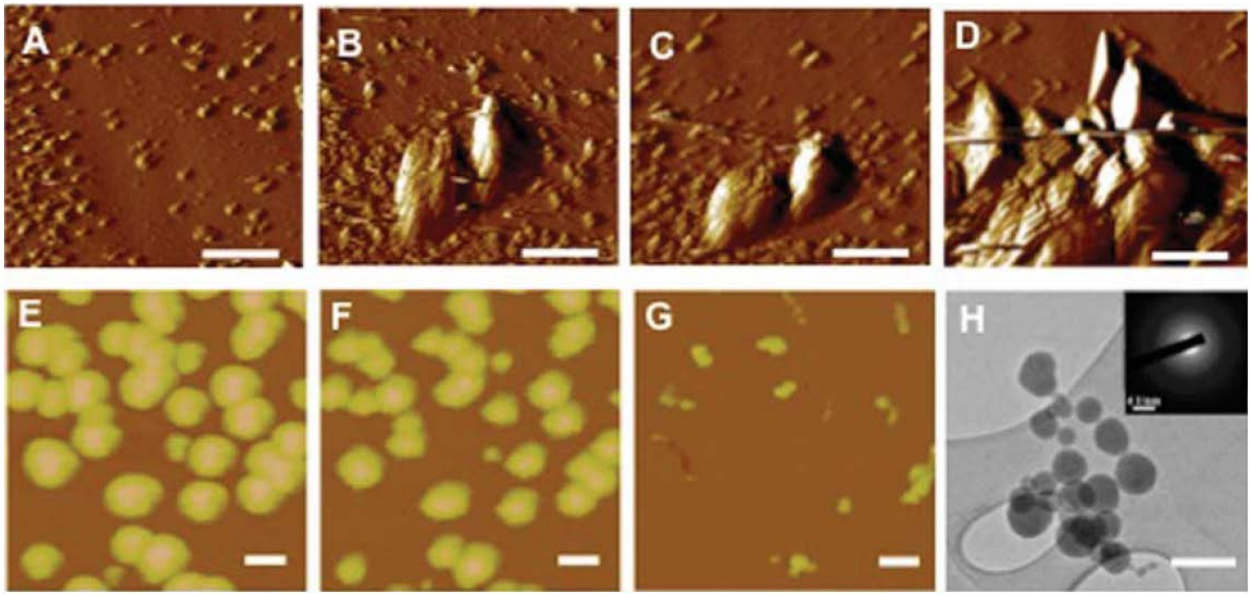

Figure 2.7 (A–D) Series of sequential in situ AFM images showing nucleation on MHA SAM in 25 mM solution with pH 8.4. The features seen in Figure 7A are not $CaCO_3$ precipitates; they are present even in pure water and are likely to be aggregates of the SAM monomers. First particles to appear have typical morphology seen for calcite rhombohedra nucleating on (012) face and grow in number and size with time. Time between frames is 93.2 s and scale bars are 1.0 mm. (D–F) Series of sequential in situ AFM images showing dissolution of initially formed nanoparticles in 13 mM $CaCO_3$ solution at room temperature and pH 8.4 on the surface of MUO. Times at which these frames were captured are (D) 68 s, (E) 128 s and (F) 190 s, where t = 0 corresponds to the moment when the calcium and bicarbonate solutions were mixed. The average height of nanoparticles decreases from (D) 64.2 $\pm$ 9.7 nm to (E) 53.2 $\pm$ 12 nm and to (F) 33.2 $\pm$ 14 nm. Scale bars are 200 nm. (G) TEM image and diffraction pattern (inset) of nanoparticles captured from 25 mM $CaCO_3$ showing particles are amorphous. Scale bar is 100 nm.

Despite in situ AFM observations on many tens of these ACC particles, in no instance was their direct transformation into calcite observed. Rather, only dissolution was observed. However, the AFM only samples small areas ($< 100 \times 100\,\mu m^2$) so a transformation event that occurred out of the field of view may have simply been missed. To circumvent this limitation, the fact that ACC particle size is dependent on supersaturation was utilized. The supersaturation can be driven to high values by introducing carbonation via gaseous diffusion from an ammonium carbonate source, in order to generate a film of ACC particles with diameters of 100s of nm (Figure 2.8). As expected, when the OH–terminated MUO on Au was used the formation of ACC, most of which fell on the SAM from the solution, was observed. However, this film of ACC particles rapidly dissolved back into solution as calcite rhombs nucleated and grew at their expense (Figure 2.9A–C).

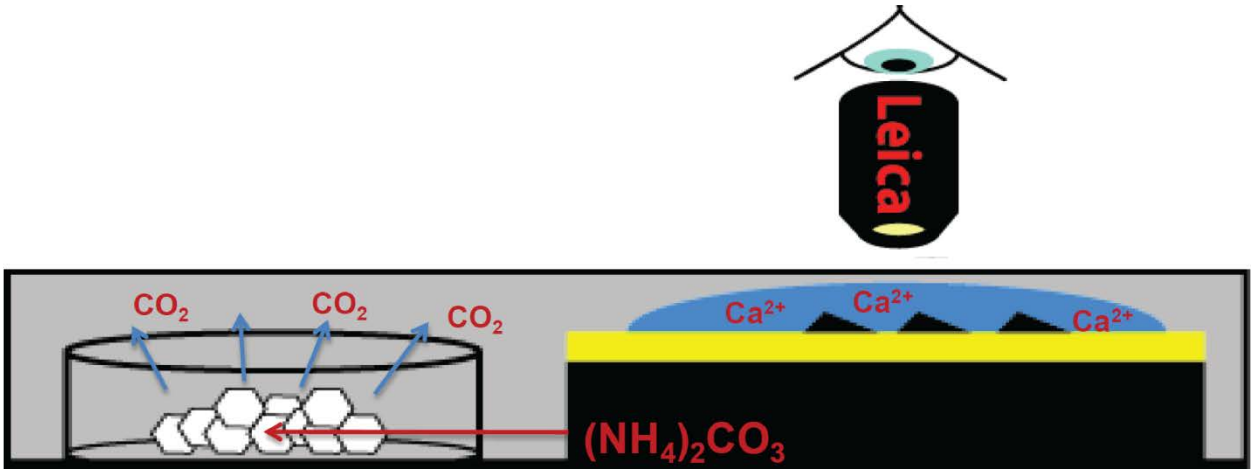

Figure 2.8 Schematic showing set-up for optical experiments to observe calcium carbonate nucleation during diffusion of carbonate into a $CaCl_2$ solution. The upward-facing SAM is covered with a droplet of $CaCl_2$ solution in a closed optically transparent container. $(NH_4)_2CO_3$ is placed in an open dish near the droplet and nucleation is observed through an optical microscope.

As a note, in no instance could it be definitively concluded that a calcite rhomb formed through direct transformation of a pre-existing ACC particle. In a number of cases, the rhomb formed from a distinct particle that deposited on the MUO surface and immediately began to grow. The fact that ACC formation occurred before any calcite surface nucleation events took place explains why rates of calcite nucleation on these films showed no dependence on the initial solution supersaturation (Inset, Figure 2.4F). Once ACC formed homogenously, the solute concentration immediately became fixed at the solubility of ACC. Thus, in essence, all calcite nucleation occurred at the same supersaturation, regardless of the initial solution conditions.

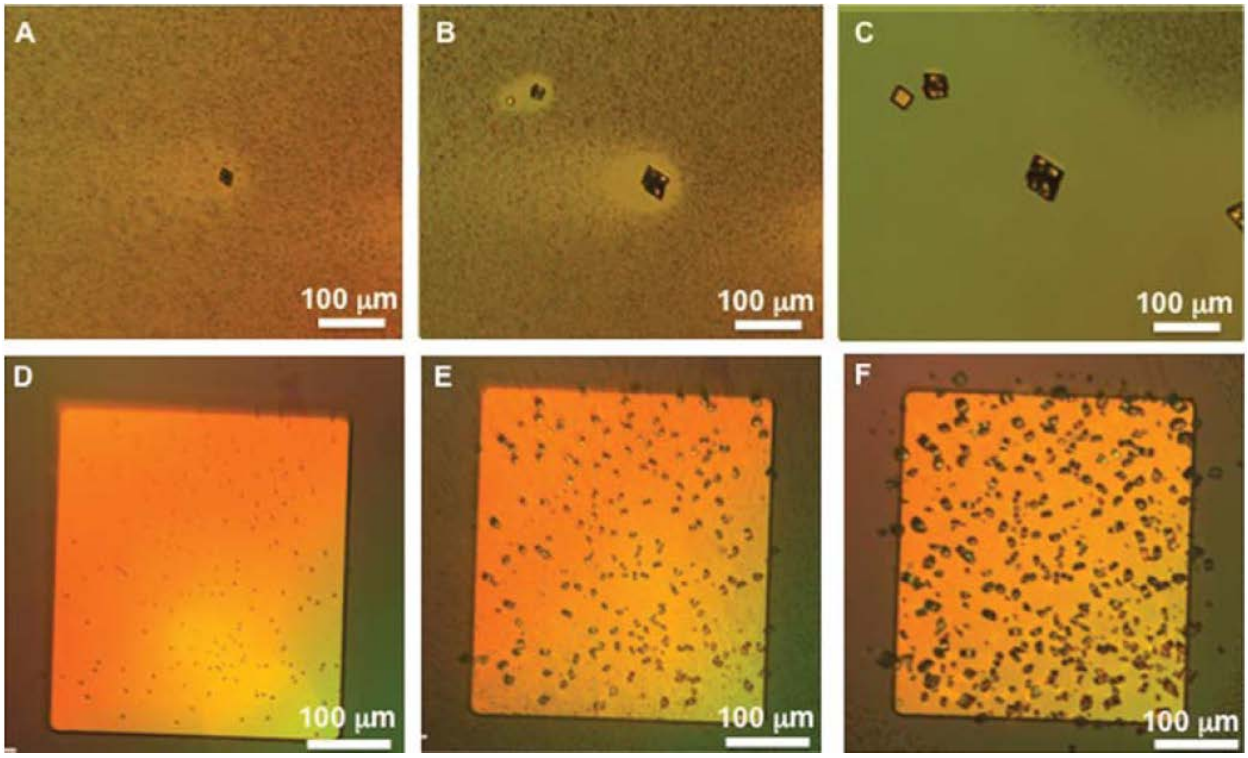

Figure 2.9 (A–C) Image sequence shows the pathway of calcite formation during diffusion of carbonate into $CaCl_2$ solution on an MUO SAM. The appearance of ACC is followed by nucleation of calcite and concomitant dissolution of the ACC film. Frame times are 830 s, 1,892 s and 3,742 s. (D–F) Image sequence shows the pathway of calcite formation during diffusion of carbonate into $CaCl_2$ solution on an MHA SAM. Calcite first appears only on the MHA film. As it grows, ACC then begins to deposit from solution until the Ca^{2+} is sufficiently depleted that ACC dissolves as calcite continues to grow. Frame times are 280 s, 700 s and 1500 s.

When the carbonate diffusion experiments were performed using the MHA SAMs, the progression of events was completely reversed from that seen on MUO (Figure 2.9D–F). The first particles to appear formed directly on the SAM surface and grew into calcite rhombs. None of these particles ever underwent dissolution. Well after they could be clearly identified as rhombs, ACC began to form in solution and deposit on the surrounding Si substrate. Some of this ACC also deposited on the SAM, but dissolved immediately due to presence of the growing calcite crystals. As the Ca^{2+} level in the surrounding solution decreased, even the ACC outside of the SAM began to dissolve due to the continued growth of the calcite rhombs. When SAMs were used that extended across the entire substrate, no ACC was observed, because the formation of calcite across the full extent of the film prevented the supersaturation from reaching the required level for ACC formation. Figure 2.10 shows a schematic representation of the pathways inferred from these experiments for both the carboxyl- and hydroxyl-terminated SAMs.

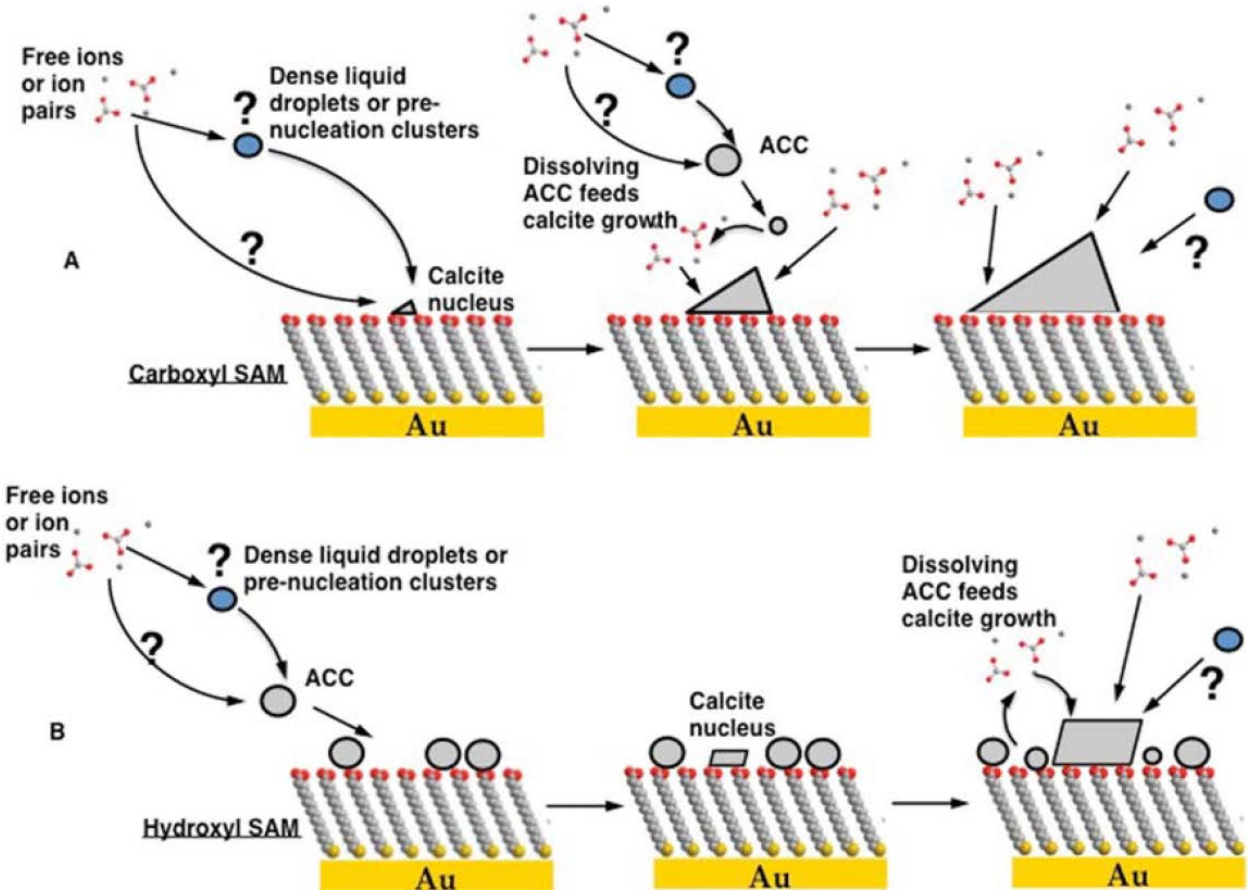

Figure 2.10 Schematic showing pathways of calcite formation on (A) carboxyl- and (B) hydroxyl-terminated SAMs. With carboxyl-terminated SAMs, free ions and ion pairs, pre-nucleation clusters or dense liquid droplets aggregate directly on the SAM to form a critical nucleus of calcite, which then grows by addition of these species. ACC then subsequently forms in solution and dissolves as it falls towards the SAM, thereby feeding the growing crystal. With hydroxyl-terminated SAMs, free ions and ion pairs, pre-nucleation clusters or dense liquid droplets first aggregate to form ACC nanoparticles in the solution. The ACC particles then land on the SAM, forming an ACC film. Subsequent nucleation of calcite either directly on the SAM or in the surrounding solution then leads to dissolution of the ACC film as the calcite grows.

2.5 Discussion

The results presented suggest that ACC nanoparticles did not serve as direct precursors to calcite in the experiments with carboxyl SAMs. Rather calcite formation resulted from distinct nucleation events. While this result would seem to contradict the previous claims that ACC serves as a precursor to calcite, it should be noted that nearly all previous studies in which this two-step pathway was proposed were carried out at supersaturations well in excess of the solubility limit of ACC [8, 11, 12]. Furthermore, with one exception [11] the transformation of an amorphous particle into a crystal was not directly observed, rather it was inferred from the

sequence of events, i.e., ACC formed first and was eventually replaced by one of the crystalline phases. In the case of experiments that utilized carbonate diffusion into a $CaCl_2$ solution [12], as well as those based on titration of a carbonate buffer [8], the supersaturation increased continually to the point of nucleation. Thus the large barrier to homogeneous nucleation, which is still in excess of 90 $\mathbf{k}T$ at the literature value of ACC solubility, may simply have prevented calcite nucleation before conditions that favored ACC formation were reached. Whether the eventual conversion to a crystalline phase occurred by direct transformation from ACC or through dissolution and re-precipitation on crystal nuclei that formed independently is simply not known.

In a series of cryoTEM studies, formation of vaterite from ACC precursor particles was deduced from analysis of ex situ images that revealed vaterite nanoparticles within larger amorphous particles in contact with a Langmuir monolayer [11, 33, 34]. However, the interfacial energy between the Langmuir monolayer and calcium carbonate crystalline phases is unknown, and may simply be too high to allow the transformation from ACC to any crystalline phase on the timescale of the experiments under the tested conditions. One may well find that, at lower supersaturation the situation is reversed and vaterite forms directly, albeit on a longer timescale than observed for ACC at the supersaturation used in the experiments. Finally, even though the calcite crystals in this study appear to nucleate before ACC forms in the case of MHA and perhaps even separately from the initial ACC nanoparticles in the case of MUO, the possibility cannot be ruled out that the calcite nuclei are themselves constructed from clusters below 10 nm in size, whether crystalline or amorphous. Even the earliest nuclei successfully captured by AFM had already grown to ~20 nm along the shortest dimension. As pointed out in Section 2.2.3, for a reasonable range of cluster excess free energies, their effect would be undetectable in measurements of $J_{\mathrm{n}}\ vs.\ \sigma$. Thus their dynamics would only be reflected in the prefactors A and E_A. As long as the super-critical nucleus that emerges is that of calcite, the rate data will reflect the calcite-SAM interface through the classical expressions. Consequently, there is no obvious contradiction between these studies.

With respect to the pre-nucleation clusters [25], there are two possible scenarios that are consistent with all of the observations described in this chapter. First, the clusters are like any other solution species; they behave as simple ionic complexes, constantly forming unstable sub-critical nuclei that spontaneously fluctuate in size until, by chance, they exceed the critical nucleus size either by ion addition or cluster aggregation. Second, they play no role in nucleation at the relatively low concentrations of these experiments; nucleation is ion-by-ion because the number and diffusivity of the free ions are much greater than those of the clusters or because the kinetic barriers to building an ordered nucleus from ions are much less than those to desolvating and ordering the clusters. A firm conclusion will have to wait until experimental tools enable direct characterization of pre-nucleation clusters in low concentration solutions at surfaces.

2.6 References

1 L. Addadi, D. Joester, F. Nudelman, S. Weiner, Mollusk shell formation: A source of new concepts for understanding biomineralization processes. *Chemistry: A European Journal* **12**, 981-987 (2006). doi:10.1002/chem.200500980

2 O. Braissant, G. Cailleau, C. Dupraz, A. P. Verrecchia, Bacterially induced mineralization of calcium carbonate in terrestrial environments: The role of exopolysaccharides and amino acids. *Journal of Sedimentary Research* **73**, 485-490 (2003). doi:10.1306/111302730485

3 S. Weiner, W. Traub, H. D. Wagner, Lamellar bone: Structure-function relations. *Journal of Structural Biology* **126**, 241-255 (1999). doi:10.1006/jsbi.1999.4107

4 F. Nudelman, K. Pieterse, A. George, P. H. H. Bomans, H. Friedrich, L. J. Brylka, P. A. J. Hilbers, G. de With, N. Sommerdijk, The role of collagen in bone apatite formation in the presence of hydroxyapatite nucleation inhibitors. *Nature Materials* **9**, 1004-1009 (2010). doi:10.1038/nmat2875

5 J. J. De Yoreo, P. G. Vekilov, Principles of crystal nucleation and growth. In *Biomineralization*, P. M. Dove, J. J. DeYoreo, S. Weiner Eds. (Mineralogical Soc America, Washington, 2003), *Reviews in Mineralogy & Geochemistry* vol. 54, pp. 57-93. doi:10.2113/0540057

6 I. Jager, P. Fratzl, Mineralized collagen fibrils: A mechanical model with a staggered arrangement of mineral particles. *Biophysical Journal* **79**, 1737-1746 (2000). doi:10.1016/S0006-3495(00)76426-5

7 P. A. Fang, J. F. Conway, H. C. Margolis, J. P. Simmer, E. Beniash, Hierarchical self-assembly of amelogenin and the regulation of biomineralization at the nanoscale. *Proceedings of the National Academy of Sciences of the United States of America* **108**, 14097-14102 (2011). doi:10.1073/pnas.1106228108

8 D. Gebauer, A. Volkel, H. Colfen, Stable prenucleation calcium carbonate clusters. *Science* **322**, 1819-1822 (2008). doi:10.1126/science.1164271

9 Y. Politi, T. Arad, E. Klein, S. Weiner, L. Addadi, Sea urchin spine calcite forms via a transient amorphous calcium carbonate phase. *Science* **306**, 1161-1164 (2004). doi:10.1126/science.1102289

10 J. Mahamid, A. Sharir, L. Addadi, S. Weiner, Amorphous calcium phosphate is a major component of the forming fin bones of zebrafish: Indications for an amorphous precursor phase. *Proceedings of the National Academy of Sciences of the United States of America* **105**, 12748-12753 (2008). doi:10.1073/pnas.0803354105

11 E. M. Pouget, P. H. H. Bomans, J. A. C. M. Goos, P. M. Frederik, G. de With, N. A. J. M. Sommerdijk, The initial stages of template-controlled CaCO3 formation revealed by cryo-TEM. *Science* **323**, 1555-1458 (2009). doi:DOI 10.1126/science.1169434

12 J. R. I. Lee, T. Y. J. Han, T. M. Willey, D. Wang, R. W. Meulenberg, J. Nilsson, P. M. Dove, L. J. Terminello, T. van Buuren, J. J. De Yoreo, Structural development of mercaptophenol self-assembled monolayers and the overlying mineral phase during templated CaCO3 crystallization from a transient amorphous film. *Journal of the American Chemical Society* **129**, 10370-10381 (2007). doi:10.1021/ja071535w

13 A. Dey, P. H. H. Bomans, F. A. Muller, J. Will, P. M. Frederik, G. de With, N. Sommerdijk, The role of prenucleation clusters in surface-induced calcium phosphate crystallization. *Nature Materials* **9**, 1010-1014 (2010). doi:10.1038/nmat2900

14 J. Aizenberg, A. J. Black, G. M. Whitesides, Control of crystal nucleation by patterned self-assembled monolayers. *Nature* **398**, 495-498 (1999). doi:10.1038/19047

15 A. M. Travaille, J. Donners, J. W. Gerritsen, N. Sommerdijk, R. J. M. Nolte, H. van Kempen, Aligned growth of calcite crystals on a self-assembled monolayer. *Advanced Materials* **14**, 492-495 (2002). doi:10.1002/1521-4095(20020404)14:7<492::aid-adma492>3.0.co;2-l

16 Y. J. Han, J. Aizenberg, Face-selective nucleation of calcite on self-assembled monolayers of alkanethiols: Effect of the parity of the alkyl chain. *Angewandte Chemie-International Edition* **42**, 3668-3670 (2003). doi:10.1002/anie.200351655

17 C. L. Freeman, J. H. Harding, D. M. Duffy, Simulations of calcite crystallization on self-assembled monolayers. *Langmuir* **24**, 9607-9615 (2008). doi:10.1021/la800389g

18 A. F. Wallace, J. J. DeYoreo, P. M. Dove, Kinetics of silica nucleation on carboxyl- and amine-terminated surfaces: Insights for biomineralization. *Journal of the American Chemical Society* **131**, 5244-5250 (2009). doi:10.1021/ja809486b

19 O. Sohnel, J. W. Mullin, Method for determination of precipitation induction periods. *Journal of Crystal Growth* **44**, 377-382 (1978). doi:10.1016/0022-0248(78)90002-7

20 O. Sohnel, Electrolyte crystal aqueous-solution interfacial tensions from crystallization data. *Journal of Crystal Growth* **57**, 101-108 (1982). doi:10.1016/0022-0248(82)90254-8

21 L. Brečević, A. E. Nielsen, Solubility of amorphous calcium carbonate. *Journal of Crystal Growth* **98**, 504–510 (1989). doi:10.1016/0022-0248(89)90168-1

22 H. Z. Zhang, B. Chen, J. F. Banfield, The size dependence of the surface free energy of titania nanocrystals. *Physical Chemistry Chemical Physics* **11**, 2553-2558 (2009). doi:10.1039/b819623k

23 G. V. Gibbs, T. D. Crawford, A. F. Wallace, D. F. Cox, R. M. Parrish, E. G. Hohenstein, C. D. Sherrill, Role of long-range intermolecular forces in the formation of inorganic

nanoparticle clusters. *Journal of Physical Chemistry A* **115**, 12933-12940 (2011). doi:10.1021/jp204044k

24 D. Quigley, C. L. Freeman, J. H. Harding, P. M. Rodger, Sampling the structure of calcium carbonate nanoparticles with metadynamics. *Journal of Chemical Physics* **134**, 044703 (2011). doi:10.1063/1.3530288

25 D. Gebauer, H. Colfen, Prenucleation clusters and non-classical nucleation. *Nano Today* **6**, 564-584 (2011). doi:10.1016/j.nantod.2011.10.005

26 Felmy, A., D. Girvin, AND E. Jenne. MINTEQ – A computer program for calculating aqueous geochemical equilibria. *U.S. Environmental Protection Agency*, Washington, D.C., EPA/600/3-84/032.

27 J. Aizenberg, A. J. Black, G. M. Whitesides, Oriented growth of calcite controlled by self-assembled monolayers of functionalized alkanethiols supported on gold and silver. *Journal of the American Chemical Society* **121**, 4500-4509 (1999). doi:10.1021/ja984254k

28 F. R. Perez, J. Martinez-Frias, Identification of calcite grains in the Vaca Muerta mesosiderite by Raman spectroscopy. *Journal of Raman Spectroscopy* **34**, 367-370 (2003). doi:10.1002/jrs.1003

29 J. Urmos, S. K. Sharma, F. T. Mackenzie, Characterization of some biogenic carbonates with Raman spectroscopy. *American Mineralogist* **76**, 641-646 (1991).

30 L. Addadi, S. Raz, S. Weiner, Taking advantage of disorder: Amorphous calcium carbonate and its roles in biomineralization. *Advanced Materials* **15**, 959-970 (2003). doi:10.1002/adma.200300381

31 S. Raz, O. Testeniere, A. Hecker, S. Weiner, G. Luquet, Stable amorphous calcium carbonate is the main component of the calcium storage structures of the crustacean Orchestia cavimana. *Biological Bulletin* **203**, 269-274 (2002). doi:10.2307/1543569

32 A. Navrotsky, Energetic clues to pathways to biomineralization: Precursors, clusters, and nanoparticles. *Proceedings of the National Academy of Sciences of the United States of America* **101**, 12096-12101 (2004). doi:10.1073/pnas.0404778101

33 E. M. Pouget, P. H. H. Bomans, A. Dey, P. M. Frederik, G. de With, N. Sommerdijk, The development of morphology and structure in hexagonal vaterite. *Journal of the American Chemical Society* **132**, 11560-11565 (2010). doi:10.1021/ja102439r

34 B. P. Pichon, P. H. H. Bomans, P. M. Frederik, N. Sommerdijk, A quasi-time-resolved Cryo-TEM study of the nucleation of $CaCO_3$ under Langmuir monolayers. *Journal of the American Chemical Society* **130**, 4034-4040 (2008). doi:10.1021/ja710416h

Chapter 3

Development of Liquid Phase TEM System and its Use in Investigating Processes of Nanocrystal Formation and Transformation

Recent ex situ observations of crystallization in both natural and synthetic systems suggest that the classical models of nucleation and growth may be inaccurate. However, in situ observations that can provide direct evidence for alternative models have been lacking due to the limited temporal and spatial resolution of experimental techniques that can observe dynamic processes in a bulk solution. This chapter describes the development of a liquid phase transmission electron microscopy (TEM) platform and its use in studies of nucleation and growth of gold, calcium carbonate, and iron oxide nanoparticles. It is shown how these in situ data can be used to obtain direct evidence for the mechanisms underlying nanoparticle crystallization as well as dynamic information that provide constraints on important energetic parameters not available through ex situ methods.

3.1 Introduction

The experiments described in the preceding chapter highlight a gap in understanding templated nucleation, due to the lack of a platform with which to observe crystallization in situ at high temporal and spatial resolution. In fact, many open questions in crystallization processes remain in part because traditional characterization tools do not allow for direct observations of the phenomena at relevant length and time scales. The dynamics of nucleation, including formation of the nascent particle, attachment and detachment of the fundamental units, and the transient existence and transformation of potential intermediate phases, typically occur at nanometer length scales limiting the utility of in situ optical [1], scanning electron microscopy [2], and x-ray based imaging [3] and spectroscopic methods. In situ scanned probe microscopy has been successfully applied to nucleation and growth in many surface-mediated systems due to its capability of imaging with adequate spatial resolution. However, the early events in materials formation for many materials occur rapidly relative to the time required for image acquisition. Although recent advances in high scan speed approaches have greatly improved the attainable temporal resolution [4], surface scanning techniques are limited in the samples they can characterize. Scanned probe microscopy is of little use, for example, in examining the role of organic matrices, such as globular phases of macromolecules [5], lipid vesicles [6], amelogenin [7], and collagen [8], where mineralization likely occurs within the matrix. More broadly, methods that minimize surface effects are necessary for better understanding crystallization

processes in solution, as surfaces often substantially change the kinetic barriers and free energies that control nucleation [9, 10].

Incorporating such methods in an attempt at reconstructing, for instance, the complete phase pathway for calcite mineralizing on SAMs will therefore likely yield an incomplete picture of the transformation process. The recent advent of liquid phase TEM [11] has provided an experimental platform that provides adequately high spatial and temporal resolutions to probe the early stages of biomineral nucleation and growth. Liquid phase TEM is well-suited for studying template-directed biomineral formation as it allows for the concurrent observation of many different aspects of the process. In addition to nanometer-scale spatial resolution, TEM provides information on crystal phase and orientation through electron diffraction, and can further supply information on chemical composition via energy dispersive x-ray spectroscopy and electron energy loss spectroscopy. With this suite of tools, TEM can potentially allow for studying, among other things, phase pathways of nucleating biominerals and nucleation densities at the point of nucleation in contrast to the indirect, optical approach discussed in the preceding chapter.

The following sections describe the development of a sealed liquid cell TEM platform and its use in the study of a number of systems, to illustrate the power of this method for discriminating between mechanisms at work during the formation of inorganic crystals. While quantitative analyses of certain phenomena are provided, the intent of this chapter is to provide a qualitative overview that shows how liquid phase TEM can be used to explore a number of processes in nucleation and crystal growth that are currently the subjects of intense study within the geochemical, biomineral and crystal growth communities.

3.2 Liquid Cell Development

The cell design described in this chapter was based on the pioneering work of researchers at I.B.M. [11], who used liquid phase TEM to quantitatively study the nucleation and growth of electrodeposited Cu islands on Au electrodes [12-14]. A side-view schematic of the initial design can be seen in Figure 3.1A. The cell was composed of two 300 micron thick silicon wafers with silicon nitride membranes coating both sides of each wafer. Photolithography methods were used to pattern wafers for selective etching. The silicon nitride film was removed using reactive ion etching, exposing the underlying silicon wafer. Wafers thus prepared were submerged in KOH solutions for silicon etching, to produce suspended nitride membranes which constitute the electron-transparent windows of the liquid cell, as well as solution reservoirs to either side of the imaging area. On the lower wafer, reactive ion etching removed the nitride to expose vias to the underlying highly doped silicon wafer, and evaporative deposition of 5 nm Ti and 20 nm Au produced thin film electrodes for use as the working electrode of an electrochemical cell. Additionally on the lower wafer, plasma enhanced chemical vapor deposition was used to deposit a spacer layer of silicon nitride, to create the gap to support a fluid layer of an appropriate thickness. The spacer layer thickness was tailored to the experiment, typically ranging between 200-500 nm. A fully assembled in situ cell wired for electrochemistry and secured on the TEM fluid stage is shown in Figure 3.1B.

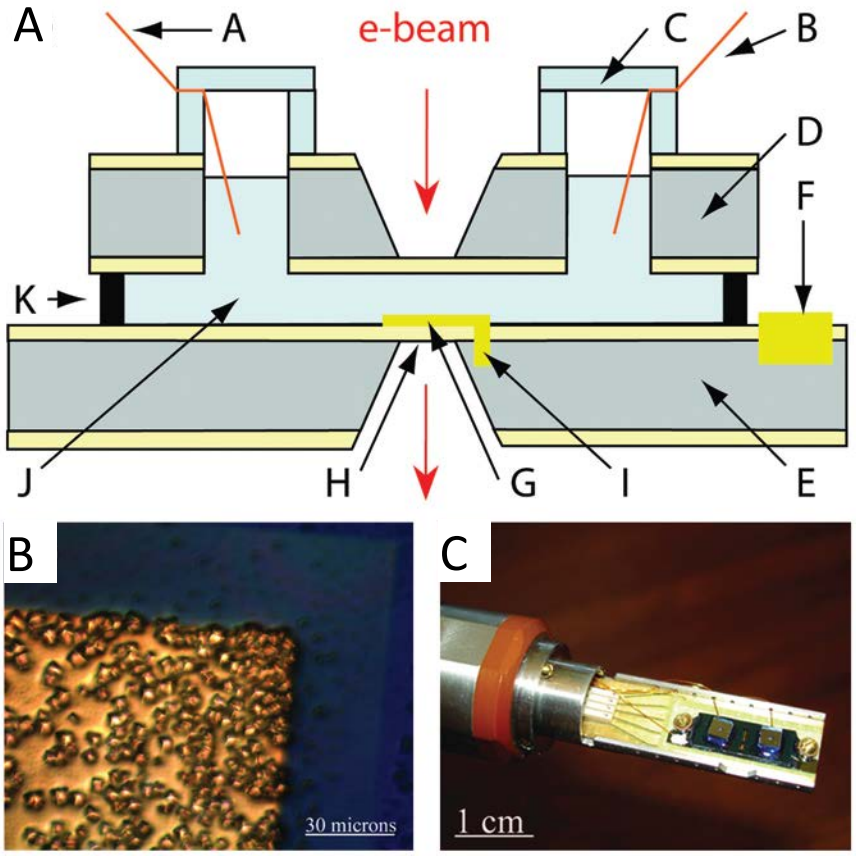

Figure 3.1 (A) Schematic cross-section of fluid cell. A, B: Reference and counter electrodes, C: Glass cap, D, E: 100nm Si_xN_y/300μm Si(100)/100nm Si_xN_y wafers, F, G: 5nm/20nm Ti/Au working electrode, H: Si_xN_y window, I: Electrical contact between Si(100) and Au, J: Solution reservoir, K: 200-500nm Si_xN_y spacer. (B) Photograph of fluid cell wired for electrodeposition and secured onto TEM stage. (C) Optical micrograph of electrodeposited calcite crystals on bench-top test of fluid cell components.

In order for liquid phase TEM to be useful in understanding materials formation processes, it must provide control over the reaction so that the phenomena can be observed in the microscope. A trigger mechanism is necessary to drive the reaction from a stable reagent solution, or one that reacts at a slow enough rate, such that the system can be prepared for data acquisition prior to the start of the reaction. To this end, two elements for manually providing a driving force were incorporated into the system described herein.

The stage incorporated electrical connections that allowed for wiring the liquid cell to external equipment for controlled biasing of the cell. For the primary interest of $CaCO_3$ formation, a sufficiently high electrical bias applied to the working electrode of an electrochemical cell reduces the dissolved molecular oxygen in the solution, producing hydroxide ions at the metal/liquid interface and increasing the pH at the surface of the electrode [15]. This increases the supersaturation of $CaCO_3$ and drives mineralization. The results of a bench-top electrodeposition test on an unassembled cell component are shown in Figure 3.1C.

The optical image shows that the driving force is highly localized and that mineralization occurs primarily on the electrode; proper fluid cell design can restrict the active area to regions observable in the TEM.

To control the temperature of the liquid cell, the custom fluid stage (Hummingbird Scientific) incorporated a Peltier device and the cell design provided an attachment site for a thermocouple to allow measurement of the fluid cell's temperature. The on-stage Peltier allowed temperature modulation in the range of $5℃ < T < 70℃$ and was tested to be stable within $\pm 0.05℃$ over the course of at least one hour. Based on the temperature dependence of a material's solubility, the temperature of the system can be modulated to suppress the reaction until ready for imaging and then drive the process forward while synchronizing image acquisition.

Over the course of extensive testing of the system detailed above, a number of issues came to light that significantly hindered the ability to conduct experiments in the TEM. One of the major issues was with the design of the electrochemical set-up, with problems arising both from the use of wires as counter and reference electrodes as well as the design of the working electrode patterned onto the lower cell component. It was found that the wires interfered with achieving a secure seal at the towers, often with the result that pin-hole leaks developed in the glue line and resulted in the solution leaking out of the cell over time. In addition, the reaction solution tended to wick out of the reservoir along the wire, lowering the liquid level to the point that the wire was no longer submerged, thus disconnecting the electrode from the system.

The working electrode was found to be problematic due to electrical connectivity issues and an excess of active area outside of the imaging window. To be able to observe nucleation and growth of materials on the electrode at the initial stages of the process the electrode must be suitably thin. As such the electrodes were fabricated by depositing 5 nm Ti as an adhesion layer and 20 nm Au for the electrode. It was found, however, that this thin layer of metal often developed a break between the regions covering the nitride and the via into the underlying silicon, causing the electrode section extending over the imaging window to be disconnected from external control.

Even when the electrode had continuity out to the imaging area, the portion of the electrode visible in the microscope constituted only 15-20% of the total active area. This resulted in a sizable probability of nucleation events occurring on regions of the electrode not visible in the microscope, decreasing the likelihood of making successful observations in a given experiment. In addition to the aforementioned design issues, investigating SAM-templated calcite nucleation would be problematic, because the thiol-gold bond strength is similar in magnitude to the applied electrical bias needed to drive mineralization [16].

There was also a significant design issue with the size of the nitride windows. The window on the upper part was greatly elongated transverse to the body of the fluid stage to facilitate EDS analysis with minimal tilting of the stage. The large size of the window, however, made the window both more fragile and subject to a large amount of flex. The window can bow out from the cell during fluid injection and sealing of the cell, and can also flex inward following the curing of the sealant. In the event that it bows out, the resultant fluid layer thickness can be microns thick rather than the desired, nominal sub-micron thickness. Further complicating matters, when filling the cell with solution it is not uncommon for a pocket of air to get trapped under the window as it bows out. Such air bubbles are difficult to remove from the cell and seem

to promote the trapping of more bubbles if an attempt is made to dry the cell and refill it. When a bubble covers the imaging area it renders the cell useless for in situ imaging. When the window flexes inward, the two windows can press together and force out any liquid that was previously in the imaging area.

The design issues raised above led to a number of modifications to the cell shown below in Figure 3.2. All three of the electrodes are now patterned on the surface of the nitride membrane on the lower wafer, eliminating the need to feed wires into the cell and eliminating continuity problems from breaks in the electrode conduction path. In addition to depositing the spacer layer for separation of the two major cell components, a passivation layer is now deposited over much of the electrode surface area internal to the cell. The result is that the section of the working electrode visible in the TEM is around 80% of the total active area of the electrode, greatly decreasing the chance that reactions occur outside the visible area. For studies that involve SAMs, the working electrode is now patterned across the window with e-beam lithography to produce patches of gold electrically isolated from the electrode but separated by no more than a few microns, so that they should still be in the region of increased pH as a bias is applied to the nearby electrode [17, 18]. To mitigate window flex, the area of the upper window has been greatly reduced, which also decreases the likelihood of bubbles becoming trapped between the windows. Although the window is now a fraction of its original size, EDS is still possible as the stage has a tilt range of $\pm 25°$.

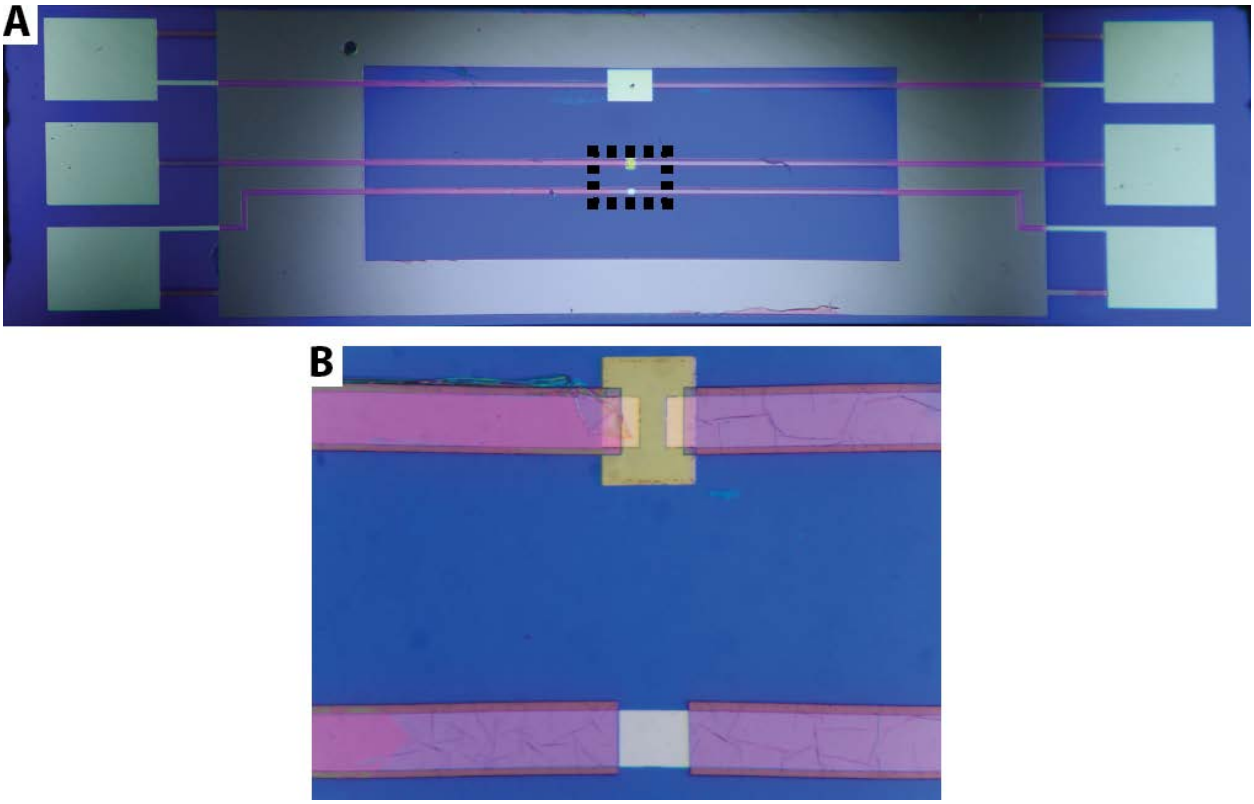

Figure 3.2 Redesigned static liquid cell. (A) All of the electrodes are patterned onto the lower cell wafer, with external connection points on either end of the wafer. (B) Boxed region in (A) highlights the passivating layer of SiO_2 that is deposited over the electrode regions internal to the liquid cell, exposing only small active regions so that the reaction zone is limited to the area visible in the TEM.

3.3 Materials and Methods

3.3.1 TEM Liquid Cell Assembly

Silicon-based liquid cell components fabricated as described in the preceding section, were used for the experimental work described below. The two primary components were glued together by drawing a small bead of epoxy (M-Bond 610) around the outer edges of the aligned wafers and curing on a hot plate, ramping the temperature from room temperature to 120°C over the course of an hour. Two silicon towers that act as solution reservoirs were glued to the upper wafer using the same epoxy. The vast bulk of the fluid cell's reaction volume (total volume 1–2 μL, depending on specific geometry) resides in these solution reservoirs, with a small fraction of the total volume expected in the thin layer between the silicon wafers. With the cell thus assembled, solution was injected into one of the reservoirs, where it was drawn through the cell via capillary action. The second reservoir was then filled with solution. Silicon or glass caps

were placed over the reservoir openings and sealed to the towers using a UV-curable epoxy (Norland Opticure 63).

3.3.2 Solution Preparation

The gold solution was made by mixing 0.5 mL of a 0.01 M Na-citrate solution and 0.5 mL of 0.01 M $HAuCl_4$ solution to 18 mL of DI water. Freshly prepared $NaBH_4$ solution (0.3 mL of 0.01 M) was added to Au-citrate solution to form the gold nanoparticles. The solutions used in these experiments had aged at room temperature for a period of less than a month before use.

Iron (III) chloride (99%, Aldrich) and potassium dihydrogen phosphate (98%, Aldrich) from Sigma Aldrich (St. Louis, MO, USA) were used as received. Iron oxide particle synthesis was achieved by mixing $FeCl_3$ and KH_2PO_4 solutions to produce a working solution with 20 mM Fe^{3+} and 0.45 mM K^+ at pH 2.05 to 2.08. For in situ experiments, a few microliters of the $FeCl_3$-KH_2PO_4 solution were loaded into the liquid cell, which was sealed and placed into the microscope. Rod-like akaganeite nanoparticles and spindle shaped hematite nanoparticles were produced in ex situ reactions with this solution at 100–150°C for 0.5–48 h by a hydrothermal method in sealed 23 mL Teflon-lined autoclaves.

Two types of calcium carbonate solutions were used. The first was prepared by mixing together reagent solutions to yield a solution containing 5 mM $CaCl_2 \cdot H_2O$ (Sigma-Aldrich 99.999%) and 5 mM $NaHCO_3$ (Alfa Aesar 99.998%). Additional calcium carbonate solutions were prepared by mixing equal volumes of a 20mM carbonate buffer (mixture of Na_2CO_3 and $NaHCO_3$) and a solution of 20mM $CaCl_2$ with 2 μM of the sea urchin spicule matrix protein SM50. As the SM50 was expected to stabilize the amorphous $CaCO_3$ phase indefinitely, this solution was allowed to sit at room temperature for months before use.

3.3.3 TEM Operation

The cell described above was used in conjunction with a custom-built TEM stage (Hummingbird Scientific) designed to work with JEOL microscopes. Two microscopes were used for the data collected and reported herein: a LaB_6 JEOL JEM-3010 operated at 300 kV and a field emission JEOL JEM-2100F operated at 200 kV. Video data was collected using the VirtualDub software to either directly capture data from the camera (JEM-3010) or collect cropped screenshots of the live view in Digital Micrograph (JEM-2100F). Image acquisition times ranged from 0.05 to 0.25 s per image and the image size was either 1001 ± 1 × 666 ± 1 pixels (JEM-2100F) or 480 × 480 pixels (JEM-3010).

3.4 Results

3.4.1 Nucleation of Au Nanoparticles

Numerous groups have investigated various aspects of gold nanoparticle growth and motion [19, 20]. The following study looked at the initial nucleation of Au nanoparticles. Figure 3.3 shows the process of gold nanoparticle formation from a gold chloride solution containing citric acid as a capping agent. While numerous successful particle formation events are observed, there are many instances in which a gold particle begins to form, fluctuates in size, and eventually dissolves away rather than growing into a stable crystal. These fluctuations demonstrate that gold nanoparticles form from solution via a true nucleation process in which sufficiently large density fluctuations are required to take the system over a free-energy barrier and justify a description of the system in terms of the classical rate equation [21]:

$$J_n = Ae^{-E_A/\mathbf{k}T}e^{-\Delta g_c/\mathbf{k}T} \tag{3.1}$$

where J_n is the nucleation rate per volume, $\mathbf{k}$ is Boltzmann's constant, T is the temperature, E_A is the activation energy associated with the atomic processes such as desolvation and attachment that must occur to form the nucleus, and Δg_c is the free energy change required to create a critical-size particle relative to that of the free ions. (Without the second barrier, Equation (3.1) would simply describe a chemical reaction that proceeds at a rate fixed by the kinetic barriers to the atomic scale processes.) This result shows that, whether or not multi-ion clusters—stable or unstable—below the resolution of the measurement contribute to formation of the super-critical nuclei, the process exhibits the characteristic feature of classical nucleation.

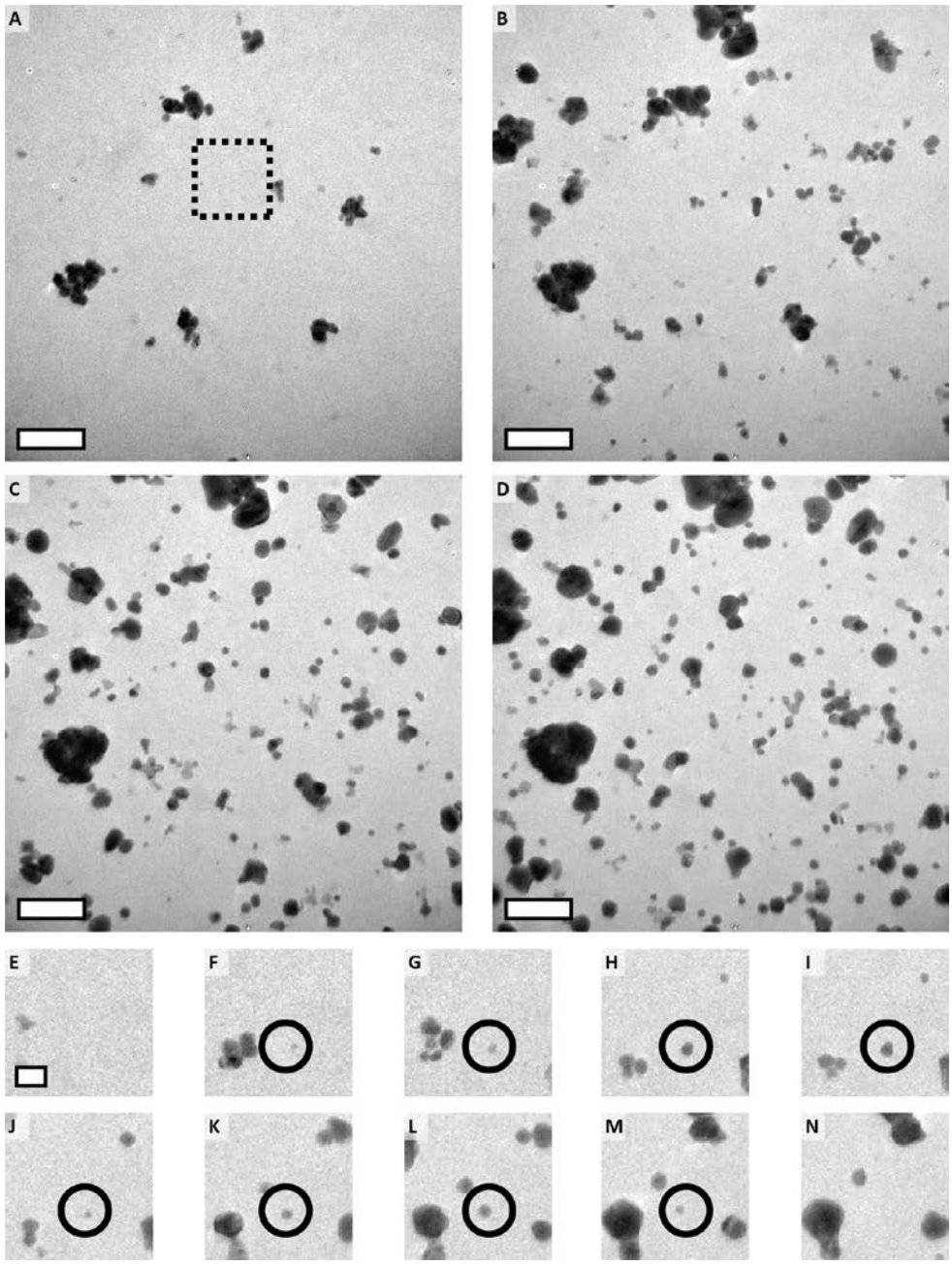

Figure 3.3 Nucleation of Au nanoparticles. A–D: Sequence of liquid cell transmission electron microscopy (TEM) images showing the nucleation of Au nanoparticles from a gold chloride solution containing citrate as a capping agent. As seen in the example highlighted by the circle in (E–N), which were taken from the region delineated by the rectangular box in (A), many of the nascent nuclei fail to reach the point of spontaneous growth and instead fluctuate in size until they disappear. This behavior demonstrates that particle formation results from unstable fluctuations, the hallmark of classical nucleation. Times in seconds: (A) 0.0, (B) 34.0, (C) 68.1, (D) 103.2, (E) 2.1, (F) 8.0, (G) 16.4, (H) 34.9, (I) 36.6, (J) 44.8, (K) 60.5, (L) 73.1, (M) 93.3, and (N) 103.2. Scale bars: (A–D) 500nm, (E–N) 200 nm.

In the classical model, the barrier results from the competition, in the growing particle, between the decreasing bulk free energy and the increasing surface free energy. Defining the supersaturation as σ and the surface free energy as α, the barrier and critical size become [21, 22]

$$\Delta g_c = B\frac{\alpha^3}{\sigma^2} \tag{3.2}$$

$$r_c = \frac{F\omega\alpha}{\mathbf{k}T\sigma} \tag{3.3}$$

with $B = \Phi(\omega/\mathbf{k}T)^2$, where F and Φ are shape factors equal to 2 and 16/3 for a spherical nucleus and ω is the volume per atom in the solid. Once incipient nuclei exceed the critical radius r_c, on average they grow rather than shrink. Consequently, by examining the particles that fail to grow one can estimate r_c for the system. (An accurate measure of r_c can be obtained by determining the particle size at which half the particles grow and half shrink, but this requires a large number of events and can be biased by the lower limit of resolution.) If one estimates the critical radius by measuring the maximum diameter reached by incipient nuclei that dissolve instead of continuing to grow, from Figure 3.3, a critical radius of 25 ± 4 nm (based on measurements of eight particles where the error is 1 SD) is obtained. Unfortunately, because neither the value of α for citrate-capped gold nor the supersaturation of the solution under the beam are known, the value of r_c cannot be used to estimate either quantity independently.

3.4.2 Nanoparticle Aggregation and Coalescence

Observations of post-nucleation aggregation of nanoparticles suggests three distinct styles. In the first one, which is illustrated by the ferrihydrite (iron oxyhydroxide) system (Figure 3.4), nanoparticles become co-aligned prior to or during the attachment process so that the lattices of the contacting surfaces match. The result is that aggregation events create branched structures with interfaces that are either defect-free or delineated by twin planes. The sequence of images in Figure 3.4 was chosen because it illustrates the unique dynamic information provided by liquid cell TEM. The sequence shows an oblong particle presumably formed during an earlier OA event drifting by a larger branched particle formed through numerous aggregation events. As the lower left corner of the smaller particle passes near the larger mass with a relative orientation that is close to alignment, it experiences the attractive force that drives OA in this system [23]. This force exerts a torque on the particle rotating it clockwise into co-alignment and causing the final jump-to-contact. However, even after the initial attachment, line defects can be seen in the interface region and their elimination leads to a large readjustment of the alignment marked by a visible counterclockwise rotation. The end result of these events is to create a highly branched single crystal that could not form through the classical terrace-ledge-kink model of growth.

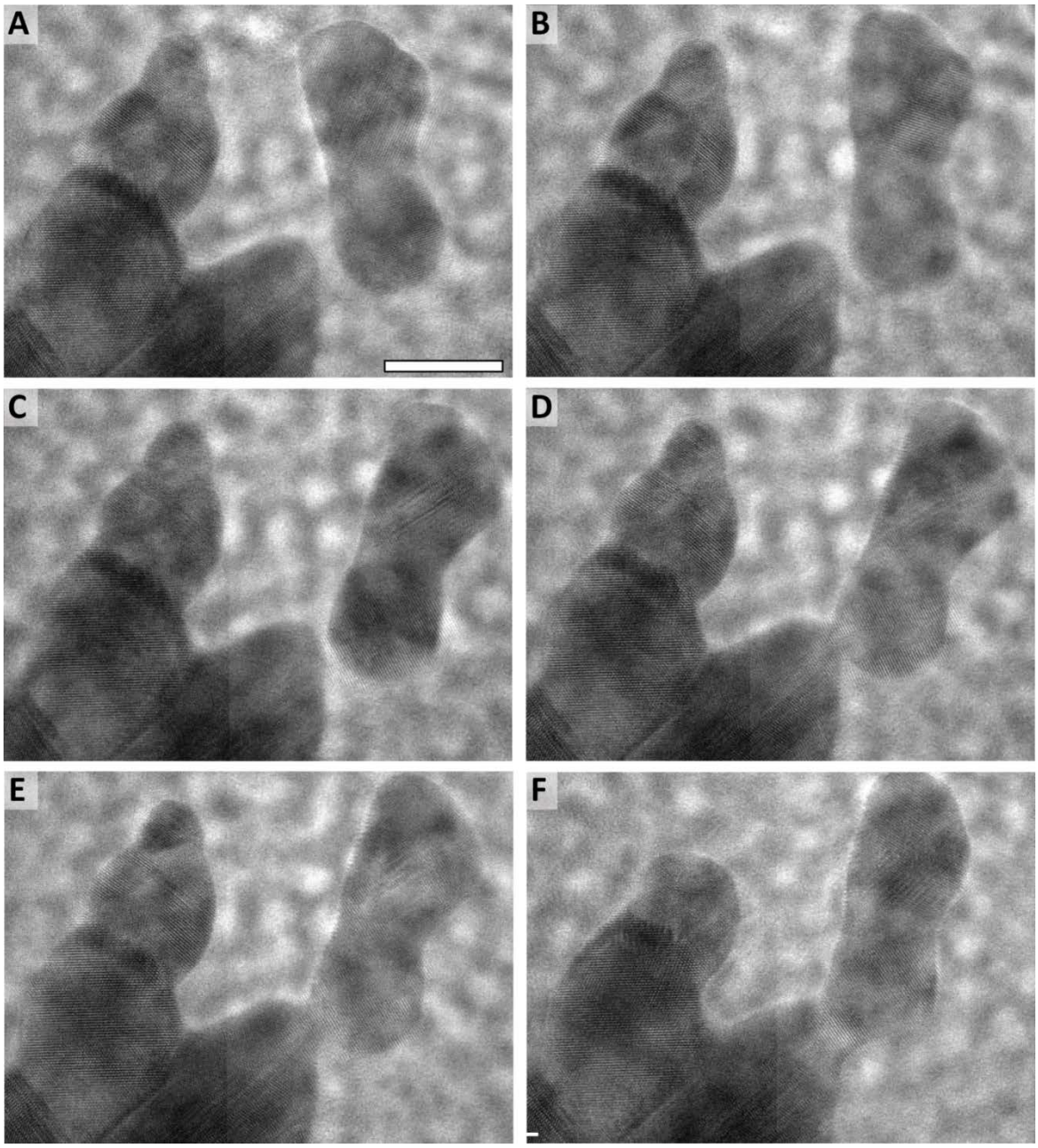

Figure 3.4 Growth of ferrihydrite (iron oxyhydroxide) via OA. A–F: Sequence of liquid cell transmission electron microscopy (TEM) images showing a dumbbell-shaped ferryhidrite particle formed during an earlier aggregation event, attaching to a larger crystal formed from many such events. As the dumbbell-shaped particle approaches the larger crystal (A–B), it feels the attractive force that drives OA and undergoes a significant clockwise rotation (B–D) before jumping to contact (C–D). Immediately following attachment, there are a number of lattice defects in the boundary region (D–E), but these quickly translate to the surface and are expelled, causing a counter-clockwise rotation of the particle about the new interface (F). Times in seconds: (A) 0, (B) 2.4, (C) 5.6, (D) 6.6, (E) 7.4, and (F) 32.2. Scale bar is 10 nm.

Measured values of rotational and translational accelerations during jump-to-contact were used [23] to calculate the magnitude of the interaction potential in the ferrihydrite system. Assuming the underlying source of OA is Coulombic, as suggested by simulations [24], it was found that approximately one net unit charge on each particle would be required to create the estimated attractive force.

The torque τ that must be applied through relaxation of the interface in order to rotate the particle in Figure 3.4 through the observed post-attachment rotation angle θ can also be estimated from these experiments. Figure 3.5 shows the dependence of the relative angle on time. During the first 2 s, the particle rotates counterclockwise through an angle of 10° in 2 s giving a rate $\omega = 87$ mrad/s. Because the dependence of angle on time is linear over this angle, the angular velocity is a constant, thus the net torque is zero. This means the torque due to relaxation of the interface is approximately equal to the resistive torque τ_r due to rotation in the viscous medium. Following Li *et al.* [23], $\tau_r = 8\pi\eta r^3\omega$ where r is the distance to the center of mass from the contact (11 nm) and η is the viscosity, which is 5.8×10^6 g cm^{-1} s^{-1} for this system. The total energy of relaxation U required to cause this rotation can then be estimated from $U = \tau_r\theta = 3.0 \times 10^{-12}$ erg. (If instead the energy needed to move an ellipsoid against the Stokes force through the distance $r\theta$ is calculated, the estimated value of U becomes 1.9×10^{-12} erg, showing that the calculation is insensitive to the detailed geometry assumed.) One can get an order of magnitude estimate of the internal strain ε this energy corresponds to from $U \sim (1/2)VE\varepsilon^2$ where V is the volume of deformation and E is the elastic modulus, which is of order 10–100 GPa for inorganic solids. Taking $E = 50$ GPa, a radius of ~ 5 nm at the interface and a deformation region of ~ 5 nm in thickness (from Figure 4), the strain is estimated to be ~ 0.01 or about 1%.

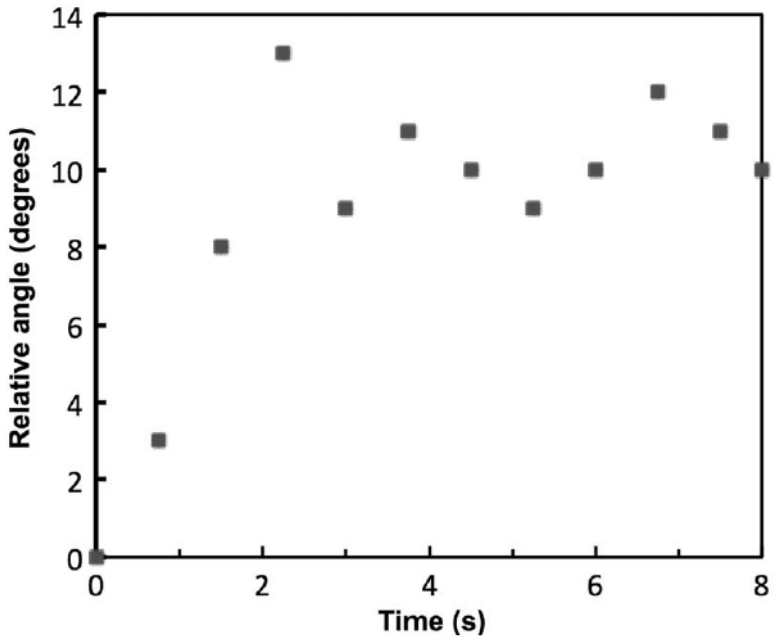

Figure 3.5 Dependence of relative orientation versus time following attachment of dumbbell-shaped ferryhidrite particle shown in Figure 3.4. The particle rotates counter clockwise at a rate of 87 mrad/s before reaching an equilibrium position.

Because the interaction of the particles often brings a small particle near a large particle, if the local curvature of the two particles differs significantly the process of integration can involve Ostwald-type ripening instead of aggregation. Figure 3.6 shows an example for the ferrihydrite system. A small particle with high positive curvature approaches a large ferrihydrite surface with negative curvature. Before an attachment event can occur, the small particle dissolves and is incorporated into the larger particle.

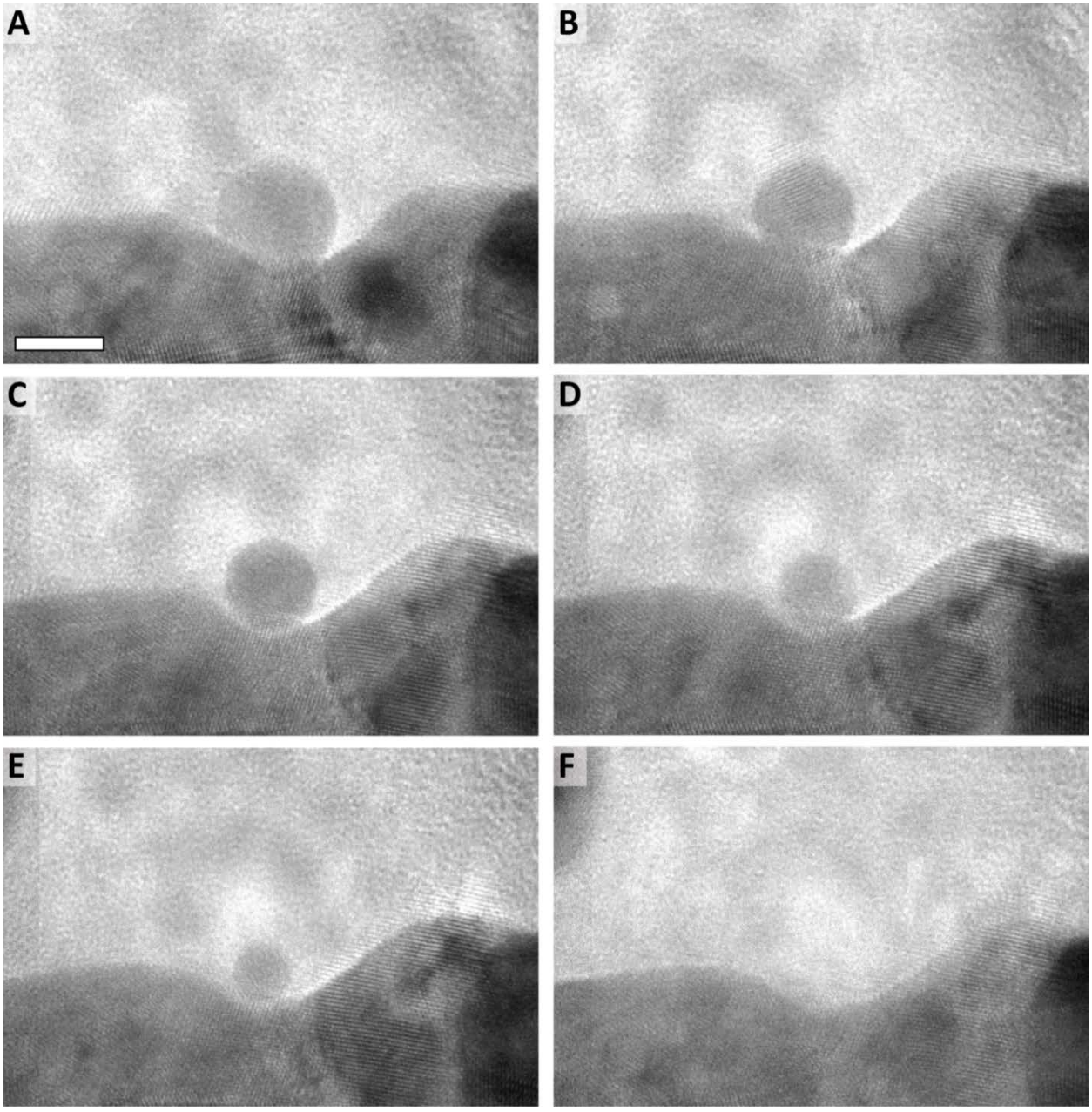

Figure 3.6 Ostwald ripening of ferrihydrite particles. Sequence of liquid cell transmission electron microscopy (TEM) images (A–F) show the dissolution of a small ferrihydrite particle with positive curvature near a large ferrihydrite surface with negative curvature. Times in seconds: (A) 0, (B) 4.6, (C) 7.6, (D) 10.2, (E) 12.6, and (F) 14.6. Scale bar is 5 nm.

The dependence of particle size on time during the ripening process for the particle shown in Figure 3.6, as well as one other not shown here, is given in Figure 3.7. Although the two particles appear in similar local particle-particle interaction environments, the dissolution kinetics are quite different. For particle 1, the fit to the third power law in Figure 3.7B shows that

its dissolution can be described well by Ostwald ripening controlled by the volume diffusion of ionic species in a solution [25]. On the other hand, the data for particle 2 cannot be described by any power law, suggesting factors other than size, such as the relative orientations of the dissolving and growing particles or the local environment (e.g., interface curvature), play a role in the dissolution and re-precipitation rate. The accelerated dissolution rate of this particle at $> \sim 12$ s may also reflect the rapid increase in Coulombic interactions at close proximity as the effect of surface charge screening diminishes [26].

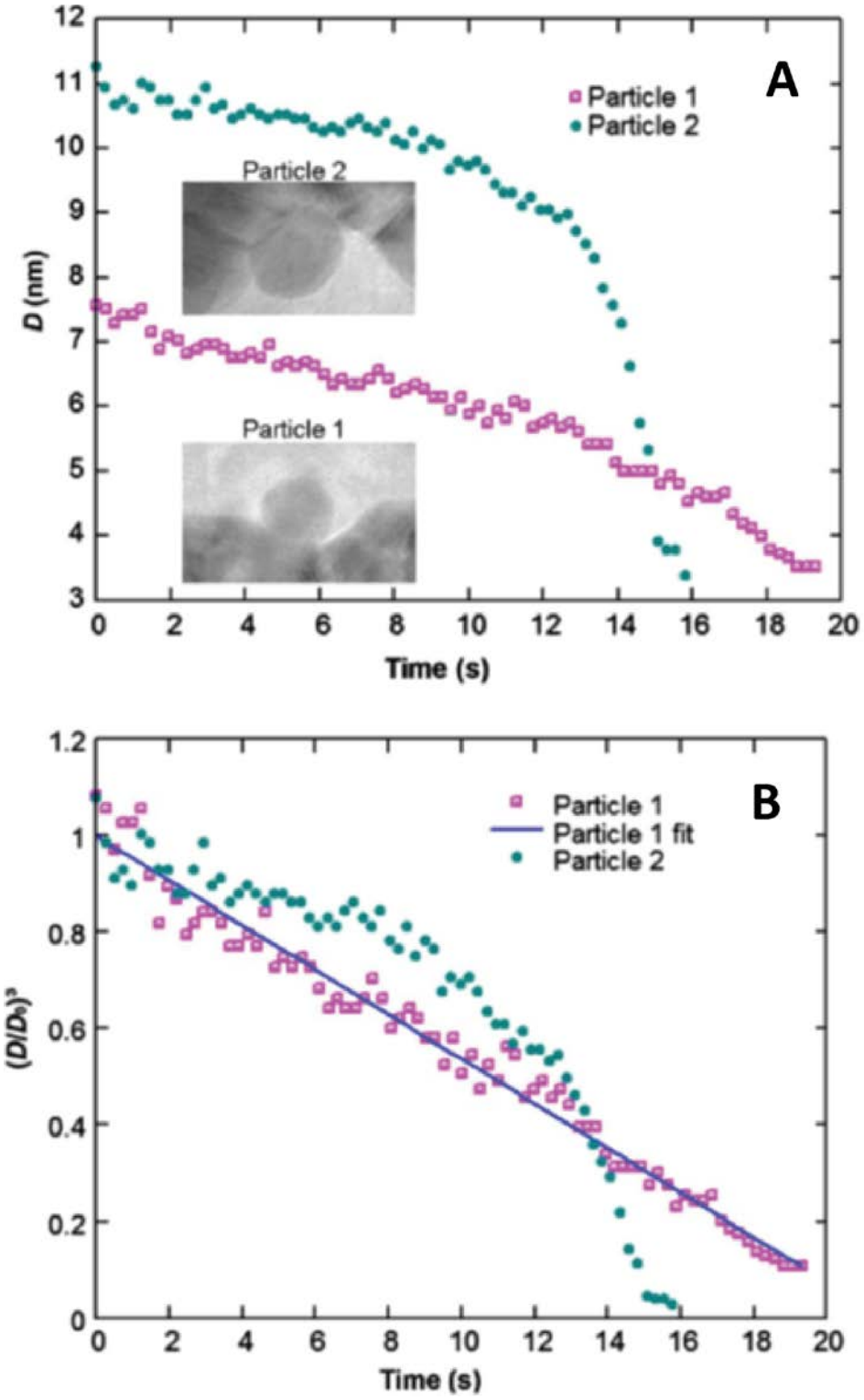

Figure 3.7 (A) Decrease in diameter with time for an individual particle near a concave surface of a much larger particle. Particle 1 is the same one shown in Figure 3.6. (B) Plot of $(d/d_0)^3$ versus time for the two particles shown in (A).

Observations in the calcium carbonate system suggest a very different aggregation process than in the ferrihydrite system. Here, particle fusion is also observed, but the primary particles, which are of order 5 nm or less and spherical, appear to be amorphous (Figure 3.8). This conclusion is consistent with molecular dynamics simulations [27, 28], which found that amorphous calcium carbonate should be the stable phase in the nm-range, despite the fact that all macroscopic crystalline phases of $CaCO_3$ have much lower solubility (i.e., higher stability). These primary particles interact with and periodically attach to a larger particle that was created through prior aggregation events and is crystalline, as is evident from the faceted shape, the presence of lattice fringes, and the constantly changing scattering contrast. After attachment, lattice fringes can be seen in the smaller particles as well, indicating that growth in this system does not occur through OA, but rather via attachment of amorphous particles that then crystalize using the parent crystal as a template. Interestingly, during one experiment in which many well-formed crystals ranging in size from about 10 to 50 nm interacted over a period of several minutes, attachment events were not observed, suggesting that true OA in this system may be a rare event.

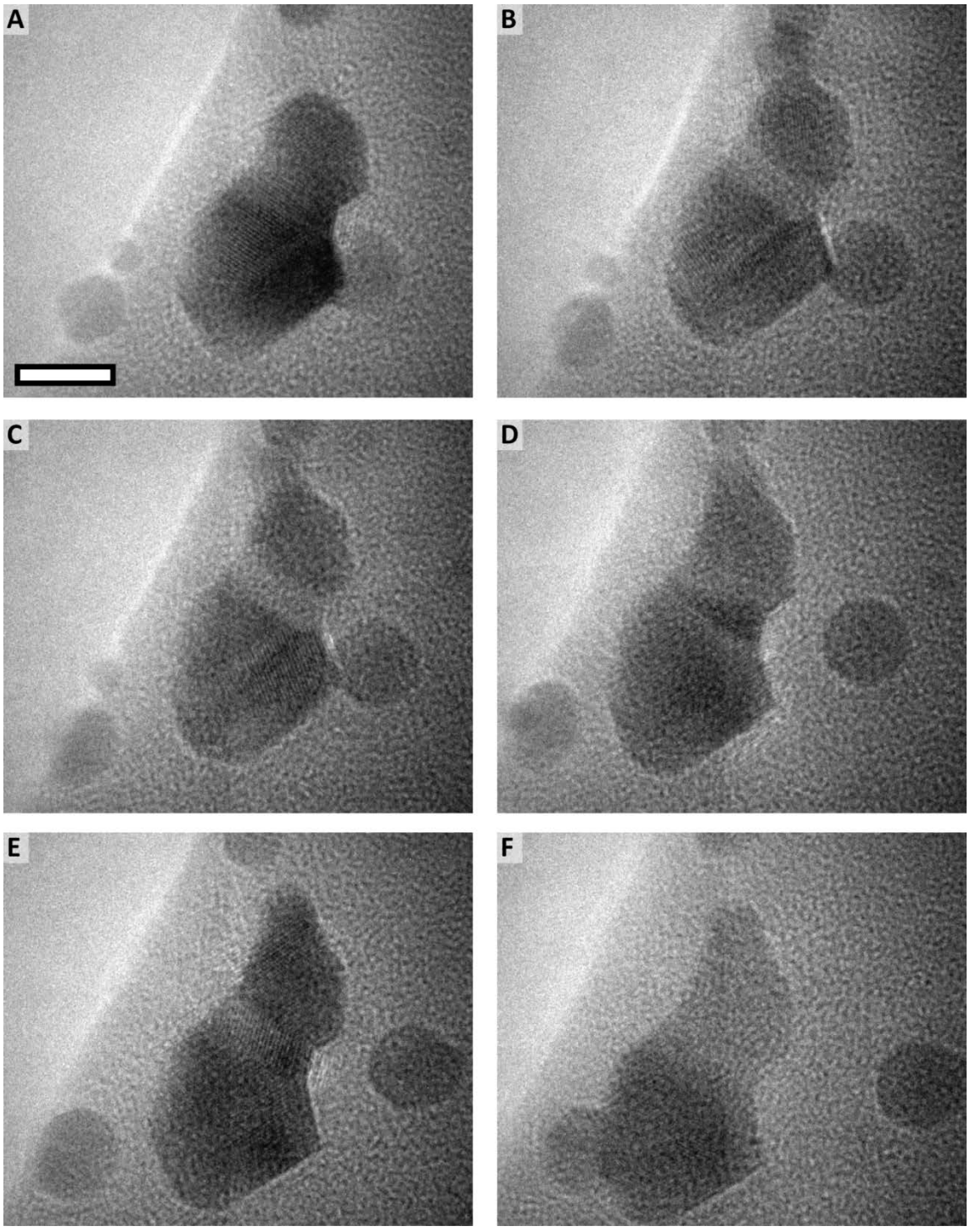

Figure 3.8 Growth of CaCO3 by particle aggregation. Sequence of liquid cell transmission electron microscopy (TEM) images (A–F) show small spherical $CaCO_3$ particles with no apparent lattice structure interacting with and attaching to either one another or to a larger composite crystal. Times in seconds: (A) 0, (B) 0.8, (C) 1.3, (D) 3.3, (E) 4.5, and (F) 6.5. Scale bar is 5 nm.

The third style of aggregation-based growth is illustrated by the akaganeite-hematite system. Akaganeite (an iron oxyhydride) forms nanorods in solution that may aggregate to eventually form spindle-shaped single crystals of hematite (an iron oxide) [29, 30]. In the akaganeite-hematite system, phase transition and growth appear interlinked, as in the calcium carbonate system, but in this system both primary and secondary particles are crystalline. Frandsen *et al.* [30] used ex situ and cryo-TEM to develop a model for the formation of these spindles based on OA of the akaganeite nanorods followed by transformation to hematite due to a size-dependent inversion of the iron oxide phase stability; after which spindle growth happens by aggregation of akaganeite onto hematite. In this study, liquid cell TEM shows hematite spindles in the solution with akaganeite nanorods and significant network formation between particles (Figure 3.9A). Although the rods tend to exhibit at least partial co-alignment, the images here show that the nanorods initially aggregate with a high degree of disorder compared with that observed during ferrihydrite aggregation (Figure 3.4) [23]. Disorder is further evident in early hematite spindles based on diffraction contrast (Figure 3.9C), lattice images (Figure 3.9D), and Fourier transform analysis (Figure 3.9D, inset), but this disorder is eliminated over time through internal reorganization to produce highly perfect single crystal hematite spindles (data not shown). Thus this system is intermediate between the case of ferrihydrite, where attachment is highly orientation dependent (as observed from lattice plane alignment), and that of calcium carbonate where the precursor is amorphous and hence overall particle orientation plays no role. Nonetheless, in all three cases the final crystals are highly perfect single crystals.

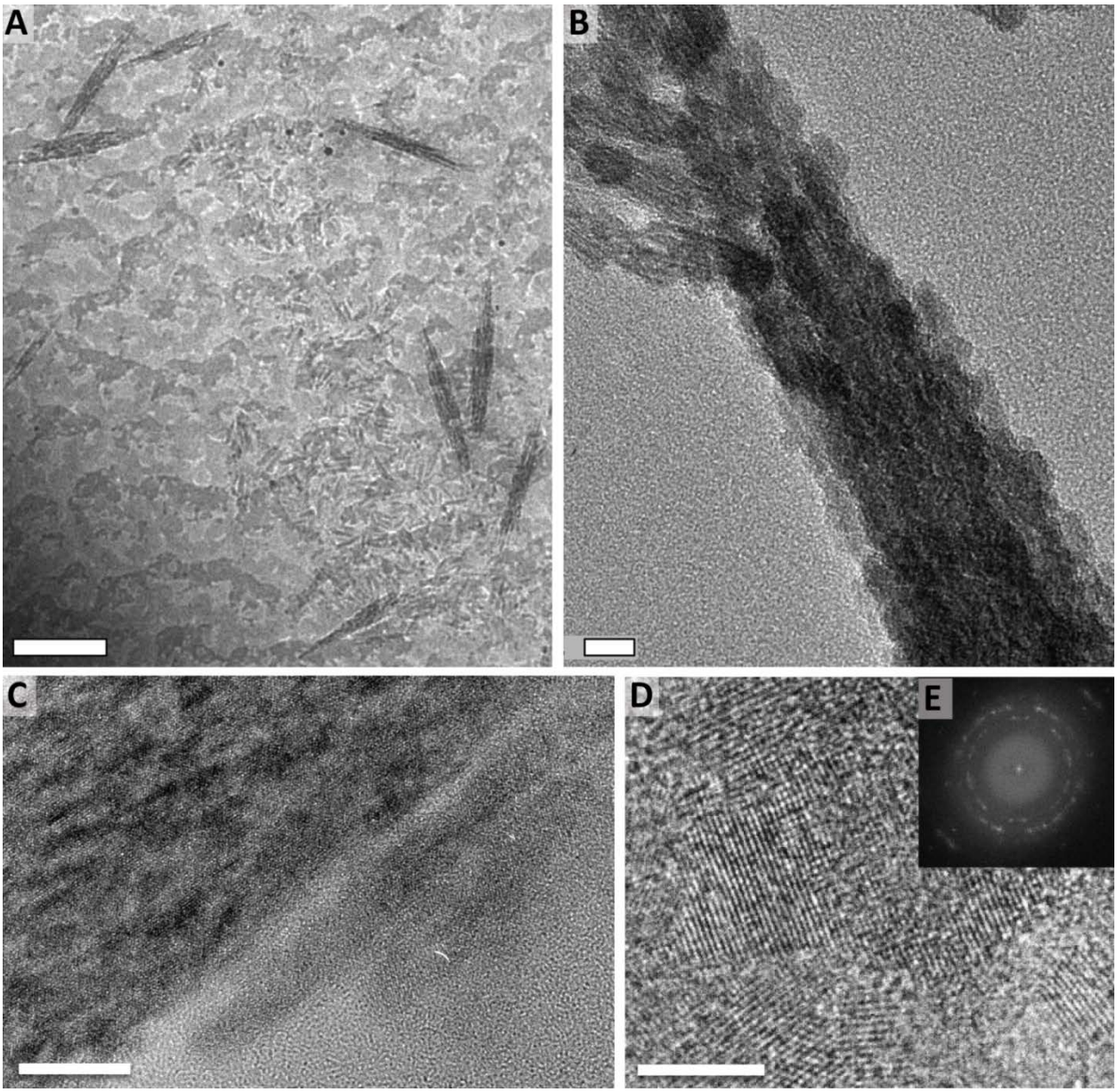

Figure 3.9 Growth of hematite (α-Fe2O3) spindles through aggregation of akaganeite nanorods (β-FeOOH). (A) Liquid cell transmission electron microscopy (TEM) shows complete spindles, partial spindles, and nanorods. (B) Ex situ image from same experiment showing assembly of the nanorods into a spindle. (C, D) High resolution images indicating that the akaganeite nanorods attach to the hematite spindles (C), but in this early stage the resulting hematite crystals are composed of randomly oriented domains (D, inset). After an extended period of hydrothermal treatment, the hematite spindles become single crystal and exhibit a single well-defined diffraction pattern (data not shown). Scale bars: (A) 200 nm, (B) 10 nm, (C) 10 nm, (D) 5 nm.

3.4.3 $CaCO_3$ nucleation on Au

TEM imaging in the liquid cell has been conducted in conditions such that the electron beam was not the primary driving force for the reaction [11-14], but imaging has also been carried out with the intent of having the electron beam initiate the process, as demonstrated, for example, in a study of the formation of platinum nanoparticles [31]. Although the liquid phase TEM system described in this chapter was designed to control nucleation and growth of $CaCO_3$ by the application of a measured thermal or electrochemical driving force, it was found that beam effects under conditions of high electron beam intensity could also initiate $CaCO_3$ nucleation and growth in the fluid cell.

The initial stages of $CaCO_3$ formation on the Au electrode are shown in Figure 3.10. Prior to the onset of mineralization, the Au electrode can be seen as the dark structure extending across the bottom and right side of the image, and the silicon nitride window as the light gray area (Figure 3.10A). In the first few seconds numerous particles with no discernable structure nucleated on the surface and along the edge of the electrode (Figure 3.10B-D). These particles can be seen as the small round protrusions around 15 nm in size (Figure 3.10B). Although these particles are presumably ACC given their lack of structure, one cannot rule out the possibility that they are vaterite as this crystalline phase can adopt a discoidal morphology. After about 60 seconds of growth the ACC particles merged together and began conversion into faceted crystals (Figure 3.10E-G). Following the conversion of ACC to the crystalline phase, the initially formed crystals merged and continued to grow into larger faceted crystals (Figure 3.10H-I).

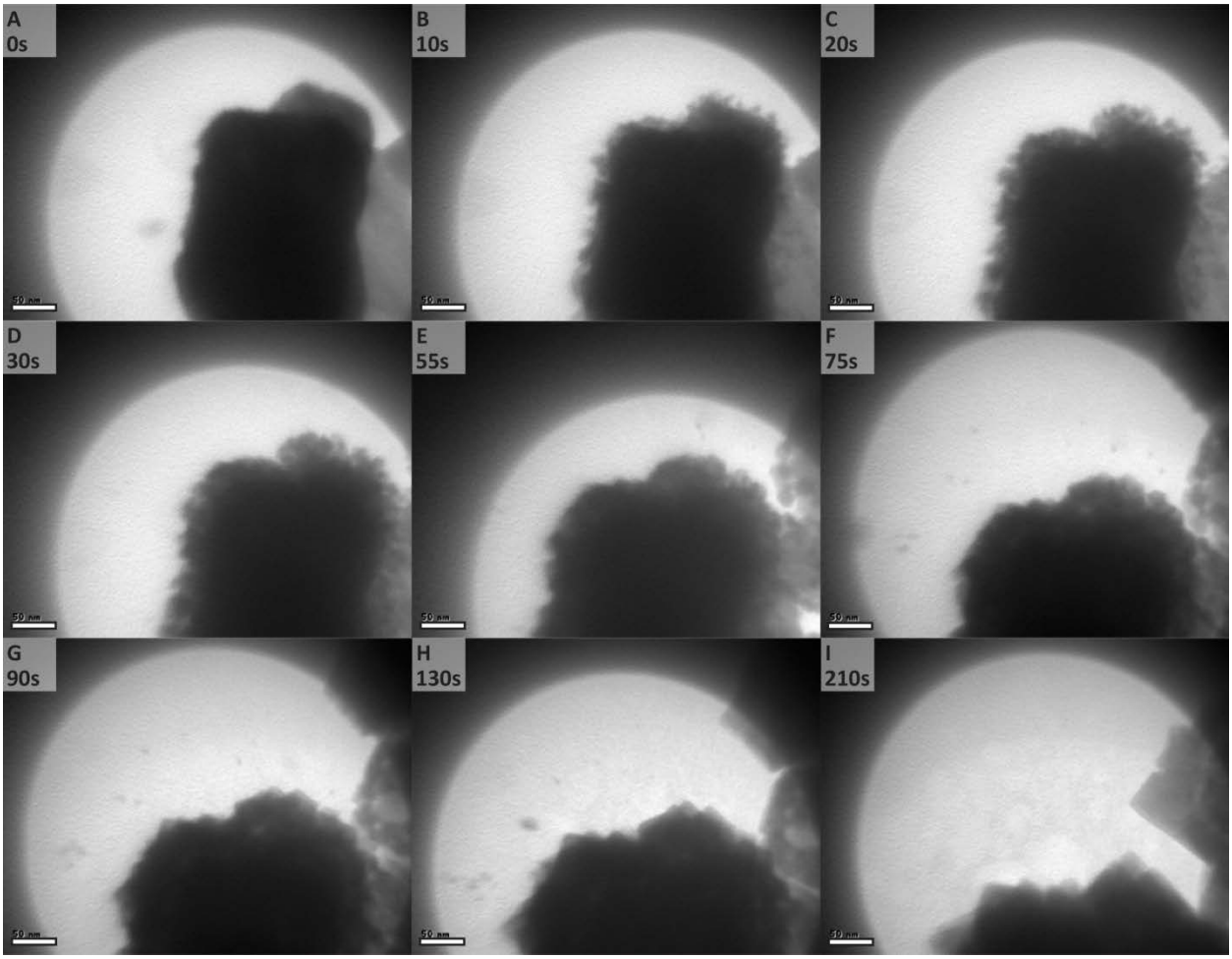

Figure 3.10 Image sequence of $CaCO_3$ nucleation, with 50nm scale bars. (A) The edge of the Au electrode before $CaCO_3$ deposition. (B-D) Formation of small particles, presumably ACC, with no discernible structure. (E-G) Merging of ACC and conversion into faceted crystals. (H-I) Continued growth into large, faceted crystals. Change in imaging area between panels is a combined result of sample drift and repositioning.

Later on in the growth process, $CaCO_3$ nanophase stability and ripening phenomena were also observed as shown in Figure 3.11. Following a period of growth, there were three relatively large crystals hundreds of nanometers in size, as well as a small aggregate of particles drifting in solution near the top of the image (Figure 3.11A). The lack of faceting and absence of growth suggests that this aggregate was a less stable phase of $CaCO_3$, such as ACC, vaterite or aragonite. While the large crystals grew at a steady rate, the size of the isolated aggregate remained unchanged. With time, it drifted towards one of the large growing crystals and attached to it (Figure 3.11B-C). Immediately upon attachment, it began to rapidly grow into a single faceted extension of the main crystal (Figure 3.11D-F), presumably due to its transformation into the more stable crystalline phase.

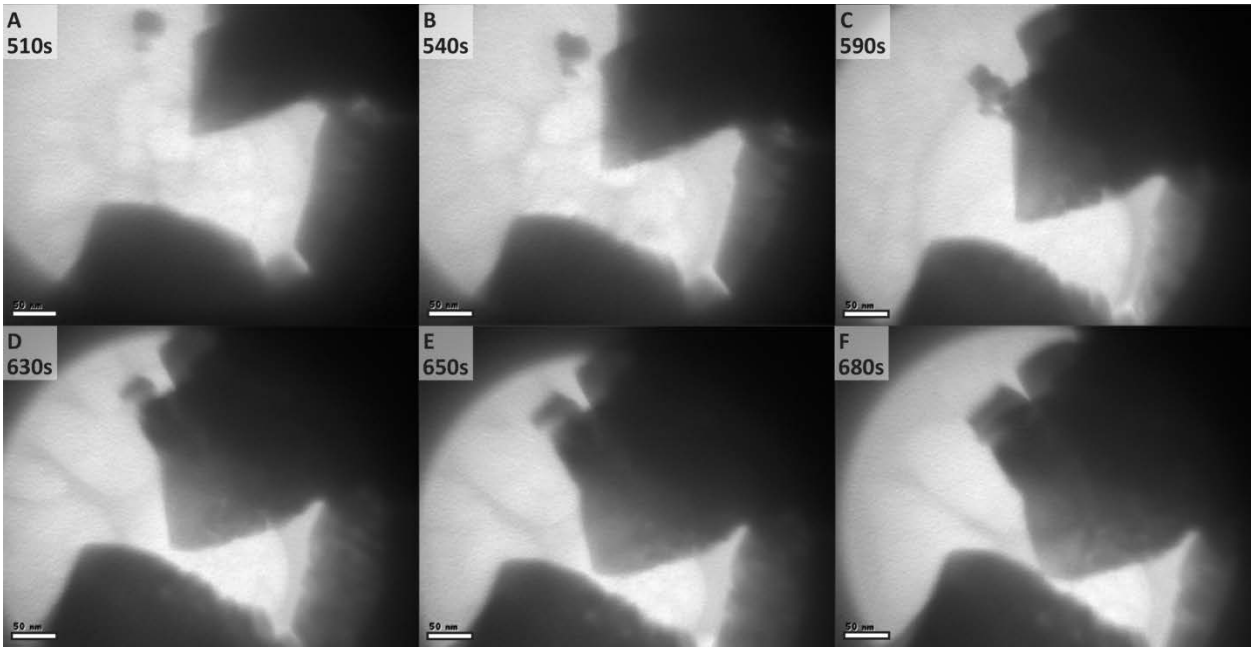

Figure 3.11 Image sequence of $CaCO_3$ coalescence and growth, with 50nm scale bars. (A) Three large crystals dominate imaging area, with detached aggregate in solution. (B-C) While crystals grow, aggregate maintains size and drifts towards nearby crystal. (D-F) Attachment of aggregate to crystal, followed by rapid growth and development of facets as aggregate transforms into crystal.

3.5 Discussion

The above examples highlight the utility of liquid phase TEM in better understanding phenomena at the onset of crystal formation. This relatively new experimental technique has opened a window to direct observations of nucleation pathways, growth mechanisms, and the interactions between the primary crystallizing material and additives. The ability to gather crystallographic information either through lattice resolution imaging or through electron diffraction further enhances the utility of this approach in understanding processes controlling materials formation. However, as should be expected given the relative youth of the liquid phase TEM field, there are numerous areas for future development, which will greatly enhance the technique's utility in quantitatively understanding a wider variety of experimental systems.

Despite the power of liquid cell TEM in providing direct evidence for specific mechanisms of crystallization from solution as well as dynamic information that can help to constrain important energetic parameters, the method has significant limitations. First, in order to get high resolution, the thickness of the liquid layer must be of order 100 nm or less. Unfortunately, particles in this geometry tend to interact with the surfaces of the liquid cell, dramatically reducing their mobility. Second, the small volume of liquid available for a reaction severely limits the extent to which a growth process can be followed.

These two issues are minor compared with the problems posed by beam effects. In nearly all experiments we have performed, the beam either triggers the reaction or impacts its rate. For

example, in the case of the experiments on gold nanoparticle nucleation, the solutions are stable for extended periods of time absent exposure to the beam; and in the experiments with iron oxyhydroxides, the initial solution contains nanorods of akaganeite. However, in the electron microscope these dissolve and are replaced by new particles of ferrihydrite. In the experiments for which $CaCO_3$ nucleation occurred on a gold electrode, again, nucleation did not occur until the cell was exposed to the beam.

A dramatic example of beam effects is given in Figure 3.12, which shows the growth of Au nanoparticles. As growth proceeds under continuous exposure, the particles suddenly begin to exhibit rapid growth with a dendritic morphology. Eventually, these dendrites, which have high curvature, collapse to form more compact, faceted crystals. These eventually aggregate and coalesce with one another. However, the entire process is instigated by the beam.

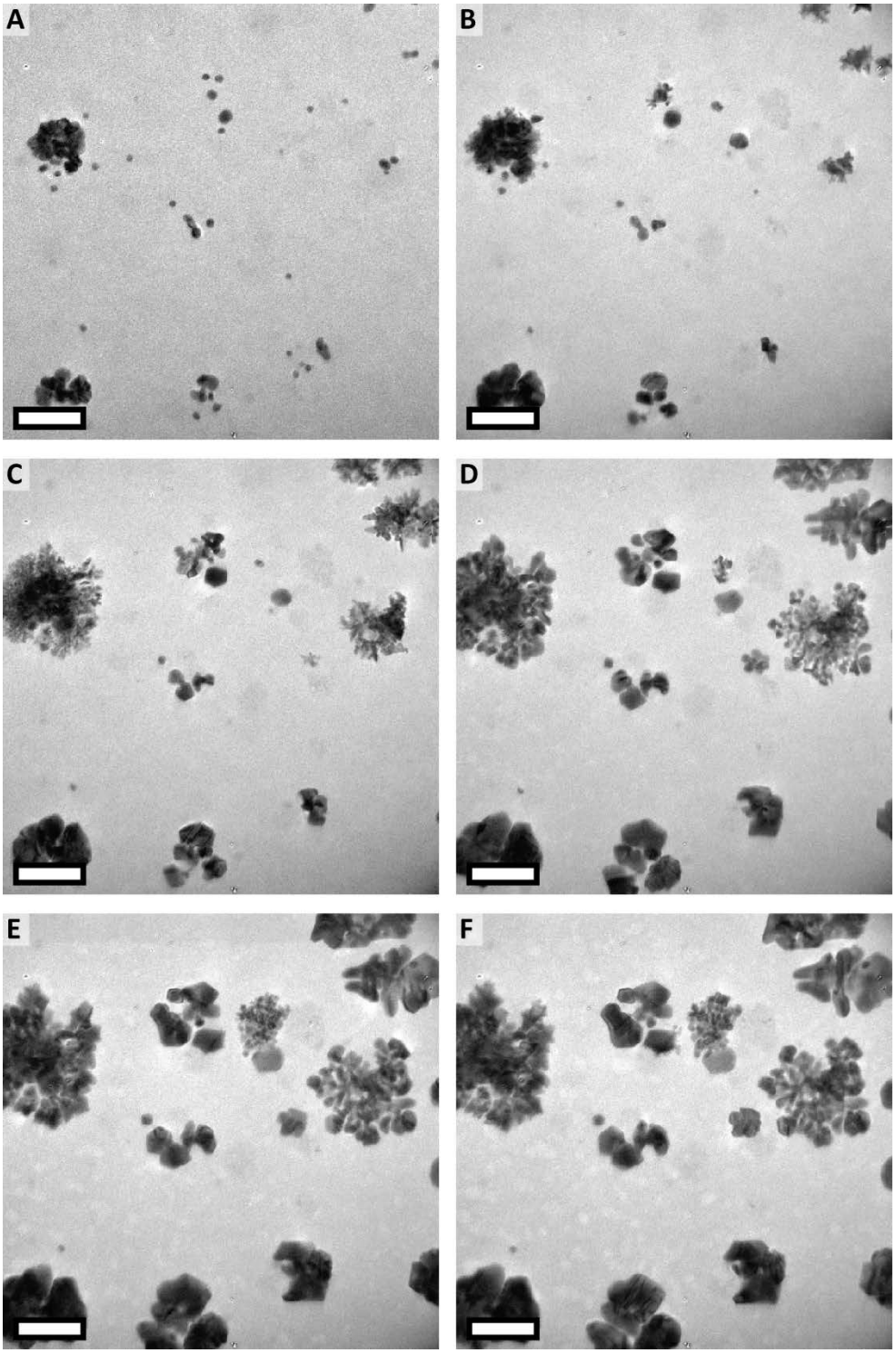

Figure 3.12 Onset of dendritic Au nanoparticle growth due to the electron beam. A–F: Sequence of liquid cell transmission electron microscopy (TEM) images showing appearance of dendritic growth front followed by dendrite collapse and particle coalescence. Times in seconds: (A) 0.0, (B) 15.4, (C) 28.8, (D) 52.4, (E) 77.0, and (F) 84.6. Scale bar is 100 nm.

How the electron beam affects reaction solutions is a significant question that has only recently begun to be addressed. A number of liquid phase TEM studies have utilized the electron beam to reduce solvated metal precursors to grow nanocrystals from solution, leaving open the question of what radiolytic products are additionally produced during interaction with the sample. Woehl *et al.* discussed the species that arise through the beam's interaction with the silicon nitride membranes and the liquid layer, and identified the aqueous electron as the reducing agent for metal precursors [32]. More recent efforts have gone toward building a predictive model of each of the species produced through electron irradiation, their spatial concentrations relative to the electron beam, lifetimes, and effect on the liquid's pH [33, 34]. Extending this model from water, for which it was originally developed, to complex solutions with many dissolved species will allow for more quantitative studies of crystallization processes in the future.

The above model predicts that pH changes of potentially significant amounts may be induced in the sample solution as a result of imaging in the TEM. At present there are no in situ diagnostics to measure such changes in the experimental conditions. In order to conduct a quantitative analysis of the energetics of crystallization, it is crucial to know solution parameters such as pH and temperature. Future developments of on-device probes that allow in situ measurement of — and control over — these and other parameters will broaden the utility of liquid phase TEM.

3.6 Conclusions

The results presented here suggest that liquid cell TEM will become a powerful tool for addressing outstanding scientific questions that have arisen in recent years concerning the mechanisms underlying nucleation and growth of crystals from electrolyte solutions. Results on nucleation of gold nanoparticles show that the process exhibits the characteristic feature of classical nucleation, while the data on crystal growth by nanoparticle aggregation demonstrate that no single pathway or controlling mechanism is at work. While some systems may exhibit true OA, others appear to involve aggregation of precursor phases that may be initially misaligned or even amorphous and thus require a post-aggregation crystallization or recrystallization step. Due to the importance of nucleation and growth processes in geochemical, biological, and synthetic systems, the information obtained using liquid cell TEM has the potential to impact a wide range of fields. However, the full impact awaits development of well-tested low dose imaging techniques as well as liquid cells that have a reproducible thickness and are instrumented to provide full knowledge of solution conditions including pH, temperature, and ion concentrations.

3.7 References

1. Q. Hu, M. H. Nielsen, C. L. Freeman, L. M. Hamm, J. Tao, J. R. I. Lee, T. Y. J. Han, U. Becker, J. H. Harding, P. M. Dove, J. J. De Yoreo, The thermodynamics of calcite nucleation at organic interfaces: Classical vs. non-classical pathways. *Faraday Discuss.* **159**, 509-523 (2012). doi:10.1039/c2fd20124k

2. A. Verch, I. E. G. Morrison, R. van de Locht, R. Kroger, In situ electron microscopy studies of calcium carbonate precipitation from aqueous solution with and without organic additives. *Journal of Structural Biology* **183**, 270-277 (2013). doi:10.1016/j.jsb.2013.05.017

3. J. Rieger, J. Thieme, C. Schmidt, Study of precipitation reactions by x-ray microscopy: CaCO3 precipitation and the effect of polycarboxylates. *Langmuir* **16**, 8300-8305 (2000). doi:10.1021/la0004193

4. T. Ando, N. Kodera, E. Takai, D. Maruyama, K. Saito, A. Toda, A high-speed atomic force microscope for studying biological macromolecules. *Proceedings of the National Academy of Sciences* **98**, 12468-12472 (2001). doi:10.1073/pnas.211400898

5. P. J. M. Smeets, K. R. Cho, R. G. E. Kempen, N. A. J. M. Sommerdijk, J. J. De Yoreo, Calcium carbonate nucleation driven by ion binding in a biomimetic matrix revealed by in situ electron microscopy. *Nat. Mater.* **14**, 394-399 (2015). doi:10.1038/nmat4193

6. C. C. Tester, R. E. Brock, C. H. Wu, M. R. Krejci, S. Weigand, D. Joester, In vitro synthesis and stabilization of amorphous calcium carbonate (ACC) nanoparticles within liposomes. *Crystengcomm* **13**, 3975-3978 (2011). doi:10.1039/c1ce05153a

7. P. A. Fang, J. F. Conway, H. C. Margolis, J. P. Simmer, E. Beniash, Hierarchical self-assembly of amelogenin and the regulation of biomineralization at the nanoscale. *Proceedings of the National Academy of Sciences of the United States of America* **108**, 14097-14102 (2011). doi:10.1073/pnas.1106228108

8. F. Nudelman, K. Pieterse, A. George, P. H. H. Bomans, H. Friedrich, L. J. Brylka, P. A. J. Hilbers, G. de With, N. Sommerdijk, The role of collagen in bone apatite formation in the presence of hydroxyapatite nucleation inhibitors. *Nat. Mater.* **9**, 1004-1009 (2010). doi:10.1038/nmat2875

9. A. J. Giuffre, L. M. Hamm, N. Han, J. J. De Yoreo, P. M. Dove, polysaccharide chemistry regulates kinetics of calcite nucleation through competition of interfacial energies. *Proceedings of the National Academy of Sciences* **110**, 9261-9266 (2013). doi:10.1073/pnas.1222162110

10. L. M. Hamm, A. J. Giuffre, N. Han, J. Tao, D. Wang, J. J. De Yoreo, P. M. Dove, Reconciling disparate views of template-directed nucleation through measurement of calcite nucleation kinetics and binding energies. *Proceedings of the National Academy of Sciences* **111**, 1304-1309 (2014). doi:10.1073/pnas.1312369111

11. M. J. Williamson, R. M. Tromp, P. M. Vereecken, R. Hull, F. M. Ross, Dynamic microscopy of nanoscale cluster growth at the solid-liquid interface. *Nat. Mater.* **2**, 532-536 (2003). doi:10.1038/nmat944

12. A. Radisic, F. M. Ross, P. C. Searson, In situ study of the growth kinetics of individual island electrodeposition of copper. *J. Phys. Chem. B* **110**, 7862-7868 (2006). doi:10.1021/jp057549a

13. A. Radisic, P. M. Vereecken, J. B. Hannon, P. C. Searson, F. M. Ross, Quantifying electrochemical nucleation and growth of nanoscale clusters using real-time kinetic data. *Nano Letters* **6**, 238-242 (2006). doi:10.1021/nl052175i

14. A. Radisic, P. M. Vereecken, P. C. Searson, F. M. Ross, The morphology and nucleation kinetics of copper islands during electrodeposition. *Surf. Sci.* **600**, 1817-1826 (2006). doi:10.1016/j.susc.2006.02.025

15. C. Gabrielli, G. Maurin, G. Poindessous, R. Rosset, Nucleation and growth of calcium carbonate by an electrochemical scaling process. *J. Cryst. Growth* **200**, 236-250 (1999). doi:10.1016/S0022-0248(98)01261-5

16. H. Gronbeck, A. Curioni, W. Andreoni, Thiols and disulfides on the Au(111) surface: The headgroup-gold interaction. *J. Am. Chem. Soc.* **122**, 3839-3842 (2000). doi:10.1021/ja993622x

17. C. Deslouis, I. Frateur, G. Maurin, B. Tribollet, Interfacial pH measurement during the reduction of dissolved oxygen in a submerged impinging jet cell. *Journal of Applied Electrochemistry* **27**, 482-492 (1997). doi:10.1023/A:1018430224622

18. M. M. Tlili, M. Benamor, C. Gabrielli, H. Perrot, B. Tribollet, Influence of the interfacial pH on electrochemical CaCO3 precipitation. *Journal of the Electrochemical Society* **150**, C765-C771 (2003). doi:10.1149/1.1613294

19. Q. Chen, J. M. Smith, J. Park, K. Kim, D. Ho, H. I. Rasool, A. Zettl, A. P. Alivisatos, 3D Motion of DNA-Au nanoconjugates in graphene liquid cell electron microscopy. *Nano Letters* **13**, 4556-4561 (2013). doi:10.1021/nl402694n

20. K. L. Jungjohann, S. Bliznakov, P. W. Sutter, E. A. Stach, E. A. Sutter, In situ liquid cell electron microscopy of the solution growth of Au-Pd core-shell nanostructures. *Nano Letters* **13**, 2964-2970 (2013). doi:10.1021/nl4014277

21. J. J. De Yoreo, P. G. Vekilov, in *Biomineralization*, P. M. Dove, J. J. DeYoreo, S. Weiner, Eds. (Mineralogical Soc America, Washington, 2003), vol. 54, pp. 57-93.

22. J. J. De Yoreo, G. A. Waychunas, Y. S. Jun, A. Fernandez-Martinez, in *Geochemistry of Geologic Co2 Sequestration*, D. J. DePaolo, D. R. Cole, A. Navrotsky, I. C. Bourg, Eds. (Mineralogical Soc Amer, Chantilly, 2013), vol. 77, pp. 229-257.

23. D. S. Li, M. H. Nielsen, J. R. I. Lee, C. Frandsen, J. F. Banfield, J. J. De Yoreo, Direction-specific interactions control crystal growth by oriented attachment. *Science* **336**, 1014-1018 (2012). doi:10.1126/science.1219643

24. H. Z. Zhang, J. F. Banfield, Energy calculations predict nanoparticle attachment orientations and asymmetric crystal formation. *J. Phys. Chem. Lett.* **3**, 2882-2886 (2012). doi:10.1021/jz301161j

25. R. L. Joesten, *Kinetics of coarsening and diffusion-controlled material growth*. D. M. Kerrick, Ed., Contact Metamorphism (Mineralogical Soc America, Washington, 1991), vol. 26, pp. 507-582.

26. H. Z. Zhang, J. F. Banfield, Interatomic coulombic interactions as the driving force for oriented attachment. *Crystengcomm* **16**, 1568-1578 (2014). doi:10.1039/c3ce41929k

27. D. Quigley, C. L. Freeman, J. H. Harding, P. M. Rodger, Sampling the structure of calcium carbonate nanoparticles with metadynamics. *Journal of Chemical Physics* **134**, 044703 (2011). doi:10.1063/1.3530288

28. P. Raiteri, J. D. Gale, Water is the key to nonclassical nucleation of amorphous calcium carbonate. *J. Am. Chem. Soc.* **132**, 17623-17634 (2011). doi:10.1021/ja108508k

29. M. Ocana, M. P. Morales, C. J. Serna, The growth mechanism of alpha-Fe2O3 ellipsoidal particles in solution. *Journal of Colloid and Interface Science* **171**, 85-91 (1995). doi:10.1006/jcis.1995.1153

30. C. Frandsen, B. A. Legg, L. R. Comolli, H. Z. Zhang, B. Gilbert, E. Johnson, J. F. Banfield, Aggregation-induced growth and transformation of beta-FeOOH nanorods to micron-sized alpha-Fe2O3 spindles. *Crystengcomm* **16**, 1451-1458 (2014). doi:10.1039/c3ce40983j

31. H. M. Zheng, R. K. Smith, Y. W. Jun, C. Kisielowski, U. Dahmen, A. P. Alivisatos, Observation of single colloidal platinum nanocrystal growth trajectories. *Science* **324**, 1309-1312 (2009). doi:10.1126/science.1172104

32. T. J. Woehl, J. E. Evans, L. Arslan, W. D. Ristenpart, N. D. Browning, Direct in situ determination of the mechanisms controlling nanoparticle nucleation and growth. *ACS Nano* **6**, 8599-8610 (2012). doi:10.1021/nn303371y

33. J. M. Grogan, N. M. Schneider, F. M. Ross, H. H. Bau, Bubble and pattern formation in liquid induced by an electron beam. *Nano Letters* **14**, 359-364 (2014). doi:10.1021/nl404169a

34. N. M. Schneider, M. M. Norton, B. J. Mendel, J. M. Grogan, F. M. Ross, H. H. Bau, Electron-water interactions and implications for liquid cell electron microscopy. *Journal of Physical Chemistry C* **118**, 22373-22382 (2014). doi:10.1021/jp507400n

Chapter 4

In Situ TEM Imaging of $CaCO_3$ Nucleation Reveals Coexistence of Direct and Indirect Pathways

The liquid phase TEM platform described in the previous chapter is limited by the static volume of the associated liquid cell. During the course of this dissertation research, a prototype of a continuous flow liquid TEM stage incorporating a microfluidic system of two inlet lines was made available for testing. This chapter describes the use of this stage to explore $CaCO_3$ nucleation by flowing in and mixing reagent solutions. It is demonstrated in this chapter that multiple nucleation pathways are simultaneously operative, including formation both directly from solution and indirectly through transformation of amorphous and crystalline precursors. However, an amorphous-to-calcite transformation was not observed. The behavior of amorphous calcium carbonate upon dissolution suggests that it encompasses a spectrum of structures, including liquids and solids. These observations of competing direct and indirect pathways are consistent with classical predictions, whereas the behavior of amorphous particles hints at an underlying commonality among recently proposed precursor-based mechanisms.

4.1 Introduction

Nucleation is a key step in the crystallization process, representing the initial transformation of a disordered phase into an ordered one. It is also the most difficult part of the process to observe because it happens on very short time and length scales. In the case of electrolyte solutions, there is an open debate as to whether classical nucleation theory (CNT), as initially developed by Gibbs [1], is a suitable framework within which to describe the process, or whether nonclassical elements such as dense liquid phases [2–4] or (meta)stable clusters [5] play important roles. Furthermore, uncertainty exists as to whether a final, stable phase can nucleate directly from solution or whether it forms through a multistep, multiphase evolution [6, 7]. In the case of multistep nucleation pathways, whether transformation from one phase to another occurs through nucleation of the more stable phase within the existing precursor or through dissolution of the original phase and re-precipitation of the secondary phase is unclear [8, 9]. Although many studies have provided snapshots of the nucleation process [8] or followed the ensemble evolution of phases in solution [9], and simulations have produced predictions for certain solution conditions [4, 10], in situ observations that follow the process from start to finish have been lacking.

The advent of liquid cell transmission electron microscopy (TEM) [11] permits imaging with nanometer-scale spatial resolution in time increments of fractions of a second. A dual-inlet flow stage was used for in situ observations of $CaCO_3$ nucleation pathways over a range of solution conditions. The observations reported in this chapter elucidate the existence of a range of nucleation pathways occurring under identical or similar solution conditions, often simultaneously within a single experiment.

4.2 Experimental Methods

4.2.1 TEM Liquid Stage and Cell

A dual inlet liquid flow transmission electron microscopy (TEM) stage and liquid cell chips (Hummingbird Scientific) were used as received. The stage has two plumbed inlets that terminate within a few centimeters of the liquid cell, in principle allowing the liquid streams to mix and flow through and around the liquid cell. The liquid volume is isolated from the vacuum of the TEM column by Viton o-rings (Figure 4.1). A single outlet transports the fluid cell effluent to a collection vial external to the stage. The fluid cell consists of two square 4 mm^2 silicon chips with 50 nm thick silicon nitride membranes deposited on each face. One nitride membrane and the silicon are etched away on each chip, producing a suspended nitride membrane that serves as a window transparent to high energy electrons. The maximum imaging area in a cell is 50×200 μm^2, based on perfect chip alignment in the stage. Imaging was predominantly conducted near the window edges to mitigate the thickness increase due to window flex, although no phenomenological difference across the imaging area was observed. One of the chips has an oxide layer 250-500 nm thick deposited on the internal face to create a rectangular flow channel between the assembled cell. In principle this allows liquid(s) from the inlets to flow through the liquid cell from one side to the other, passing across the windows. Liquid layer thicknesses in the imaging area vary widely from cell to cell, in part due to flex of the nitride membranes under the influences of vacuum and liquid flow. During some experiments the thickness of the fluid layer varied over the course of an experiment, becoming significantly thinner over short time periods, perhaps due to water vaporization by radiolysis or the introduction of an air bubble.

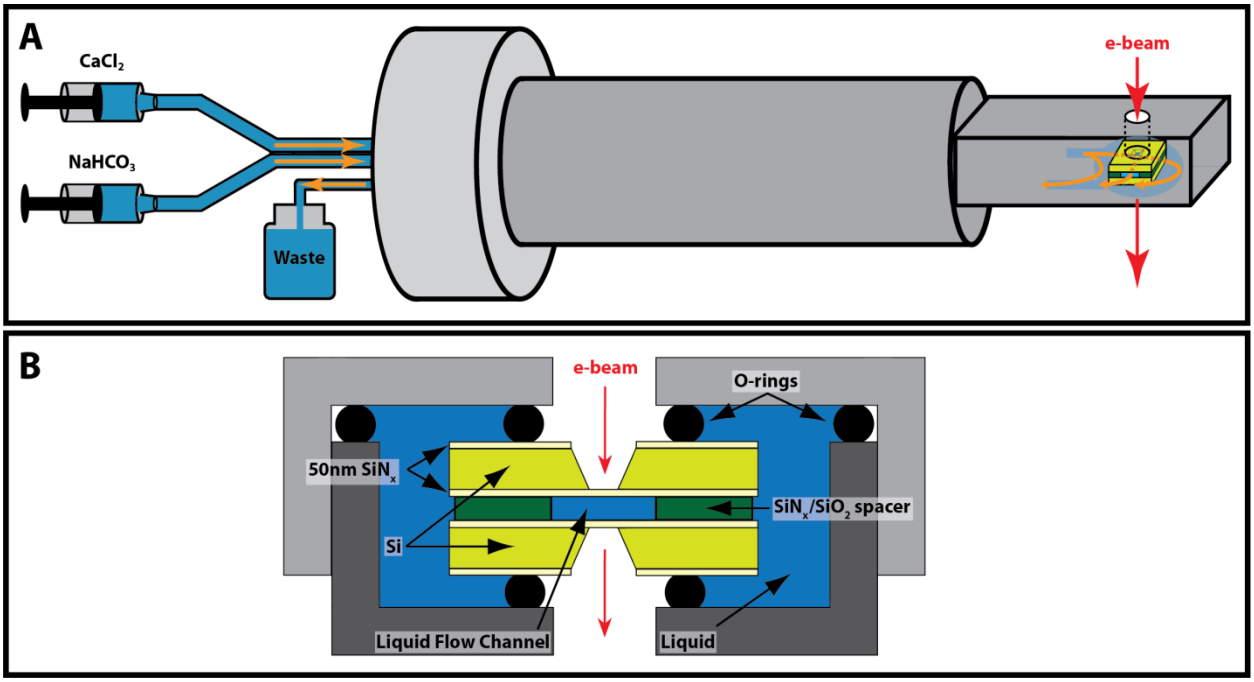

Figure 4.1 Schematics of experimental set-up. Overview of the liquid stage set-up (A) shows separate inlets for the two reagent solutions, which mix shortly before reaching the liquid cell. Proprietary stage details regarding inlet mixing not shown. The combined liquid stream flows through the flow channel of the cell as well as around the external sides of the cell, and exits the stage through a single outlet tube that empties into a waste container. Side-view schematic of the liquid cell on the stage (B) shows liquid in the cell's flow channel, as well as external to the cell. From this perspective, liquid would flow into/out-of the plane of the image as it passes through the cell. O-rings keep the liquid separated from the vacuum of the TEM column.

4.2.2 Sample Preparation

Solutions of $NaHCO_3$ (99.998%, Alfa Aesar) and $CaCl_2$ (99.99% Alfa Aesar) with concentrations ranging between 10-100 mM were prepared by dissolving the salts in Milli-Q water (Millipore Corporation), and used to fill gas-tight syringes (Hamilton) that were placed on separate syringe pumps and connected to the tubing system of the dual inlet liquid flow TEM stage. One inlet was filled with the $NaHCO_3$ solution, while the other inlet was filled with Milli-Q water to prevent premature nucleation. The fluid cell chips were plasma cleaned in a Plasma Cleaner/Sterilizer PDC-32G (Harrick Plasma) for around one minute prior to use, by bleeding in 200-400 mTorr ambient atmosphere. The chips were pre-wet with 0.5-1.0 μL of $NaHCO_3$ solution, and the stage was closed and sealed for vacuum compatibility. During this assembly process, salt deposits were occasionally created on the exterior of the chips and were visible as fixed features during imaging. $NaHCO_3$ was immediately pumped through the cell to circulate solution through the stage plumbing and the stage was pumped down in a "testing garage" provided with the stage to check the vacuum seal. Post-test, the garage was brought back to atmospheric pressure, and the stage was transferred immediately to the electron microscope. The

$NaHCO_3$ flow was interrupted during transfer of the stage, but restarted within a minute and continued during pump-down and alignment of the microscope.

4.2.3 Reaction Conditions

Experiments were either conducted by switching the flow from $NaHCO_3$ to $CaCl_2$ and flowing in this single reactant (approximated, so as to prevent potential mineralization in the $CaCl_2$-filled tube due to diffusion, by the 10:0.2 (μL/min) $CaCl_2$:$NaHCO_3$ flow ratio in Appendix III, Tables A1 and A2), or by simultaneously flowing in both reactants at variable ratios of flow rates from 5:5 to 9:1 (μL/min), keeping the total flow rate constant. While it is clear that the flow profile of the two inlets through the stage, after exiting the tubing, and into or around the liquid cell is non-trivial, the linear growth rates indicate steady state growth conditions suggesting that some portion of fluid flow does pass through the cell. Exactly in which manner the two fluid streams flow, at any given condition, and where and to what extent mixing occurs are parameters that unfortunately remain unclear. As such, it is impossible to know the precise conditions of the solutions inside the liquid cell. Supersaturations and pH were calculated using Visual MINTEQ (Jon Petter Gustafsson) [12], assuming complete mixing of the two reagent solutions, and are reported in Table A1 (Appendix II). It is clear from our results that these calculated values, at least in some cases, do not reflect the solution conditions in the imaged area. For example, formation and growth of amorphous calcium carbonate (ACC) and vaterite at {20:20/10:0.2} was observed, where the calculations show the mixed solution to be undersaturated with respect to those phases. Experiments were primarily run with equimolar concentrations of the two reactant solutions, spanning the range from 10 mM to 100 mM, flowing through the stage at a total flow rate at or near 10 μL min-1, with the relative flow ratio of Ca^{2+}:CO_3^{2-} varying between 50:1 and 1:1. Table A2 (Appendix II) shows the various phases observed at each experimental condition. In agreement with reports from other $CaCO_3$ crystallization studies that utilized mixing of reagent solutions to create supersaturation, no ACC was produced with reagent solutions with concentrations ≤ 10 mM. Some experiments were run by flowing only 30 mM $CaCl_2$ solution to mix with and displace 100 mM $NaHCO_3$ solution used to pre-fill the liquid cell. Liquid cells that were used for multiple experiments were thoroughly rinsed by extensively flushing all of the tubing between experiments with dilute HCl (pH ≈ 4) and Milli-Q water.

4.2.4 Electron Microscopy

Electron microscopy was conducted using the aforementioned Hummingbird liquid flow stage in a field emission JEOL JEM2100-F (JEOL Ltd.) operated at 200 kV. Data was collected using the VirtualDub software (Avery Lee) to collect sequential, cropped screenshots from Digital Micrograph (Gatan Inc.) as .avi files. Image acquisition times were 0.1 – 0.2 s, and the video frame size was 1001 ± 1 × 666 ± 1 pixels. Precise measurements of electron dose are difficult to obtain, as a significant variation in liquid layer thickness can convolute measurements of electron density transmitted through the sample to detectors sitting below the sample. Measurements were made with a blank stage under representative imaging conditions, as well as with the liquid stage and cell for comparison. There was found to be roughly a twenty percent

reduction in measured value in the presence of fluid and used that as a basis for estimating the electron dose from values measured during experiments. While it is not expected that the actual values were thus determined precisely, they serve as reasonable estimates. Using this approach a conservative estimate of the electron dose at the start of experiments would be $5 \pm 3 \times 10^2$ electrons $nm^{-2}s^{-1}$.

Video data was recorded beginning at the onset of reagent flow. In a typical experiment 3-5 minutes elapsed before the onset of observable nucleation and growth processes. The times reported in the figures and text are based on t = 0 corresponding to the start of each video clip, and have no relationship to the beginning of the experiment as defined by the onset of reagent flow.

4.3 Results

A range of flow rates, set independently for the two reagents (Appendix II) were used to introduce $CaCl_2$ and $NaHCO_3$ solutions of varying concentrations into the flow cell. In some experiments, supersaturations increased initially but eventually decreased until undersaturated so that dissolution was also observed. Nucleation of both metastable and stable phases was recorded, including amorphous calcium carbonate (ACC), vaterite, aragonite, and calcite, typically exhibiting morphologies common for these phases. All nucleation events occurred on the top or bottom membrane of the fluid cell. The thickness of the fluid layer varied and sometimes thinned substantially during an experiment, facilitating collection of diffraction data for unambiguous phase identification. However, collection of diffraction data was not always possible, either because phase transformations took place while operating in imaging mode or because the solution layer thickness produced multiple scattering events that degraded the diffraction signal beyond use.

Amorphous calcium carbonate particles nucleated (Figure 4.2, A and B) and grew to diameters of up to hundreds of nanometers (Figure 4.2, C and D). Diffraction data confirmed the amorphous nature of the particles (Figure 4.2D, inset). Similarly for vaterite, nucleation (Figure 4.2, E and F) was followed by extensive growth (Figure 4.2G); some crystals merged to form larger crystals (Figure 4.2H) with visible texture (Figure 4.2I). In some cases, at later stages of growth the growing outer edge exhibited a layered structure while the interior of the growing platelet dissolved away (Figure 4.2J). The diffraction pattern (Figure 4.2J, inset) identified the phase as vaterite.

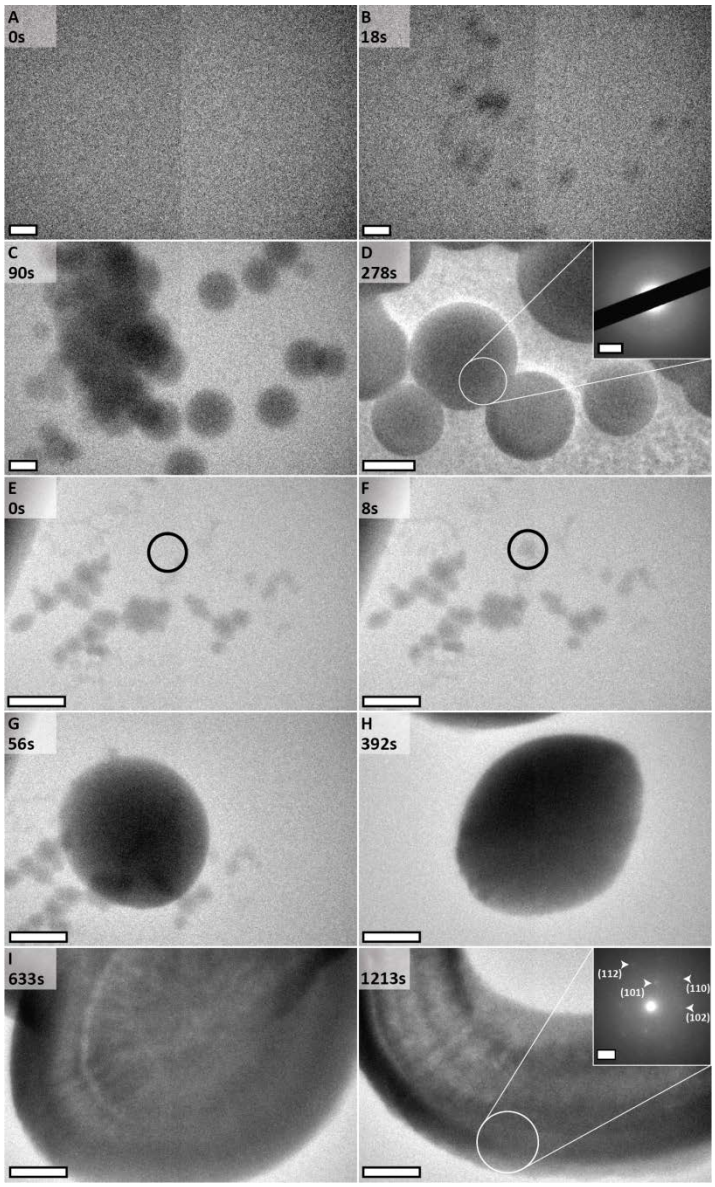

Figure 4.2 Direct formation of ACC and vaterite. Image sequence shows the fluid cell before nucleation (A) and during nucleation and growth of ACC (B to D). Diffraction analysis [inset to (D)], performed when the fluid layer thinned (see supplementary materials), confirms the amorphous nature of the particles. Image sequence follows vaterite formation and growth (E to J). Gray spots already present (E) are salt deposits that formed on the outer surface of the liquid cell window during cell assembly. In (E) and (F), the nucleation site of a vaterite particle is circled for clarity. The particle grows (G), merges with a second particle (H), and exhibits layering at the growth front and dissolution in the center (I and J). Diffraction analysis [inset to (J)] identifies the material as vaterite. Scale bars are 500 nm in (A) to (J) and 2 nm^{-1} in the insets to (D) and (J). Solution conditions—designated by $[CaCl_2]$:$[NaHCO_3]$/R($CaCl_2$):R($NaHCO_3$) in all figure legends with concentrations in millimolar and flow rates R in microliters per minute—are 50:50/10:0.2 for (A) to (D) and 40:40/9:1 for (E) to (J).

Multistep nucleation pathways starting with ACC (Figure 4.3) was also observed. ACC particles formed and grew to sizes ranging from hundreds of nanometers to micrometers (Figure 4.3, A and E) before suddenly transforming to the aragonite "sheaf-of-wheat" morphology (Figure 4.3, C and D) or vaterite (Figure 4.3, F to H). Typically, the ACC particle began to shrink just before the appearance of a secondary phase (Figure 4.3, B and F) on, or possibly just below, the surface of the original particle. This shrinkage perhaps indicates either the expulsion of water from the amorphous particle or a sudden decrease in concentration leading to partial dissolution. This secondary phase grew rapidly, consuming the original amorphous particle (Figure 4.3, C, D, G, and H). The two phases maintained constant physical contact throughout this transformation process. Because the surrounding medium is supersaturated with respect to the secondary phase, growth presumably also involves monomer addition from solution.

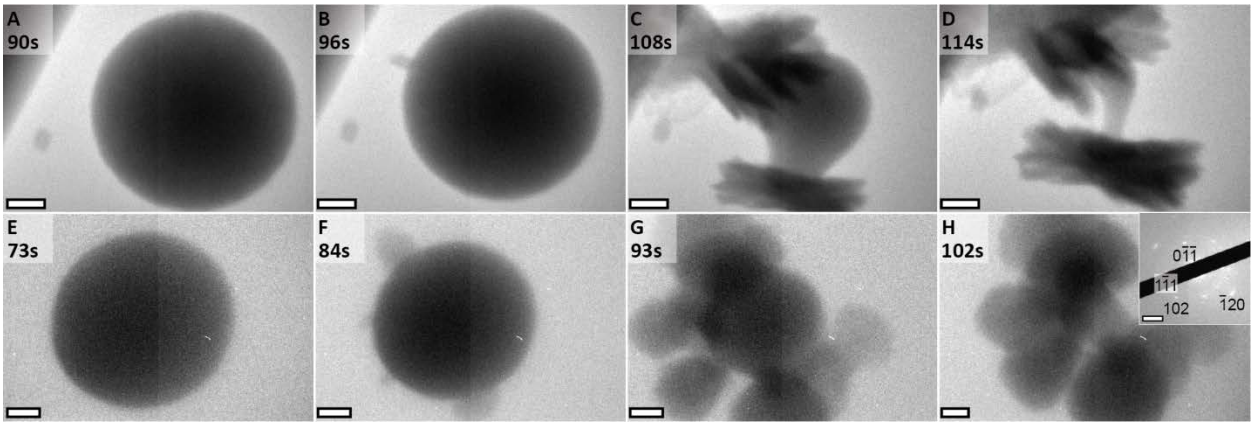

Figure 4.3 Direct transformation of ACC to crystalline phases. Image sequence shows a previously nucleated ACC particle (A), with the secondarily nucleated crystalline phase forming on or in the amorphous particle (B). The secondary phase, exhibiting typical aragonitic sheaf-of-wheat morphology, grows at the expense of the ACC, with the two phases maintaining physical contact during the entire transformation (C and D). Image sequence shows a previously nucleated ACC particle (E), with secondarily nucleated vaterite plates forming on or in the amorphous particle (F).These plates grow at the expense of the ACC (G and H), in the same manner as above (C and D). Diffraction from the resulting plates identifies them as vaterite [inset to (H)]. Scale bars are 500 nm in (A) to (H) and 2 nm^{-1} in the inset to (H). Solution conditions are 30:100/10:0.2 for (A) to (H).

These two examples demonstrate the occurrence of multistep pathways of $CaCO_3$ crystal nucleation by which a metastable, amorphous precursor appears first and then transforms into a more energetically favorable crystalline phase through a direct, physical connection between the growing and shrinking phases. These multistep pathways contrast with direct pathways in which a crystalline phase nucleates from solution, either in the absence of ACC or independently of any amorphous particles that may have already formed. In this latter case, which is well documented [9, 13–15], the nucleation of the crystalline phase is followed by dissolution of preexisting amorphous particles and reprecipitation onto the crystalline phase, as inferred from in situ optical [13, 14] and x-ray studies [9]. However, among the hundreds of experiments conducted, transformation of ACC into calcite (the most stable phase of $CaCO_3$) was never observed.

Concurrent nucleation of multiple phases was additionally detected. For example, direct nucleation of calcite rhombohedra (Figure 4.4, A to D) was observed alongside the formation of a (hemi-)spherical particle that, based on morphology, was either ACC or vaterite. Numerous optical studies have shown that ACC dissolves in the presence of calcite [13–15]. Consequently, although the particle lacked any visible internal structure, as was typically seen in vaterite (Figs. 4.3, H to J, and 4.4, H and I), it is unlikely to be ACC.

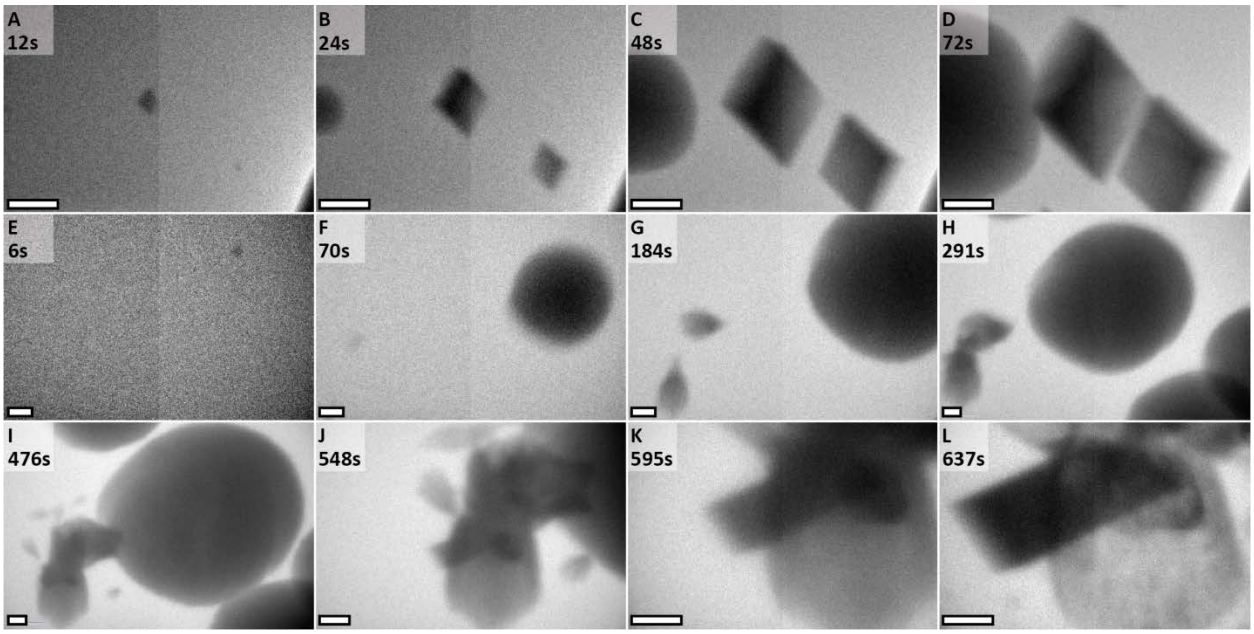

Figure 4.4 Concurrent formation of multiple phases. Image sequence shows simultaneous nucleation and growth of calcite crystals and either ACC or vaterite (A to D). The nitride window edge is visible at the bottom right corner of each panel. Image sequence shows direct nucleation of vaterite (E) and aragonite (F) and subsequent growth (G and H). The formation of calcite occurs on aragonite (I), followed by calcite growth and concomitant dissolution of the aragonitic bundle (J to L). Scale bars are 500 nm in all panels. Solution conditions are 30:30/8:2 for (A) to (D) and 50:50/10:0.2 for (E) to (H).

Nucleation of multiple phases, followed by transformation to secondary phases, was also observed in a single experiment (Figure 4.4, E to L). For example, a crystal with vateritic morphology first formed (Figure 4.4, E to I) and continued to grow as bundles with aragonitic morphology formed in the vicinity and merged into larger aggregates (Figure 4.4, F to J). A calcite rhombohedron then nucleated in apparent contact with the aragonitic bundle (Figure 4.4I) and grew throughout the rest of the experiment (Figure 4.4, J to L) as the aragonitic bundle dissolved (Figure 4.4, K and L). Diffraction information to unequivocally assign phases was unable to be collected in this experiment, leading to some ambiguity. Furthermore, because the image is a two-dimensional (2D) projection of a 3D volume, there is some uncertainty as to the precise location of the calcite nucleus relative to the surface of the bundle.

Contrary to expectations, on the time scale of our experiments, ACC nucleation occurred only when the solution was exposed to the electron beam under sufficiently high solution

concentrations. Moreover, varying the electron dose accelerated, delayed, or prevented its formation. By contrast, none of the crystalline phases showed such a relation to the electron beam; crystals were regularly found far from areas exposed to the beam.

Growth rates for ACC (Figure 4.5A), calcite (Figure 4.5B), and vaterite (Figure 4.5C) were measured in 14 experiments, tracking observations of both single and multiple particles. All phases grew linearly, indicating that post nucleation growth occurred under steady-state solution conditions and was controlled by surface kinetics rather than diffusive transport [16]. Although some growth curves exhibited single linear trends, others showed two distinct linear regions. This change in slope marked a drop in the growth rate and, therefore, supersaturation, suggesting a reduced rate of solute input to the cell, perhaps due to $CaCO_3$ nucleation near the cell inlet.

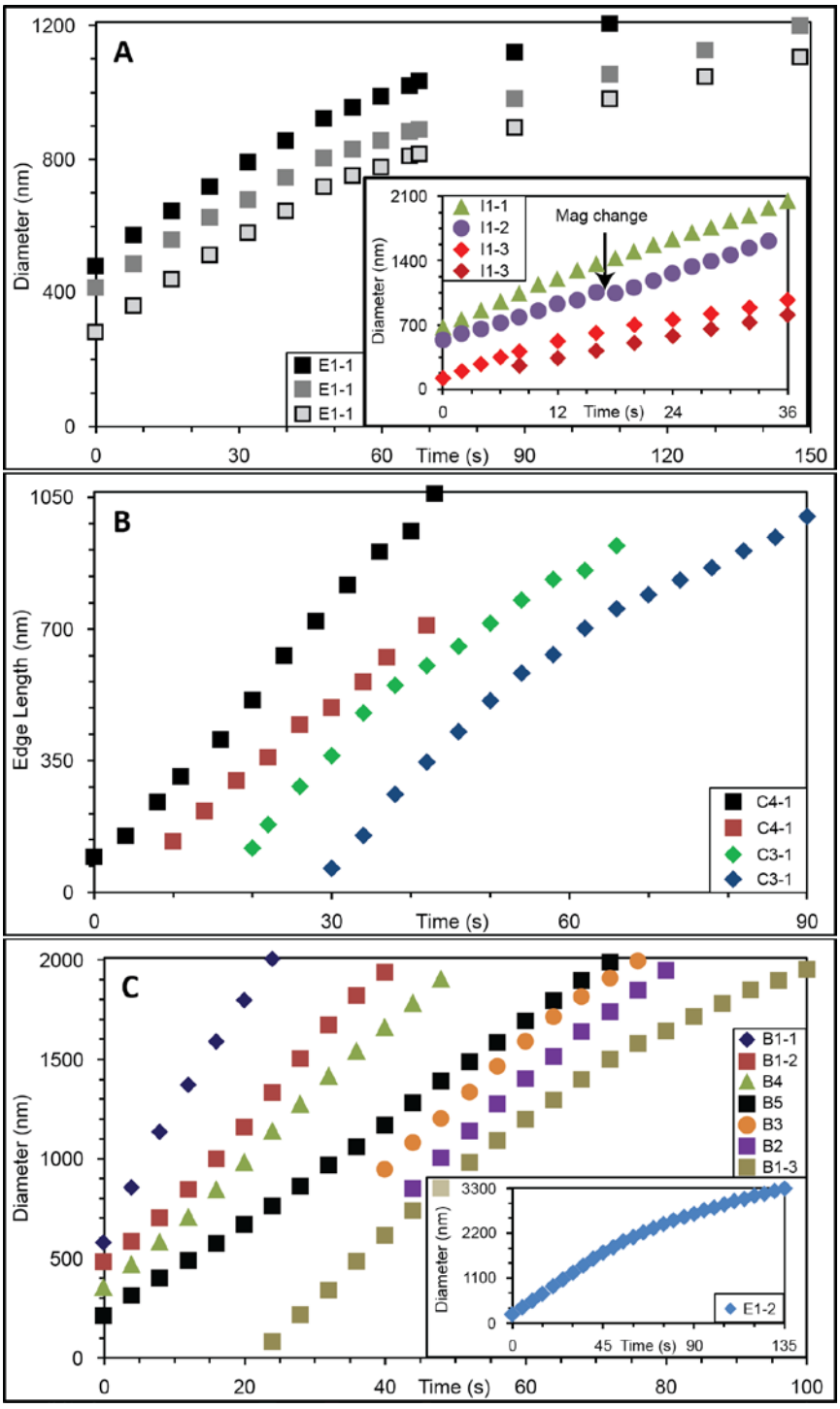

Figure 4.5 Post-nucleation growth rates. Data plotted for ACC (A), calcite (B), and vaterite (C). In all cases linear growth rates are observed, either with a single rate or with two distinct rates. Lateral off-sets (B, C) have been set for clarity. Experimental conditions are given in Tables A1 and A2 (Appendix II). Measurements from repeated experiments at the same conditions are identified by '-#' in the panel legends

Finally, multiple distinct dissolution behaviors for ACC particles were observed under continued illumination by the electron beam, following thinning of the liquid layer. Some ACC particles underwent uniform shrinking to the point of complete disappearance, behaving as if they were liquid droplets evaporating into the surrounding medium (Figure 4.6, A to F). By contrast, other ACC particles at a later time in the same experiment exhibited behavior indicative of a dissolving solid, becoming rough and pitted over time (Figs. 4.6, G to L) before finally disappearing. Others exhibited behavior combining or intermediate to these two end points.

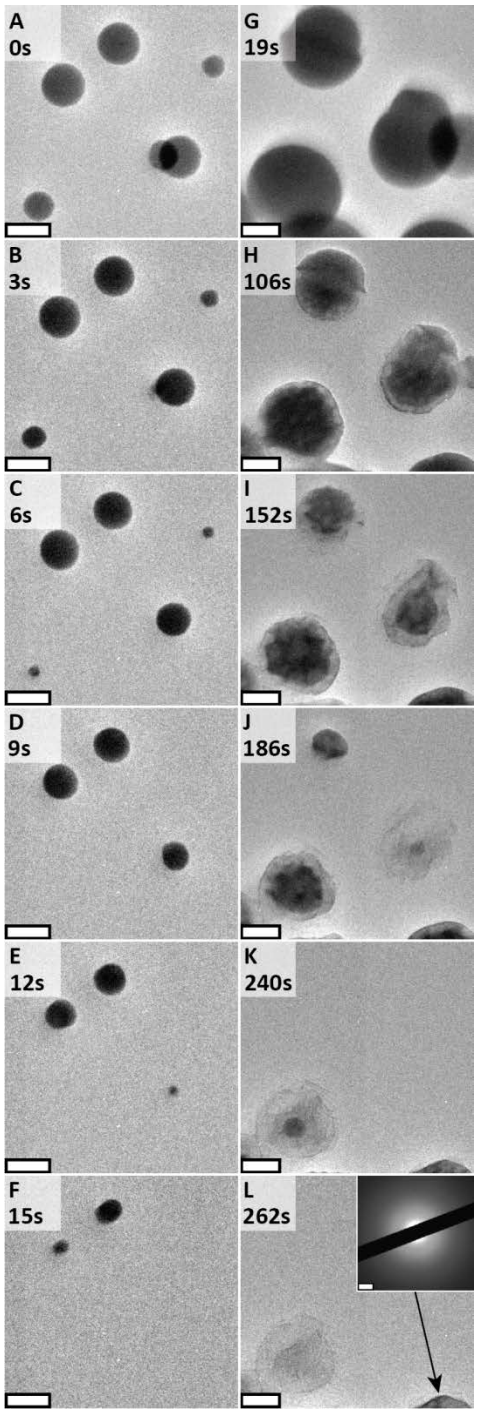

Figure 4.6 Two dissolution behaviors of ACC. Image sequence shows that some ACC particles undergo liquid-like shrinking and disappearance (A to F). At a later time in the same experiment, a second image sequence depicts nearby ACC particles exhibiting solid-like behavior, becoming pitted and developing roughened edges (G to L) while still amorphous [inset to (L)]. Scale bars are 500 nm in (A) to (L) and 2 nm^{-1} for the inset to (L). Solution conditions are 100:100/10:0.2 for all panels.

4.4 Discussion

The open questions about nucleation from electrolyte solutions are especially germane to the $CaCO_3$ system. Numerous studies have concluded that the final crystalline state often emerges long after the first appearance of ACC [5, 6, 9, 15, 17–19]. Physical chemical analyses [5] and cryogenic TEM [19] have given rise to a model of nucleation in which stable multi-ion clusters aggregate to form this first amorphous phase, which then transforms directly to the crystalline phases. Based on x-ray diffraction and optical microscopy, other studies have concluded that nucleation is described well by CNT, and crystalline phases that appear after ACC do so through dissolution and reprecipitation [9, 13]. Ex situ TEM [20] and nuclear magnetic resonance data [3] indicate the existence of a dense liquid phase. Molecular dynamics simulations predict polymeric clusters [10], and dense liquid phases [4] form through spinodal decomposition with ACC then forming through partial dehydration. However, the existence of these phenomena remains unproven. Moreover, spectroscopic analyses have shown that many $CaCO_3$-based biominerals form through aggregation and crystallization of ACC exhibiting multiple hydrated states [21, 22]. The spatial resolution of the experiments described in this chapter does not allow insight into the question of whether nucleation occurs via ion-by-ion attachment, as per CNT, or whether stable or metastable clusters serve as the primary species of addition. These observations do, however, demonstrate that multiple nucleation pathways exist for the crystalline phases of $CaCO_3$, including both direct formation from solution and direct transformation from more disordered phases. Moreover, these findings show that these multiple pathways and phases, summarized in Figure 4.7, are simultaneously available to the system at moderate to high supersaturations, as fully expected from classical considerations.

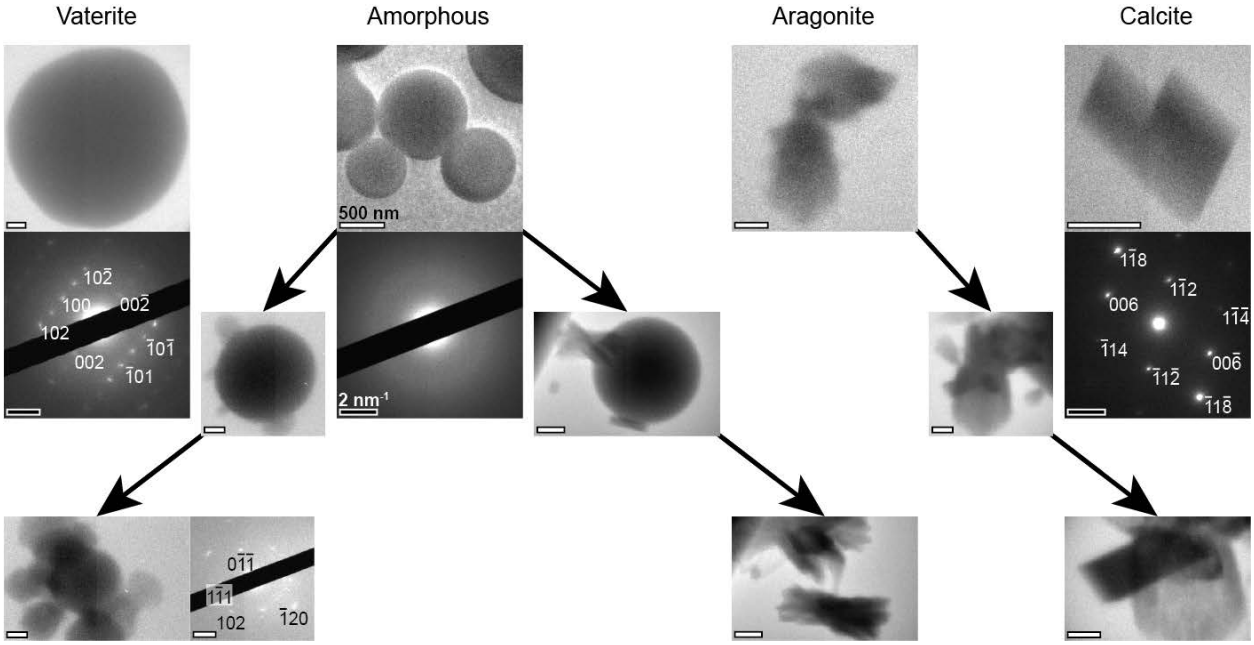

Figure 4.7 Formation pathways of $CaCO_3$. Direct formation from solution of amorphous phase and three anhydrous crystalline phases. Nucleation of vaterite and aragonite on existing amorphous particles leads to direct transformation from amorphous to crystal in these multi-step pathways. Crystal to crystal transformation also observed in the case of calcite forming on aragonite and growing at the expense of the initially formed phase. Scale bars 500 nm and 2 nm^{-1} for images and diffraction data, respectively.

These results also shed light on the process by which the disordered phases transform to the more ordered phase. In all cases for which the starting point of the secondary nucleus can be definitively identified, it lies approximately at the surface of the parent particle. This is consistent with previous in situ TEM observations of solidification in liquid $Au_{72}Ge_{28}$ droplets where the first ordered domain appeared at the surface [23]. Presumably, the higher mobility of surface ions and, in the case of solutions, their ability to rapidly exchange with the solution leads to this phenomenon.

Because the experimental cells used in these experiments have fluid layer thicknesses ranging from hundreds of nanometers to micrometers, effects of confinement might be expected. However, over the range of sizes observed here, the lateral growth rates remain constant and thus do not appear to be affected by the cell dimensions. Effects of confinement on nucleation could be evident in two ways: The first is through a similarity in cell dimensions to critical nucleus size [24], and the second is by structuring of the liquid layer through proximity to the cell membranes [25, 26]. However, the cell dimensions are orders of magnitude above the ~1- to 10 nm critical sizes of the crystalline phases [13], as well as the ~10 Å thickness of the hydration layers [25, 26].

The findings reported in this chapter also bear upon the controversy concerning the nature of ACC. Initially, a single amorphous phase was reported [27]. Later experiments demonstrated the existence of both hydrous ACC and anhydrous ACC [28]. Other research

suggested the existence of two forms of hydrous ACC [29], as well as proto-vateritic ACC and proto-calcitic ACC [30], with each serving as a precursor to the respective crystalline phase. The dense liquid phase referred to above was recently proposed as yet another amorphous form. The above results call into question whether these are fundamentally distinct phases or whether they exist as points on a continuum. Though certainly not conclusive, the disparate modes of ACC dissolution observed in this chapter suggest that the term ACC refers to a spectrum of structures ranging from the dense liquid phase to the anhydrous form, rather than a single or even a few closely related structures. Finally, whereas these results clearly show that direct transformation of ACC to the crystalline phase of $CaCO_3$ readily occurs, they confirm previous suggestions from low-resolution optical measurements, macroscopic x-ray diffraction data [13–15], and x-ray microscopy [31] that direct transformation from ACC to calcite is unlikely. Indeed, this formation pathway has never been directly observed.

4.5 References

1. J. W. Gibbs, On the equilibrium of heterogeneous substances. *Transactions of the Connecticut Academy of Arts and Sciences* **3**, 108-248 (1876); 343-524 (1878).

2. S. E. Wolf, J. Leiterer, M. Kappl, F. Emmerling, W. Tremel, Early homogenous amorphous precursor stages of calcium carbonate and subsequent crystal growth in levitated droplets. *Journal of the American Chemical Society* **130**, 12342–12347 (2008). doi:10.1021/ja800984y

3. M. A. Bewernitz, D. Gebauer, J. Long, H. Cölfen, L. B. Gower, A metastable liquid precursor phase of calcium carbonate and its interactions with polyaspartate. *Faraday Discussions* **159**, 291–312 (2012). doi:10.1039/c2fd20080e

4. A. F. Wallace, L. O. Hedges, A. Fernandez-Martinez, P. Raiteri, J. D. Gale, G. A. Waychunas, S. Whitelam, J. F. Banfield, J. J. De Yoreo, Microscopic evidence for liquid-liquid separation in supersaturated $CaCO_3$ solutions. *Science* **341**, 885–889 (2013). doi:10.1126/science.1230915

5. D. Gebauer, A. Völkel, H. Cölfen, Stable prenucleation calcium carbonate clusters. *Science* **322**, 1819–1822 (2008). doi:10.1126/science.1164271

6. H. Cölfen, M. Antonietti, *Mesocrystals and Non-Classical Crystallization* (Wiley, San Francisco, 2008).

7. A. E. S. Van Driessche, L. G. Benning, J. D. Rodriguez-Blanco, M. Ossorio, P. Bots, J. M. García-Ruiz, The role and implications of bassanite as a stable precursor phase to gypsum precipitation. *Science* **336**, 69–72 (2012). doi:10.1126/science.1215648

8. E. M. Pouget, P. H. Bomans, A. Dey, P. M. Frederik, G. de With, N. A. Sommerdijk, The development of morphology and structure in hexagonal vaterite. *Journal of the American Chemical Society* **132**, 11560–11565 (2010). doi:10.1021/ja102439r

9. P. Bots, L. G. Benning, J. D. Rodriguez-Blanco, T. Roncal-Herrero, S. Shaw, Mechanistic insights into the crystallization of amorphous calcium carbonate (ACC). *Crystal Growth & Design* **12**, 3806–3814 (2012). doi:10.1021/cg300676b

10. R. Demichelis, P. Raiteri, J. D. Gale, D. Quigley, D. Gebauer, Stable prenucleation mineral clusters are liquid-like ionic polymers. *Nature Communications* **2**, 590 (2011). doi:10.1038/ncomms1604

11. M. J. Williamson, R. M. Tromp, P. M. Vereecken, R. Hull, F. M. Ross, Dynamic microscopy of nanoscale cluster growth at the solid-liquid interface. *Nature Materials* **2**, 532–536 (2003). doi:10.1038/nmat944

12. Felmy, A., D. Girvin, AND E. Jenne. MINTEQ – A computer program for calculating aqueous geochemical equilibria. *U.S. Environmental Protection Agency*, Washington, D.C., EPA/600/3-84/032.

13. Q. Hu, M. H. Nielsen, C. L. Freeman, L. M. Hamm, J. Tao, J. R. I. Lee, T. Y. J. Han, U. Becker, J. H. Harding, P. M. Dove, J. J. De Yoreo, The thermodynamics of calcite nucleation at organic interfaces: Classical vs. non-classical pathways. *Faraday Discussions* **159**, 509–523 (2012). doi:10.1039/c2fd20124k

14. J. Aizenberg, D. A. Muller, J. L. Grazul, D. R. Hamann, Direct fabrication of large micropatterned single crystals. *Science* **299**, 1205–1208 (2003). doi:10.1126/science.1079204

15. J. R. I. Lee, T. Y. Han, T. M. Willey, D. Wang, R. W. Meulenberg, J. Nilsson, P. M. Dove, L. J. Terminello, T. van Buuren, J. J. De Yoreo, Structural development of mercaptophenol self-assembled monolayers and the overlying mineral phase during templated $CaCO_3$ crystallization from a transient amorphous film. *Journal of the American Chemical Society* **129**, 10370–10381 (2007). doi:10.1021/ja071535w

16. A. A. Chernov, *Modern Crystallography III* (Springer, Berlin, 1984).

17. E. Beniash, J. Aizenberg, L. Addadi, S. Weiner, Amorphous calcium carbonate transforms into calcite during sea urchin larval spicule growth. *Proceedings of the Royal Society of London Series B* **264**, 461–465 (1997). doi:10.1098/rspb.1997.0066

18. S. Weiner, I. Sagi, L. Addadi, Choosing the crystallization path less traveled. *Science* **309**, 1027–1028 (2005). doi:10.1126/science.1114920

19. E. M. Pouget, P. H. Bomans, J. A. Goos, P. M. Frederik, G. de With, N. A. Sommerdijk, The initial stages of template-controlled $CaCO_3$ formation revealed by cryo-TEM. *Science* **323**, 1455–1458 (2009). doi:10.1126/science.1169434

20. S. E. Wolf, L. Müller, R. Barrea, C. J. Kampf, J. Leiterer, U. Panne, T. Hoffmann, F. Emmerling, W. Tremel, Carbonate-coordinated metal complexes precede the formation of liquid amorphous mineral emulsions of divalent metal carbonates. *Nanoscale* **3**, 1158–1165 (2011). doi:10.1039/c0nr00761g

21. L. Addadi, S. Raz, S. Weiner, Taking advantage of disorder: Amorphous calcium carbonate and its roles in biomineralization. *Advanced Materials* **15**, 959–970 (2003). doi:10.1002/adma.200300381

22. Y. Politi, Y. Levi-Kalisman, S. Raz, F. Wilt, L. Addadi, S. Weiner, I. Sagi, Structural characterization of the transient amorphous calcium carbonate precursor phase in sea urchin embryos. *Advanced Functional Materials* **16**, 1289–1298 (2006). doi:10.1002/adfm.200600134

23. P. W. Sutter, E. A. Sutter, Dispensing and surface-induced crystallization of zeptolitre liquid metal-alloy drops. *Nature Materials* **6**, 363–366 (2007). doi:10.1038/nmat1894

24. L. O. Hedges, S. Whitelam, Patterning a surface so as to speed nucleation from solution. *Soft Matter* **8**, 8624–8635 (2012). doi:10.1039/c2sm26038g

25. L. Cheng, P. Fenter, K. L. Nagy, M. L. Schlegel, N. C. Sturchio, Molecular-scale density oscillations in water adjacent to a mica surface. *Physical Review Letters* **87**, 156103 (2001). doi:10.1103/PhysRevLett.87.156103

26. J. I. Kilpatrick, S.-H. Loh, S. P. Jarvis, Directly probing the effects of ions on hydration forces at interfaces. *Journal of the American Chemical Society* **135**, 2628–2634 (2013). doi:10.1021/ja310255s

27. L. Brečević, A. E. Nielsen, Solubility of amorphous calcium carbonate. *Journal of Crystal Growth* **98**, 504–510 (1989). doi:10.1016/0022-0248(89)90168-1

28. N. Koga, Y. Yamane, Thermal behaviors of amorphous calcium carbonates prepared in aqueous and ethanol media. *Journal of Thermal Analysis and Calorimetry* **94**, 379–387 (2008). doi:10.1007/s10973-008-9110-3

29. A. V. Radha, T. Z. Forbes, C. E. Killian, P. U. Gilbert, A. Navrotsky, Transformation and crystallization energetics of synthetic and biogenic amorphous calcium carbonate. *Proceedings of the National Academy of Sciences of the United States of America* **107**, 16438–16443 (2010). doi:10.1073/pnas.1009959107

30. D. Gebauer, P. N. Gunawidjaja, J. Y. Ko, Z. Bacsik, B. Aziz, L. Liu, Y. Hu, L. Bergström, C. W. Tai, T. K. Sham, M. Edén, N. Hedin, Proto-calcite and proto-vaterite in amorphous calcium carbonates. *Angewandte Chemie-International Edition* **49**, 8889–8891 (2010). doi:10.1002/anie.201003220

31. J. Rieger, J. Thieme, C. Schmidt, Study of precipitation reactions by x-ray microscopy: $CaCO_3$ precipitation and the effect of polycarboxylates. *Langmuir* **16**, 8300–8305 (2000). doi:10.1021/la0004193

Chapter 5

Conclusions and Future Directions

5.1 Conclusions

5.1.1 $CaCO_3$ Formation Pathways

The data presented within this dissertation suggest that calcium carbonate formation is well-described by the theoretical framework of classical nucleation theory. As described in Chapter 1, the solid phases of $CaCO_3$ have similar solubilities and relatively large interfacial energies (~100 mJ/m^2). Due to the latter, in order to study nucleation on a manageable experimental time-scale, the solution must be driven to high supersaturation which results in multiple phases and pathways becoming thermodynamically available. Even when the concentration is raised to the solubility limit of the amorphous phase so that all four of the common polymorphs are stable with respect to the dissolved state, the free energy barrier to forming calcite in solution, which is the most stable phase, is still on the order of 100 $\mathbf{k}T$ as shown in Chapter 2. Hence pathways can be complex and the relatively similar energy barriers to formation of the different phases makes the selection of a single phase unlikely in the absence of a biased system, such as a preferential surface which serves as a physicochemical template.

Indeed, in the absence of such a template the nucleation of one phase versus another, and the phase pathway through which an individual crystal develops, appeared to be random, as described in detail in Chapter 4. With the caveat that the precise solution conditions in the imaging area are unknown, the various formation pathways were found to exist across a range of supersaturations. As the initial solute concentrations were raised, ACC became increasingly predominant and more pathways were observed. These findings are consistent with expectations of CNT that as the energy barriers are lowered through increasing supersaturation, multiple phases and pathways should become increasingly accessible due to the high interfacial free energy and large free energy barrier to nucleation in this system, as discussed above. However, while they contradict models that allow only for pathways involving initial formation of ACC either from pre-nucleation clusters or dense liquid droplets, they provide no evidence for or against the existence of either species, because the resolution is inadequate to see clusters of the size envisioned by the pre-nucleation cluster model and, when ACC precursors were observed, the TEM images did not definitively reveal whether they were solid or liquid.

5.1.2 SAM-Templated $CaCO_3$ Formation Pathways

With the addition of alkanethiol SAMs which are well known to bias the final phase and orientation of nucleating $CaCO_3$ particles, data from low resolution in situ microscopies suggest that the mineralization pathways are likewise controlled. For –COOH surfaces favorable to calcite formation, crystallization appeared to occur in the absence of any transient, metastable solid precursor phase. Even when the experimental setup produced an expected supersaturation gradient with the lowest supersaturation at the template surface, calcite crystals were observed to form a substantial amount of time prior to the homogeneous formation of the amorphous phase. SAMs functionalized with an –OH moiety provide a contrasting case. With few exceptions, the first phase observed was consistent with the amorphous phase irrespective of experimental setup. The exceptional cases can be explained by defects on the surface or contaminating particles in solution which serve as nucleation sites for calcite crystals. The ACC particles form and/or settle on the surface, where they remain until the system is further disturbed. Homogeneous calcite nucleation events which occur randomly in the supersaturated solution lead to crystals settling onto the ACC-covered SAM surface and growing through the dissolution of the amorphous particles and re-precipitation of the $CaCO_3$ onto the stable crystal.

5.1.3 Calcite Nucleation Rates on –COOH SAMs

The different behaviors in Section 5.1.2 can be described by the results of the nucleation rate experiments discussed in Chapter 2 in conjunction with other reports in the literature. SAMs with a –COOH surface substantially reduce the effective free energy for a nucleating calcite crystal, leading to a much lower energy barrier to nucleation of the stable phase, consistent with predictions of CNT. Using a similar experimental approach, Hamm *et al.* investigated nucleation rates for a number of different surface chemistries [1]. All of the SAMs tested gave consistent results with those described in Chapter 2, except for the –OH surface. For this exceptional case, the calcite nucleation rate was extremely low and appeared to have no dependence on the supersaturation of the solution. A possible explanation for this observation, consistent with the other results from the two studies, would be that the –OH surface presents an energetically unfavorable surface for calcite nucleation and thus prevents heterogeneous nucleation. It is only through a disturbance in the system – whether a surface defect on the SAM, a contaminant in solution, or otherwise – that calcite sporadically forms. It would be interesting to follow the method of Hamm *et al.* and use dynamic force spectroscopy to measure the free energy of binding for an –OH SAM on a calcite surface. A weak binding energy would indicate a relatively unfavorable interfacial energy between the crystal and SAM, and would validate the above hypothesis as well as be consistent with the framework of CNT.

5.2 Future Directions

5.2.1 Liquid Phase TEM Observations of SAM-Templated $CaCO_3$ Formation Pathways

The conclusions in Section 5.1.2 are based on low resolution methods that provide indirect evidence for the formation pathways described. Liquid phase TEM provides the obvious solution to this limitation, and substantial effort has been undertaken to conduct formation pathway experiments on SAMs in the TEM liquid cell. However, to date, none of these preliminary attempts have been successful.

The first approach was to evaporate a 50×50 μm^2 thin metal film (1.5 nm Ti, 8 nm Au) over a portion of the electron-transparent window of one of the liquid flow cell components. By restricting the region for templated nucleation thusly, it was expected that the reaction would only occur in the region visible in the TEM. This chip was then placed in an ethanolic SAM solution overnight for the monolayer to assemble and rinsed prior to cell assembly on the TEM liquid flow stage. This precluded the use of a step in sample preparation methodology in Chapter 4, where the fluid cell components were placed in a plasma cleaner immediately prior to assembly to make the internal cell surfaces hydrophilic, as the nitride is otherwise naturally hydrophobic. Thus during cell assembly, the solution droplet (used to pre-wet the cell during stage assembly) would bead up on the surface rather than spread across to the outer edges. When mixing experiments were conducted in the microscope, no reactions were observed to occur over the course of tens of experiments covering a range of solution conditions. Similar experiments run as a control, with the metal film deposited but without the organic monolayer – therefore allowing the use of the plasma cleaner during sample preparation – consistently yielded crystal formation events on and near the metal film as expected (Au being a favorable surface for $CaCO_3$ nucleation, relative to silicon nitride).

A potential explanation for the difference between the Au control and SAM experiments is based on the hydrophilicity/hydrophobicity of the surface. The solution droplet spreads to the edge of the cell in the case of the control experiment, leading to a continuous body of liquid throughout the TEM liquid stage and cell. Thus, when the reagents are pumped through the microfluidic system, they can pass into and through the liquid cell, creating a supersaturated solution from which solid $CaCO_3$ nucleates and can be observed. However, with the SAM organized on the metal film, the solution droplet beads up and doesn't spread to the edge of the assembled liquid cell. Thus there is an air barrier between the liquid in the cell and the reagent mixture that is pumped through the TEM stage plumbing. In this scenario, none of the reagent mixture flows into or through the cell, and therefore no nucleation events can be observed.

To get around this issue the experimental approach was changed. As described in Chapter 2, one of the methods for creating supersaturated $CaCO_3$ solutions is through the decomposition of $(NH_4)_2CO_3$ to diffuse $CO_{2(g)}$ into a $Ca^{2+}_{(aq)}$ solution. Figure 5.1 shows how this approach was employed with the TEM liquid flow stage. With this approach, which had successfully been used previously by Smeets *et al.* [2], $CaCO_3$ formation did indeed occur. However, the expected calcite nucleated on the (012) plane was not observed. Different phases were found to form and

did not evolve be consistent with the literature observations from bulk studies. The phenomena were qualitatively consistent with studies looking at formation of $CaCO_3$ and other minerals in confined spaces [3-6]. Stephens *et al.* used the CO_2 diffusion method for generating a supersaturated solution in a calcium rich solution between two crossed cylinders coated with gold on which a SAM was organized [3]. They found that surface separations smaller than 10 µm affected first the morphology of the calcite crystals, and at smaller separations resulted in a stabilization of ACC. The authors attribute the observations to a confinement effect, however the results discussed in Chapter 4 of this dissertation suggest that their results might be more accurately attributed to the combination of the confined geometry and the passive diffusion reaction conditions. While the root cause of these observations remains poorly understood, it is clear that the experimental approach is not compatible with liquid phase TEM, which has (nominally) a sub-micron fluid layer thickness.

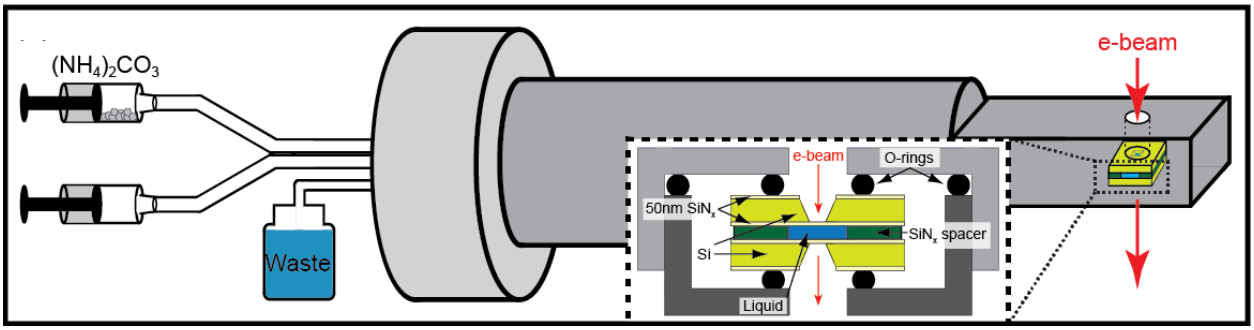

Figure 5.1 Dual-inlet TEM flow stage configured for diffusing gaseous decomposition products of $(NH_4)_2CO_3$ into Ca^{2+}-rich droplet in liquid cell, with inset showing sample region in detail. A syringe containing $(NH_4)_2CO_3$ powder is connected to an empty fluid line, to allow $NH_{3(g)}$ and $CO_{2(g)}$ to diffuse through the system and into the $CaCl_2$ solution droplet filling the channel between the windows of the liquid cell. The diffusion of $CO_{2(g)}$ into the Ca^{2+}-rich solution continually increases the supersaturation of solid $CaCO_3$ phases, creating a driving force for precipitation.

If it is possible to conduct $CaCO_3$ formation pathway experiments on SAMs in liquid phase TEM, the preliminary results described in this section suggest that the following approach may be successful. Rather than evaporate a metal film onto a small region of a liquid cell component, the entire surface should be covered. The reason for this is that –COOH SAMs are relatively hydrophilic. Thus when the sample is prepared the solution droplet used to pre-wet the cell should spread to the edge of the cell. When the stage is completely assembled there should therefore be no air gap as hypothesized above, and the pumped reactants should mix and flow into the cell. While nucleation events would be expected to occur across the substantial region of the liquid cell unobservable in the TEM, perhaps a sufficiently high supersaturated solution would yield nucleation events in the window region.

5.2.2 Outlook for Liquid Phase TEM

The data presented in Chapters 3 and 4 highlight the utility of liquid phase TEM in better understanding phenomena at the onset of crystal formation. This relatively new experimental technique has opened a window to direct observations of nucleation pathways, growth mechanisms, and the interactions between the primary crystallizing material and additives. The ability to gather crystallographic information either through lattice resolution imaging or through electron diffraction further enhances the utility of this approach in understanding processes controlling materials formation. However, as should be expected given the relative youth of the liquid phase TEM field, there are numerous areas for future development, which will greatly enhance the technique's utility in quantitatively understanding a wider variety of experimental systems.

As mentioned in Sections 4.2.1 and 4.2.3, current flow stage designs allow the liquid stream to flow around the outside of the cell in addition to flowing through the channel and across the imaging region within the cell. As such, flow patterns within, and mixing characteristics of, flow stages remain largely unknown. This results in some degree of uncertainty regarding the solution composition under electron beam illumination, particularly in the case of multiple inlet stages. As an example, during the course of the experiments detailed in Chapter 4, formation of some $CaCO_3$ phases was observed from solutions which were expected to be undersaturated with respect to those phases, based on calculations using the starting reagent concentrations and relative flow rates of the two precursor streams (Appendix II). However, the surprising results may not be caused entirely, or even to a significant extent, by the uncertainty in fluid flow pathways. Another, perhaps more important, effect on the sample arises from interaction with the electron beam.

How the electron beam affects reaction solutions is a significant question that has only recently begun to be addressed. A number of liquid phase TEM studies have utilized the electron beam to reduce solvated metal precursors to grow nanocrystals from solution, leaving open the question of what radiolytic products are additionally produced during interaction with the sample. Woehl *et al.* discussed the species that arise through the beam's interaction with the silicon nitride membranes and the liquid layer, and identified the aqueous electron as the reducing agent for metal precursors [7]. More recent efforts have gone toward building a predictive model of each of the species produced through electron irradiation, their spatial concentrations relative to the electron beam, lifetimes, and effect on the liquid's pH [8, 9]. Extending this model from water, for which it was originally developed, to complex solutions with many dissolved species will allow for more quantitative studies of crystallization processes in the future.

The above model predicts that pH changes of potentially significant amounts may be induced in the sample solution as a result of imaging in the TEM. At present there are no in situ diagnostics to measure such changes in the experimental conditions. In order to conduct a quantitative analysis of the energetics of crystallization, it is crucial to know solution parameters such as pH and temperature. Future developments of on-device probes that allow in situ measurement of — and control over — these and other parameters will broaden the utility of liquid phase TEM.

Although still in its early years of development, liquid phase TEM has already become an invaluable tool in understanding nucleation, growth, and control of these processes with the use of additives. Future advancements of the technique will only expand its utility in addressing such fundamental areas of materials formation. Through its unique ability to track nanoparticle motion, application of liquid phase TEM to the post nucleation phase of solutions can provide critical information on the dynamics and mechanisms of crystallization through nanoparticle assembly, such as oriented attachment [10, 11] as described elsewhere in this volume. The spatial and temporal resolutions of liquid phase TEM are also well suited to exploring the occurrence of novel crystallization pathways, such as liquid-liquid phase separation, a process that has been implicated in both protein [12] and simple electrolyte solutions [13]. The demonstration that both macromolecular and mineral phases can be simultaneously observed during crystallization [2, 14] opens up a new approach to understanding the formation of biominerals, such as bones and teeth, in which organic scaffolds organize mineral constituents [15]. In all of these examples, incorporation of in situ diagnostics to provide a better understanding of the solution conditions in the volume illuminated by the electron beam, and the extension of current models to better represent experimental solutions, would allow for quantitative studies to better understand the mechanisms underlying crystallization processes.

5.3 References

1. L. M. Hamm, A. J. Giuffre, N. Han, J. Tao, D. Wang, J. J. De Yoreo, P. M. Dove, Reconciling disparate views of template-directed nucleation through measurement of calcite nucleation kinetics and binding energies. *Proceedings of the National Academy of Sciences* **111**, 1304-1309 (2014). doi:10.1073/pnas.1312369111

2. P. J. M. Smeets, K. R. Cho, R. G. E. Kempen, N. A. J. M. Sommerdijk, J. J. De Yoreo, Calcium carbonate nucleation driven by ion binding in a biomimetic matrix revealed by in situ electron microscopy. *Nature Materials* **14**, 394-399 (2015). doi:10.1038/nmat4193

3. C. J. Stephens, S. F. Ladden, F. C. Meldrum, H. K. Christenson, Amorphous calcium carbonate is stabilized in confinement. *Advanced Functional Materials* **20**, 2108-2115 (2010). doi:10.1002/adfm.201000248

4. B. Cantaert, E. Beniash, F. C. Meldrum, Nanoscale confinement controls the crystallization of calcium phosphate: Relevance to bone formation. *Chemistry-a European Journal* **19**, 14918-14924 (2013). doi:10.1002/chem.201302835

5. Y. W. Wang, H. K. Christenson, F. C. Meldrum, Confinement leads to control over calcium sulfate polymorph. *Advanced Functional Materials* **23**, 5615-5623 (2013). doi:10.1002/adfm.201300861

6. A. S. Schenk, E. J. Albarracin, Y. Y. Kim, J. Ihli, F. C. Meldrum, Confinement stabilises single crystal vaterite rods. *Chemical Communications* **50**, 4729-4732 (2014). doi:10.1039/c4cc01093k

7. T. J. Woehl, J. E. Evans, L. Arslan, W. D. Ristenpart, N. D. Browning, Direct in situ determination of the mechanisms controlling nanoparticle nucleation and growth. *ACS Nano* **6**, 8599-8610 (2012). doi:10.1021/nn303371y

8. J. M. Grogan, N. M. Schneider, F. M. Ross, H. H. Bau, Bubble and pattern formation in liquid induced by an electron beam. *Nano Letters* **14**, 359-364 (2014). doi:10.1021/nl404169a

9. N. M. Schneider, M. M. Norton, B. J. Mendel, J. M. Grogan, F. M. Ross, H. H. Bau, Electron-water interactions and implications for liquid cell electron microscopy. *Journal of Physical Chemistry C* **118**, 22373-22382 (2014). doi:10.1021/jp507400n

10. D. S. Li, M. H. Nielsen, J. R. I. Lee, C. Frandsen, J. F. Banfield, J. J. De Yoreo, Direction-specific interactions control crystal growth by oriented attachment. *Science* **336**, 1014-1018 (2012). doi:10.1126/science.1219643

11. J. M. Yuk, J. Park, P. Ercius, K. Kim, D. J. Hellebusch, M. F. Crommie, J. Y. Lee, A. Zettl, A. P. Alivisatos, High-resolution EM of colloidal nanocrystal growth using graphene liquid cells. *Science* **336**, 61-64 (2012). doi:10.1126/science.1217654

12. O. Galkin, K. Chen, R. L. Nagel, R. E. Hirsch, P. G. Vekilov, Liquid-liquid separation in solutions of normal and sickle cell hemoglobin. *Proceedings of the National Academy of Sciences of the United States of America* **99**, 8479-8483 (2002). doi:10.1073/pnas.122055299

13. A. F. Wallace, L. O. Hedges, A. Fernandez-Martinez, P. Raiteri, J. D. Gale, G. A. Waychunas, S. Whitelam, J. F. Banfield, J. J. De Yoreo, Microscopic evidence for liquid-liquid separation in supersaturated $CaCO_3$ solutions. *Science* **341**, 885-889 (2013). doi:10.1126/science.1230915

14. J. E. Evans, K. L. Jungjohann, P. C. K. Wong, P.-L. Chiu, G. H. Dutrow, I. Arslan, N. D. Browning, Visualizing macromolecular complexes with in situ liquid scanning transmission electron microscopy. *Micron* **43**, 1085-1090 (2012). doi:10.1016/j.micron.2012.01.018

15. F. Nudelman, K. Pieterse, A. George, P. H. H. Bomans, H. Friedrich, L. J. Brylka, P. A. J. Hilbers, G. de With, N. Sommerdijk, The role of collagen in bone apatite formation in the presence of hydroxyapatite nucleation inhibitors. *Nature Materials* **9**, 1004-1009 (2010). doi:10.1038/nmat2875

Appendix I

Dependence of Nucleation Rate on Supersaturation

In classical nucleation theory (CNT), the free energy change upon nucleation is given by:

$$\Delta g = -\frac{V}{\Omega}\mathbf{k}T\sigma + A_b\left(\alpha_{cs} - \alpha_{fs}\right) + A_s\alpha_{cf} \tag{A1.1}$$

where V is the volume of the nucleus, Ω is the molecular volume of the growth unit, **k** is Boltzmann's constant, T is the absolute temperature, σ is the supersaturation, A_b is the area of the base in contact with the film, A_s is the area of the surface in contact with the solution, and α_{cf}, α_{fs} and α_{cs} are the interfacial energies of the crystal-fluid, fluid-substrate and crystal-substrate interfaces. The thermodynamic barrier is given by the maximum in Δg with respect to crystal size, which occurs at:

$$\Delta g_c = \frac{f\alpha_{het}^3\Omega^2}{(\mathbf{k}T\sigma)^2} \quad \text{with} \quad \alpha_{het} = \alpha_{cf} - h\left(\alpha_{fs} - \alpha_{cs}\right) \tag{A1.2}$$

The corresponding nucleation rate is given by:

$$J_{\mathrm{n}} = Ae^{-E_A/\mathbf{k}T}e^{-\Delta g_c/\mathbf{k}T} \tag{A1.3}$$

which can be rewritten as follows:

$$\ln(J_{\mathrm{n}}) = A' - \frac{f\alpha_{het}^3\Omega^2}{(\mathbf{k}T)^3}\left(\frac{1}{\sigma^2}\right) \quad \text{with} \quad A' = \ln\left(Ae^{-E_A/\mathbf{k}T}\right) \tag{A1.4}$$

where A is a pre-factor that is independent of σ, and E_A is an effective activation barrier that captures the kinetic barriers to reactions such as desolvation of solute ions, attachment to the forming nucleus and structural rearrangements. Here both f and h are numbers that depend on the aspect ratio of the nucleus. For nucleation of a calcite rhombohedron on the (012) plane, analysis of the volume and surface areas leads to $f = 19.71$ and $h = 0.525$. However, for a large range of nucleation planes, these numbers are nearly identical, varying by no more than about 10%. Because the interfacial energy is raised to the third power in the free energy barrier, these small variations in f have negligible effect ($< 2.5\%$) on the values of α_{het} extracted from the nucleation rate data.

The interfacial free energy can be generalized to an excess free energy, Δg_{ex}. In this regard, the change in free energy associated with formation of a solute particle is given by:

(A1.5) $$\Delta g = \frac{dg}{dn}\Delta n + \Delta g_{ex}$$

In CNT Δg_{ex} is given by the interfacial energy times the surface area of the nucleus, which is assumed to be constant. Consequently, Δg_{ex} scales with the square of the particle size, i.e., $\Delta g_{ex}/A_s = \alpha =$ constant. Two factors that can have a further and significant impact on the nucleation barrier are a more complex size dependence and the existence of local minima in Δg_{ex} vs. size.

The effect of size dependence can easily be incorporated. For example, if the size dependence is given by an exponential rise from a minimum value, then $\Delta g_{ex} = \alpha_\infty A_s\{1 - exp[-(L - L_0)/L_\infty]\}$, where L is the edge length of the rhombohedron, L_0 is the value of L at which Δg_{ex} decreases to zero, and is L_∞ the value of L at which Δg_{ex} reaches $1 - exp[-(L - L_0)/L_\infty]$ of its bulk value. When the critical size is of the order of or less than the dimensions at which the dependence of the excess free energy on size becomes significant, the consequence of is a reduction in the energy penalty associated with creating the critical nucleus. The impact of this effect is shown in Figure 2.2B.

The effect of clusters can also be incorporated into Equation (A1.1) by writing:

(A1.6) $$\Delta g = -\frac{V}{\Omega}\mathbf{k}T\sigma + A_b\left(\alpha_{cs} - \alpha_{fs}\right) + A_b\alpha_{cf} - \frac{V}{V_{cl}}\Delta g_{ex}$$

where V_{cl} and Δg_{ex} are the volume and excess free energy of a cluster above that of the free ions. For homogeneous nucleation of rhombohedral calcite of edge length L from spherical clusters of radius r_{cl}, $V/V_{cl} = 0.978(3L^3/4\pi r_{cl}^3)$ giving:

(A1.7) $$\Delta g = -\frac{0.978L^3}{\Omega}\mathbf{k}T\sigma + 6 \cdot 0.978L^2\alpha_{cf} - \frac{3 \cdot 0.978L^3}{4\pi r_{cl}^3}\Delta g_{ex}$$

When the clusters lie in a local minimum, $\Delta g_{ex} > 0$ (Figure 2.2D, solid green line). Therefore, because the clusters lie higher in free energy than the ions, aggregating them to form a critical nucleus carries less of an energy penalty. On the other hand, if the clusters lie in a global minimum, i.e., they are lower in energy than the free ions, $\Delta g_{ex} < 0$ (Figure 2.2D, dashed green line) and there is an added energy penalty associated with nucleation through their aggregation. The impact of cluster aggregation for positive Δg_{ex} is illustrated in Figure 2.2C.

Beyond inducing changes in the magnitude of the barrier, the second effect of these features in the free energy landscape is that the relationship between the barrier (or rate) and the supersaturation deviates from the simple α^3/σ^2 dependence seen in Equations (A1.2) and (A1.3). Even in the case of a simple size dependence, such as the exponential rise described above, the resulting relationship is complex. In the case of cluster aggregation in an otherwise flat landscape, if we write $\Delta g_{ex} = 4\pi r_{cl}^2\alpha_{cl}$, where α_{cl} is the effective interfacial energy of a cluster, then in Equation (A1.3) σ is simply replaced by:

(A1.8) $$\sigma' = \sigma + \frac{3\Omega\alpha_{cl}}{r_{cl}\mathbf{k}T}$$

In the case where the minimum is global, there is a stable population of clusters with a narrow size distribution and the plus sign in Equation (A1.7) is replaced with a minus sign. For $r_{cl} \geq 0.5$ nm, $\alpha_{cl} \leq 0.5\alpha$ and $\sigma \geq 4.5$, Equation (A1.7) gives $(\sigma' - \sigma)/\sigma < 0.1$. Consequently, for the range of concentrations examined in this study, deviations from α^3/σ^2 due to cluster aggregation are unlikely to be observed.

Appendix II

Calculated Experimental Conditions and Observed $CaCO_3$ Phases

Table A1. Calculated pH and $CaCO_3$ supersaturations. Supersaturations for the major phases of calcium carbonate and pH values were calculated using the Visual MINTEQ (Jon Petter Gustafsson) software [1], for each experimental condition. These calculated values are not expected to accurately reflect the conditions observed, as discussed in the materials and methods section.

	A	B	C	D	E	F	G	H	I
	Concentrations	10 mM $CaCl_2$ & 10 mM $NaHCO_3$	20 mM $CaCl_2$ & 20 mM $NaHCO_3$	30 mM $CaCl_2$ & 30 mM $NaHCO_3$	40 mM $CaCl_2$ & 40 mM $NaHCO_3$	50 mM $CaCl_2$ & 50 mM $NaHCO_3$	60 mM $CaCl_2$ & 60 mM $NaHCO_3$	70 mM $CaCl_2$ & 70 mM $NaHCO_3$	100 mM $CaCl_2$ & 100 mM $NaHCO_3$	30 mM $CaCl_2$ into 100 mM $NaHCO_3$
1	Flow rates ($\mu L\ min^{-1}$) Ca^{2+} : 10 CO_3^{2-} : 0.2		ACC Vaterite Calcite	ACC Calcite	ACC Vaterite Calcite	ACC Vaterite Aragonite Calcite	ACC Vaterite Calcite	ACC Vaterite Aragonite Calcite	ACC	ACC Vaterite Aragonite Calcite
2	Ca^{2+} : 9 CO_3^{2-} : 1		Vaterite	ACC	ACC Vaterite Aragonite Calcite	ACC Aragonite		ACC Vaterite Aragonite		Vaterite Calcite
3	Ca^{2+} : 8 CO_3^{2-} : 2		ACC Vaterite Aragonite	ACC Calcite	ACC Vaterite Aragonite	ACC		Calcite	ACC Vaterite Calcite	Calcite
4	Ca^{2+} : 6.67 CO_3^{2-} : 3.33		Vaterite Aragonite	ACC Calcite	ACC Vaterite	ACC Vaterite Calcite		ACC Vaterite	ACC Calcite	Calcite
5	Ca^{2+} : 5 CO_3^{2-} : 5		ACC Vaterite	ACC Vaterite Calcite	ACC Vaterite Calcite	ACC ACC Aragonite	ACC Vaterite Calcite	ACC Vaterite	ACC Calcite	ACC Calcite

Table A2. Observed $CaCO_3$ phases. Reagent concentrations and flow rates of conducted experiments, with observed phases listed. Solution conditions not tested are crossed out.

	A	B	C	D	E	F	G	H	I
Concentrations	10 mM $CaCl_2$ & 10 mM $NaHCO_3$	20 mM $CaCl_2$ & 20 mM $NaHCO_3$	30 mM $CaCl_2$ & 30 mM $NaHCO_3$	40 mM $CaCl_2$ & 40 mM $NaHCO_3$	50 mM $CaCl_2$ & 50 mM $NaHCO_3$	60 mM $CaCl_2$ & 60 mM $NaHCO_3$	70 mM $CaCl_2$ & 70 mM $NaHCO_3$	100 mM $CaCl_2$ & 100 mM $NaHCO_3$	30 mM $CaCl_2$ into 100 mM $NaHCO_3$
Flow rates (µL min^{-1})									
1 Ca^{2+} : 10 CO_3^{2-} : 0.2	pH = 7.798	pH = 7.722	pH = 7.673	pH = 7.636	pH = 7.606	pH = 7.581	pH = 7.560	pH = 7.507	pH = 7.680
	σ(ACC) = -5.190	σ(ACC) = -4.269	σ(ACC) = -3.762	σ(ACC) = -3.412	σ(ACC) = -3.145	σ(ACC) = -2.929	σ(ACC) = -2.747	σ(ACC) = -2.323	σ(ACC) = -2.551
	σ(Vat) = -1.688	σ(Vat) = -0.767	σ(Vat) = -0.262	σ(Vat) = 0.087	σ(Vat) = 0.355	σ(Vat) = 0.571	σ(Vat) = 0.755	σ(Vat) = 1.177	σ(Vat) = 0.949
	σ(Ara) = -0.716	σ(Ara) = 0.205	σ(Ara) = 0.711	σ(Ara) = 1.061	σ(Ara) = 1.329	σ(Ara) = 1.545	σ(Ara) = 1.727	σ(Ara) = 2.151	σ(Ara) = 1.923
	σ(Cal) = -0.385	σ(Cal) = 0.537	σ(Cal) = 1.043	σ(Cal) = 1.391	σ(Cal) = 1.660	σ(Cal) = 1.877	σ(Cal) = 2.059	σ(Cal) = 2.482	σ(Cal) = 2.254
2 Ca^{2+} : 9 CO_3^{2-} : 1	pH = 7.841	pH = 7.750	pH = 7.697	pH = 7.658	pH = 7.628	pH = 7.603	pH = 7.581	pH = 7.529	pH = 7.705
	σ(ACC) = -3.553	σ(ACC) = -2.664	σ(ACC) = -2.167	σ(ACC) = -1.821	σ(ACC) = -1.557	σ(ACC) = -1.340	σ(ACC) = -1.158	σ(ACC) = -0.737	σ(ACC) = -0.992
	σ(Vat) = -0.051	σ(Vat) = 0.838	σ(Vat) = 1.333	σ(Vat) = 1.681	σ(Vat) = 1.946	σ(Vat) = 2.162	σ(Vat) = 2.344	σ(Vat) = 2.763	σ(Vat) = 2.508
	σ(Ara) = 0.921	σ(Ara) = 1.810	σ(Ara) = 2.307	σ(Ara) = 2.653	σ(Ara) = 2.920	σ(Ara) = 3.134	σ(Ara) = 3.316	σ(Ara) = 3.737	σ(Ara) = 3.482
	σ(Cal) = 1.253	σ(Cal) = 2.141	σ(Cal) = 2.639	σ(Cal) = 2.984	σ(Cal) = 3.249	σ(Cal) = 3.465	σ(Cal) = 3.647	σ(Cal) = 4.069	σ(Cal) = 3.813
3 Ca^{2+} : 8 CO_3^{2-} : 2	pH = 7.863	pH = 7.771	pH = 7.717	pH = 7.679	pH = 7.649	pH = 7.624	pH = 7.603	pH = 7.552	pH = 7.732
	σ(ACC) = -2.901	σ(ACC) = -2.012	σ(ACC) = -1.513	σ(ACC) = -1.167	σ(ACC) = -0.900	σ(ACC) = -0.686	σ(ACC) = -0.504	σ(ACC) = -0.083	σ(ACC) = -0.380
	σ(Vat) = 0.599	σ(Vat) = 1.490	σ(Vat) = 1.987	σ(Vat) = 2.335	σ(Vat) = 2.600	σ(Vat) = 2.816	σ(Vat) = 2.998	σ(Vat) = 3.419	σ(Vat) = 3.120
	σ(Ara) = 1.573	σ(Ara) = 2.461	σ(Ara) = 2.961	σ(Ara) = 3.307	σ(Ara) = 3.574	σ(Ara) = 3.788	σ(Ara) = 3.970	σ(Ara) = 4.391	σ(Ara) = 4.094
	σ(Cal) = 1.904	σ(Cal) = 2.793	σ(Cal) = 3.290	σ(Cal) = 3.638	σ(Cal) = 3.903	σ(Cal) = 4.119	σ(Cal) = 4.301	σ(Cal) = 4.723	σ(Cal) = 4.426
4 Ca^{2+} : 6.67 CO_3^{2-} : 3.33	pH = 7.893	7.801	pH = 7.748	pH = 7.710	pH = 7.681	pH = 7.657	pH = 7.636	pH = 7.587	pH = 7.770
	σ(ACC) = -2.473	σ(ACC) = -1.575	σ(ACC) = -1.073	σ(ACC) = -0.723	σ(ACC) = -0.456	σ(ACC) = -0.239	σ(ACC) = -0.058	σ(ACC) = 0.364	σ(ACC) = -0.002
	σ(Vat) = 1.029	σ(Vat) = 1.927	σ(Vat) = 2.429	σ(Vat) = 2.777	σ(Vat) = 3.044	σ(Vat) = 3.260	σ(Vat) = 3.442	σ(Vat) = 3.864	σ(Vat) = 3.498
	σ(Ara) = 2.003	σ(Ara) = 2.899	σ(Ara) = 3.401	σ(Ara) = 3.751	σ(Ara) = 4.018	σ(Ara) = 4.234	σ(Ara) = 4.416	σ(Ara) = 4.838	σ(Ara) = 4.472
	σ(Cal) = 2.333	σ(Cal) = 3.231	σ(Cal) = 3.732	σ(Cal) = 4.080	σ(Cal) = 4.350	σ(Cal) = 4.564	σ(Cal) = 4.748	σ(Cal) = 5.167	σ(Cal) = 4.803
5 Ca^{2+} : 5 CO_3^{2-} : 5	pH = 7.937	pH = 7.848	pH = 7.795	pH = 7.759	pH = 7.730	pH = 7.707	pH = 7.687	pH = 7.641	pH = 7.822
	σ(ACC) = -2.208	σ(ACC) = -1.299	σ(ACC) = -0.790	σ(ACC) = -0.437	σ(ACC) = -0.170	σ(ACC) = 0.048	σ(ACC) = 0.230	σ(ACC) = 0.652	σ(ACC) = 0.177
	σ(Vat) =1.294	σ(Vat) =2.204	σ(Vat) =2.710	σ(Vat) =3.062	σ(Vat) =3.332	σ(Vat) =3.548	σ(Vat) =3.732	σ(Vat) =4.154	σ(Vat) = 3.677
	σ(Ara) =2.266	σ(Ara) =3.178	σ(Ara) =3.684	σ(Ara) =4.036	σ(Ara) =4.306	σ(Ara) =4.522	σ(Ara) =4.704	σ(Ara) =5.126	σ(Ara) =4.651
	σ(Cal) =2.597	σ(Cal) =3.507	σ(Cal) =4.016	σ(Cal) =4.368	σ(Cal) =4.635	σ(Cal) =4.854	σ(Cal) =5.036	σ(Cal) =5.457	σ(Cal) =4.983

Appendix II Reference

1. Felmy, A., D. Girvin, AND E. Jenne. MINTEQ – A computer program for calculating aqueous geochemical equilibria. *U.S. Environmental Protection Agency*, Washington, D.C., EPA/600/3-84/032.